



Millar, David C. L. (2023) *Tracking oscillatory signals through the flaring solar atmosphere*. PhD thesis.

<https://theses.gla.ac.uk/83413/>

Copyright and moral rights for this work are retained by the author

A copy can be downloaded for personal non-commercial research or study, without prior permission or charge

This work cannot be reproduced or quoted extensively from without first obtaining permission from the author

The content must not be changed in any way or sold commercially in any format or medium without the formal permission of the author

When referring to this work, full bibliographic details including the author, title, awarding institution and date of the thesis must be given

Enlighten: Theses  
<https://theses.gla.ac.uk/>  
[research-enlighten@glasgow.ac.uk](mailto:research-enlighten@glasgow.ac.uk)

# Tracking Oscillatory Signals Through the Flaring Solar Atmosphere

David C. L. Millar  
MSci (Hons)

Submitted in fulfilment of the requirements for the  
degree of Doctor of Philosophy

Astronomy and Astrophysics Group  
School of Physics and Astronomy  
University of Glasgow



University  
of Glasgow

February 2023

---

This thesis is my own composition except where indicated. No part of this thesis has been submitted elsewhere for any other degree or qualification.

**Copyright © 2022 David C. L. Millar**

7th February 2023

---

*This world, it is a tempest sometimes. But remember, the sun always rises again.*

---

Brandon Sanderson, *The Way of Kings*

# Abstract

Fluctuations in the light we receive from the Sun happen constantly. Much of this variation can be thought of as random, however within solar timeseries there are many true periodic signals to be found, if one knows where to look. Identifying the source of these oscillations can give us a wealth of information about the underlying physical environment of the solar atmosphere. One area which has been particularly exploited is the search for oscillations due to solar flares which can be short-lived, bursty, and variable. Periodic signals detected during solar flares can help us understand the physics of flares, as well as how they interact with the lower layers of the atmosphere. The lower layers of the atmosphere have been known to present periodic fluctuations on timescales of a few minutes in quiet Sun conditions, and there have been some recent reports of energetic events such as flares affecting the quiescent oscillations, even exciting them. This thesis aims to investigate the effect of flares on the lower atmosphere by identifying and categorising oscillatory signals in a variety of solar data.

In Chapter 1 an overview of necessary background physics is given. The layers of the Sun's atmosphere and the standard model of solar flares are described. An introduction to different periodic signals which are present in solar data is given, including quiet Sun periodicities and those observed during transient phenomena.

The methods used throughout the thesis are presented in Chapter 2, starting with descriptions of the instrumentation which obtained the analysed datasets. A discussion is presented on best practices when searching for oscillations in data, and the spectral fitting method is outlined. Techniques used to obtain physical solar parameters from spectropolarimetric observations are also introduced.

In Chapter 3, a study of chromospheric intensity oscillations in a flaring active region is presented. Maps were produced showing the oscillatory signals which were present before and after the occurrence of the flare. When comparing the results after the flare to those before, oscillations were found to have changed their locations and typical periods

### *Abstract*

in the vicinity of a sunspot located near the flare ribbons. These changes were interpreted as the result of a changing magnetic environment connected to the flare.

The interpretations of these results were investigated using magnetohydrodynamic simulations in Chapter 4. Three different sets of simulations were carried out, to identify the most likely effect to have been responsible for the results of Chapter 3. The sets of simulations were concerned with the magnetic field inclination, the chromospheric temperature profile, and the length of the chromospheric cavity. The inclination angle was found to be the most likely of these three effects to change the periodic signals.

Chapter 5 presents analysis of a second dataset, from an active region which featured much less powerful flare activity than the event from Chapter 3. A similar analysis was performed, and extended to also feature Doppler velocity data. Velocity oscillations were identified in pixels which exhibited some of the strongest flare heating. The possible cause of the induced velocity oscillations was explored using measurements of the magnetic field from spectropolarimetric observations, and inversions using the STiC code.

In Chapter 6 concluding remarks are made, including a summary of the main results of the thesis and descriptions of possible future avenues for investigation.

# Contents

<b>Abstract</b>	<b>iii</b>
<b>List of Figures</b>	<b>viii</b>
<b>Acknowledgements</b>	<b>xi</b>
<b>1 Introduction</b>	<b>1</b>
1.1 The solar atmosphere . . . . .	2
1.2 Solar flares . . . . .	4
1.2.1 The standard model of a flare . . . . .	4
1.2.2 Flare classification . . . . .	5
1.3 Solar periodicities . . . . .	6
1.3.1 Sunspot cycles . . . . .	6
1.3.2 Five-minute oscillations . . . . .	6
1.3.3 Three-minute oscillations . . . . .	7
1.3.4 Quasi-periodic pulsations . . . . .	10
1.3.5 Sunquakes . . . . .	10
1.3.6 Loop oscillations . . . . .	11
1.3.7 Chromospheric response to excitation . . . . .	11
<b>2 Methodology</b>	<b>13</b>
2.1 Observational methods . . . . .	13
2.1.1 The Swedish Solar Telescope/CRISP . . . . .	13
2.1.2 Description of CRISP spectral lines . . . . .	15
2.1.3 Solar Dynamics Observatory . . . . .	17
2.2 Spectral analysis . . . . .	19
2.2.1 Power spectra . . . . .	19
2.2.2 Signal detection in coloured noise . . . . .	20
2.2.3 Wavelet analysis . . . . .	24
2.2.4 Detrending methods . . . . .	26

## *Contents*

2.2.5	The spectral fitting method . . . . .	27
2.2.6	Description of the spectral fitting method . . . . .	29
2.2.7	Determination of the preferred model . . . . .	32
2.2.8	Summary of the spectral fitting method . . . . .	33
2.3	Measurements and inversions . . . . .	35
2.3.1	STiC . . . . .	35
2.3.2	The weak-field approximation . . . . .	37
<b>3</b>	<b>The effect of a solar flare on chromospheric oscillations</b>	<b>40</b>
3.1	Event and datasets . . . . .	40
3.1.1	CRISP . . . . .	43
3.1.2	AIA . . . . .	43
3.2	Methods . . . . .	44
3.3	Results . . . . .	44
3.3.1	Preferred models . . . . .	44
3.3.2	Periods and locations of Gaussian bump peaks . . . . .	50
3.3.3	AIA Results . . . . .	52
3.4	Discussion . . . . .	53
3.4.1	Limitations . . . . .	53
3.4.2	Interpretations . . . . .	56
3.5	Conclusions . . . . .	61
<b>4</b>	<b>Simulations of sunspot oscillations</b>	<b>63</b>
4.1	LareXd . . . . .	64
4.2	Code setup . . . . .	65
4.3	Results . . . . .	68
4.3.1	Relationship of simulated parameters to observables . . . . .	69
4.3.2	Vertical magnetic field . . . . .	71
4.3.3	Comparing magnetic field inclinations . . . . .	75
4.3.4	Maltby profile atmospheres with varying inclinations . . . . .	80
4.3.5	Varying the height of the transition region . . . . .	85
4.4	Discussion . . . . .	86
4.5	Conclusion . . . . .	90
<b>5</b>	<b>Oscillations in a small flaring active region</b>	<b>92</b>
5.1	Description of flare events and dataset . . . . .	92
5.1.1	Reference points . . . . .	96

## *Contents*

5.2	Analyses . . . . .	97
5.2.1	Velocity measurement . . . . .	98
5.3	Intensity oscillations . . . . .	101
5.3.1	Reduced resolution results . . . . .	101
5.3.2	Intensity oscillations at full resolution . . . . .	109
5.4	Velocity oscillations . . . . .	109
5.4.1	The flare ribbon . . . . .	115
5.4.2	Intensity vs velocity oscillations . . . . .	115
5.5	Evolution of the atmosphere around the oscillatory signals . . . . .	116
5.5.1	Intensity imaging . . . . .	116
5.5.2	Magnetic field . . . . .	118
5.6	STiC inversions . . . . .	121
5.6.1	Inversion setups . . . . .	121
5.6.2	STiC results . . . . .	122
5.7	Discussion . . . . .	128
5.7.1	Sunspot oscillations . . . . .	128
5.7.2	Flare ribbon oscillations . . . . .	131
5.7.3	Comparison to the 2014-09-06 event . . . . .	133
5.8	Conclusion . . . . .	134
<b>6</b>	<b>Conclusions</b>	<b>136</b>
	<b>Bibliography</b>	<b>142</b>

# List of Figures

2.1	Diagram of a Fabry-Pérot Interferometer. . . . .	14
2.2	Synthetic timeseries with white noise backgrounds and their corresponding power spectra. . . . .	21
2.3	Synthetic timeseries with red noise backgrounds and their corresponding power spectra. . . . .	23
2.4	A Morlet wavelet. . . . .	25
2.5	Example of a timeseries which is best fit by the red noise background model.	29
2.6	Example of a timeseries which is best fit by the Gaussian bump model. . .	31
2.7	Example of a timeseries which is best fit by the kappa function model. . .	32
2.8	Flow chart summarising the spectral fitting method. . . . .	34
3.1	Lightcurves of GOES 1–8 Å and the CRISP spectral lines integrated across the field of view. . . . .	41
3.2	Context images of AR 12157 in several wavelengths. . . . .	42
3.3	Examples of each of the three model fits in observed timeseries. . . . .	45
3.4	Preferred spectrum models for Ca II 8542 Å in the pre-impulsive interval.	46
3.5	Preferred spectrum models for Ca II 8542 Å in the post-impulsive interval.	46
3.6	Preferred spectrum models for H $\alpha$ in the pre-impulsive interval. . . . .	47
3.7	Preferred spectrum models for H $\alpha$ in the post-impulsive interval. . . . .	47
3.8	Gaussian bump peaks for Ca II 8542 Å in the pre-impulsive interval. . . .	51
3.9	Gaussian bump peaks for Ca II 8542 Å in the post-impulsive interval. . . .	51
3.10	Gaussian bump peaks for H $\alpha$ in the pre-impulsive interval. . . . .	51
3.11	Gaussian bump peaks for H $\alpha$ in the post-impulsive interval. . . . .	52
3.12	Pre- and post-impulsive oscillatory signals detected in the AIA 1600 Å and 1700 Å channels. . . . .	54
3.13	HMI continuum image and magnetic field component timeseries from locations across the sunspot. . . . .	59
3.14	AIA 171Å images, with the locations of oscillatory signals over-plotted. . .	61
4.1	Cell spacing as a function of height in the $y$ -direction . . . . .	66

## List of Figures

4.2	Comparison of FAL-C, Maltby and STiC-inverted umbral temperature profiles.	67
4.3	Temperature and density stratification across the umbral atmosphere. . . . .	68
4.4	Several physical parameters sampled from the upper chromosphere of the vertical magnetic field simulation. . . . .	70
4.5	Vertical velocity variation in space and time in the umbral atmosphere simulation. . . . .	72
4.6	Height variation of $v_y$ Fourier power spectra in the umbral simulation with vertical magnetic field. . . . .	73
4.7	$v_y$ timeseries at various heights in the atmosphere. . . . .	74
4.8	$v_y$ timeseries at a fixed height in Set 1 simulations, with varying magnetic field inclinations. . . . .	75
4.9	$v_y$ in simulations from Set 1. . . . .	78
4.10	Power spectrum as a function of height, in simulations from Set 1. . . . .	79
4.11	Power spectrum as a function of height, for Set 2 simulations. . . . .	81
4.12	Cut-off period as a function of height in the umbral and Maltby atmospheres.	82
4.13	$v_y$ as a function of height and time in simulations from Set 3. . . . .	83
4.14	Power spectrum as a function of height, in simulations from Set 3. . . . .	84
4.15	Various measurements of velocity, comparing results from simulations with varying inclinations. . . . .	88
5.1	GOES timeline of 2013-06-13 flare events. . . . .	93
5.2	Context images of NOAA 11768 in Ca II 8542 Å. . . . .	94
5.3	Context images of NOAA 11768 in AIA 94 Å and 171 Å channels. . . . .	94
5.4	Stokes parameter maps for Fe I 5250 Å. . . . .	95
5.5	Stokes parameter maps for Ca II 8542 Å. . . . .	96
5.6	Reference images showing the named sunspots and locations of STiC inversions. . . . .	97
5.7	Examples of each of the three model fits in observed timeseries from the 2013 dataset. . . . .	99
5.8	Preferred models in the pre-flares interval for reduced-resolution Ca II 8542 Å intensity. . . . .	101
5.9	Preferred models in the post-flare interval for reduced-resolution Ca II 8542 Å intensity. . . . .	102
5.10	Preferred models in the pre-flares interval for reduced-resolution Fe I 5250 Å intensity. . . . .	103
5.11	Preferred models in the post-flares interval for reduced-resolution Fe I 5250 Å intensity. . . . .	104

## List of Figures

5.12 Gaussian bump peak periods in the pre-flares interval for reduced-resolution Ca II 8542 Å.	105
5.13 Gaussian bump peak periods in the post-flares interval for reduced-resolution Ca II 8542 Å.	106
5.14 Gaussian bump peak periods in the pre-flares interval for reduced-resolution Fe I 5250 Å.	107
5.15 Gaussian bump peak periods in the post-flares interval for reduced-resolution Fe I 5250 Å.	108
5.16 Preferred spectrum models in the pre-flares interval for full-resolution Ca II 8542 Å.	110
5.17 Preferred spectrum models in the post-flares interval for full-resolution Ca II 8542 Å.	111
5.18 Gaussian bump peak periods in the pre-flares interval for full-resolution Ca II 8542 Å.	112
5.19 Gaussian bump peak periods in the post-flares interval for full-resolution Ca II 8542 Å.	113
5.20 Preferred models and Gaussian bump peaks for velocity data from Ca II 8542 Å.	114
5.21 Intensity images of the sunspots in Fe I 5250 Å wing and Ca II 8542 Å line core.	117
5.22 Magnetic field components over the sunspots.	119
5.23 Velocity profiles used in the initialisation of STiC timeseries inversions.	123
5.24 Atmospheric parameter maps from STiC inversions, at chromospheric depth.	125
5.25 Atmospheric parameters slice at a constant $y$ -value.	126
5.26 Timeseries of temperature and $v_{los}$ for STiC inverted pixels, with $v_{los}$ wavelet spectra.	127

# Acknowledgements

Over the past four years I have had many great experiences and met some amazing people. This is a quick note to say thank you to everyone who has helped me along the way.

First and foremost, I must thank Lyndsay Fletcher, my supervisor. Your infectious enthusiasm for solar physics seeped into me five years ago, and your influence has shaped me into the scientist I am today. Thank you for giving me direction while also letting me feel my own way, and thanks for giving me confidence and reassurance in times of self-doubt.

I must also mention the many other researchers who have helped me along the way. To Ryan Milligan and Nic Labrosse, who were secondary supervisors to the project; Jayant Joshi, for enthusiastic help with a complicated dataset; Jaime de la Cruz Rodríguez, for taking the time to get me up to speed with STiC. To everyone else I have ever bothered with a question about science, a code, or an admin issue: it is greatly appreciated.

I would like to thank the Carnegie Trust for supporting this project, particularly for their response during difficult times.

To my fellow PhD students in Room 604, past and present, it has been great to be a part of this community. The many distracting chats, whiteboard sessions, phys-art projects, and tech support sessions made days go quicker. Chris, John, Aaron, and Kris: I'm glad to have been along for the ride with you all. Everyone else in the astro department who attended afternoon coffee sessions, I wish we could have had more!

Thank you to everyone in the *Roasties* family, those that have been with me since before I can remember, and those that I've picked up along the way: your friendship is truly treasured.

To all of my furry and feathery friends who have helped me through this PhD — Dexter, Daisy, Rosie, Benny, Freddie, Cosmo, and Sonny — you have kept me sane and been a constant source of joy. Sonny, your suggestions and corrections have really improved this thesis. Thanks to Fiona and Ian for helping us wrangle our animals, and for always checking in.

### *Acknowledgements*

I would not be a functioning human without the guidance of my Mum and Dad. Thanks for being my best role models, and for always supporting my path. Gran, thanks for all your help and for always bigging me up! To Rachel, you are an amazing sister and a source of inspiration.

Gilly, words cannot describe the impact you've had on my life. Weathering hard times with you has made me certain that you're my soul mate and I'll spend the rest of my life with you. Thank you for always keeping my head up and being my biggest cheerleader, and best friend.

---

# 1

---

## Introduction

You would not know it from gazing at the Sun as it moves across the sky, but our star is an ever-changing body, almost any way you look at it. Like an energetic puppy, getting it to sit still for a photo is impossible, and we are (currently) unable to reproduce it in a laboratory setting. Because of this our insights into many of its workings are fleeting, despite the fact that there are many telescopes constantly pointing in its direction. The Sun is a main sequence star, approximately 4.6 billion years old ([Bonanno et al. 2002](#)), and has at least eight planetary companions in its solar system, a configuration which we will no doubt find increasingly more common as the search for extrasolar planets continues. The Sun is the only star with a planet which we know sustains organic life — Earth. The Sun is our best example of a star, and by studying it we can gain an understanding of the millions of others that we see in the night sky.

In several billion years the Sun will exhaust its store of nuclear fuel and expand into a red giant, growing so large that it will envelop the inner planets in its radius. In the meantime, life on Earth exists due to a delicate balance of the Sun's energetic output: the optical flux we receive is enough to heat our planet to a liveable temperature, and for it to sustain an atmosphere which provides breathable air. The atmosphere also protects us from some of the more harmful solar radiation, namely high energy ultraviolet rays which can cause sunburns in small doses, and alter DNA in large doses. The balance in the Sun-Earth system can be altered by extreme solar events which are collectively known as “space weather”. Forecasting space weather has become an important aspect of monitoring our environment, as some of the dangers associated with it include telecommunications interruptions, power grid failures, and damage to manned and unmanned space missions.

Some researchers believe the Sun is capable of much more energetic events than we have ever witnessed, due to observations of “superflares” in solar-type stars with the Kepler

## 1.1 *The solar atmosphere*

telescope (Cliver et al. 2022). During superflares the brightness of distant stars can increase by up to  $\sim 20\%$  of the stellar luminosity, while one of the largest solar flares observed in the last 20 years saw a 0.03% increase in the Sun's brightness (Kopp 2016). Should the Sun undergo such an event the consequences for Earth would be unprecedented.

In order for humanity to progress through the technological age and beyond, it is therefore necessary for us to understand our star and space weather. As of now it is a fairly young science, though thankfully we have a plethora of instrumentation and researchers dedicated to unravelling the mysteries of the Sun.

There is still a lot we do not know about flares and the solar atmosphere. In this thesis we present work which is primarily focussed on observing the lower layers of the solar atmosphere, and how they can be affected during flare activity. We search for periodicities in a variety of solar data, as their presence can be an indicator of physical processes at work. In this chapter we will introduce the solar atmosphere and solar flares. We will go on to give examples of some relevant periodicities that we can observe in solar data, in quiet Sun conditions and those which are associated with energetic events such as flares.

### 1.1 The solar atmosphere

The atmosphere of the Sun begins at the surface, approximately 7 million kilometres from its core, and is comprised of three main layers: photosphere, chromosphere, and corona. Beyond the corona there is the solar wind, a constant outflow of material into the Solar System. A combination of observations and theoretical models have shaped our understanding of the temperature structure and elemental abundance of the atmosphere. The resulting temperature and density stratifications are described by semi-empirical model atmospheres such as FAL-C (Fontenla et al. 1993).

The solar surface is defined as the point where light escapes its interior, marking the beginning of the photosphere. Formally this is where the optical thickness  $\tau$  for light at 5000 Å is unity (also styled as  $\log \tau_{5000} = 0$ ). The photosphere is dominated by continuum radiation of an approximate black body at a temperature of 5800 K. From photospheric radiation we observe features including granulation and sunspots. Granulation is caused by bubbles of plasma at slightly different temperatures rising and falling in the convective zone below the surface, with typical horizontal sizes  $\sim 1$  Mm (Nordlund et al. 2009).

## 1.1 *The solar atmosphere*

Bundles of magnetic flux can rise up from the convection zone and break through the lower photosphere, and can develop into  $> \text{kG}$  magnetic fields normal to the surface. Convection is suppressed in these areas, causing cool and comparatively dark areas on the photosphere called sunspots ([van Driel-Gesztelyi & Green 2015](#)). Groups of sunspots are an indicator of active regions, which are the source of many energetic space weather events. Sunspots are used as an indicator of solar activity, with a greater number of sunspots indicating a more active Sun. Sunspots are comprised of a dark umbra, with temperatures of  $\sim 4000 \text{ K}$ , surrounded by the penumbra, an intermediary between the sunspot and the surrounding quiet Sun, which is slightly hotter than the umbra, has a highly inclined magnetic field ([Mathew et al. 2003](#)), and has the appearance of long strands extending from the umbra.

As height above the surface increases, the temperature drops from  $\sim 5800 \text{ K}$  to  $\sim 4400 \text{ K}$  at a height of 500 km. This is called the temperature minimum region and is considered the top of the photosphere.

Above the temperature minimum region is the chromosphere: one of the most complex parts of the atmosphere. It is so called because of its red colouring when it was first seen by astronomers, which comes from the predominant  $\text{H}\alpha$  spectral line. The chromosphere is a thin layer ( $\sim 1000 \text{ km}$ ) but is extremely varied in appearance. Here we observe many complex magnetic structures such as spicules, tall spikes of plasma that extend high into the atmosphere and give the chromosphere a “hairy” appearance. The density in the chromosphere drops with height but the temperature increases to  $\sim 10^4 \text{ K}$  at its upper boundary. The reason for temperature increasing into the upper layers of the Sun’s atmosphere is not yet known, but is possibly due to the dissipation of magnetic or acoustic wave energy generated by photospheric convection ([Srivastava et al. 2021](#)). The chromosphere is optically thin to most radiation, and we therefore mostly study it using spectral line emission or absorption features.

Above the chromosphere is a thin layer known as the transition region where the temperature increases extremely rapidly to  $\sim 1\text{MK}$  over a few hundred kilometres, into the upmost layer of the Sun’s atmosphere, the corona. This upper part of the atmosphere is observable by eye during solar eclipses, but is usually only visible using ultraviolet (UV) and extreme ultraviolet (EUV) telescopes situated in space. This prevalence in UV wavelengths is due to its high temperature and low density, resulting in highly ionised material such as iron atoms. The plasma of the corona is in the “frozen in” condition ([Alfvén 1942](#)), meaning that the plasma flows along magnetic field lines. We make use of this fact to visualise the coronal magnetic field by imaging the radiation emitted by

## 1.2 Solar flares

the coronal material. The field structures are known as coronal loops, and they trace out fields which can originate deep in the photosphere below.

The corona extends out to several solar radii from the surface and can reach temperatures  $\geq 2\text{MK}$ . Similar to the chromosphere, the reason for this high temperature despite the drop in density is an ongoing puzzle for solar physicists. It is possible that waves transfer a significant amount of energy from the lower atmosphere, or that reconfiguring magnetic fields release energy to heat the atmosphere (De Moortel & Browning 2015).

## 1.2 Solar flares

On the night of 1<sup>st</sup> September 1859 a huge magnetic storm occurred at Earth, and bright red aurorae were observed over the world, at latitudes as low as 23 degrees (Kimball 1960). Around 18 hours earlier, Richard Carrington was observing a group of sunspots when two extremely bright patches appeared, and then faded within minutes (Carrington 1859). The unusual observation (called the “Carrington Event”) was corroborated by Richard Hodgson (1859). This was the first solar flare ever observed, and none have rivalled its power since (Tsurutani 2003). Flares are the most powerful processes in the Solar System, releasing huge amounts of energy ( $\sim 10^{25}\text{ J}$ ) in a relatively short amount of time ( $\sim 10\text{ min}$ ) (Fletcher et al. 2011), and are often accompanied by coronal mass ejections (CMEs), which throw plasma out into interplanetary space (Webb & Howard 2012). CMEs are often directed towards the Earth, and cause geomagnetic storms when the magnetised clouds interact with the Earth’s magnetosphere. The CME associated with the Carrington Event is what caused the enhanced aurorae, and there were also reports of fires caused by sparking telegraph wires (Shea & Smart 2006). Carrington noted the geomagnetic storm in the report of his observations, but it was not until the next century that the link between such storms and solar flares was fully established (Hale 1931, Chapman & Bartels 1940, Newton 1943).

### 1.2.1 The standard model of a flare

Flares usually occur in active regions above sunspots or sunspot groups, and are defined as short intense flashes of radiation. Some competing explanations exist for the cause of flares, but this description is based on the most popular of these called the standard model. The standard model is also known as the CSHKP model after the authors who

## 1.2 Solar flares

developed it (Carmichael 1964, Sturrock 1966, Hirayama 1974, Kopp & Pneuman 1976). Magnetic field loops which are anchored in the lower atmosphere lie in the corona and can become sheared and twisted, a process driven by convective motion under the photosphere. The potential energy stored in the fields increases as they twist. The flare begins when this large amount of energy is released by a magnetic reconnection event. Reconnection happens when field lines change their topology and connectivity, changing to a lower energy state, and this release of energy starts the “impulsive” phase of the flare. We therefore observe changes to the measured magnetic field in the majority of flares (Castellanos Durán et al. 2018). Brightening at soft X-ray (SXR) wavebands is observed at the top of the flare loop where heating and acceleration of electrons occurs. The accelerated particles travel down the magnetic field of the loop, and impart a large amount of energy in the chromosphere, which heats and ionises the material there. The footpoints of the flare loop in the chromosphere become bright in hard X-ray (HXR) radiation, evidence of bremsstrahlung radiation from non-thermal electrons colliding with the chromosphere. This is known as the collisional thick target model (Brown 1971). Chromospheric brightenings called flare ribbons extend from the footpoints, observed in optical, near-infrared and UV wavelengths. Heating causes the material to expand, and can undergo “evaporation”, where chromospheric matter flows up and fills coronal loops (Neupert 1968, Graham & Cauzzi 2015). A corresponding downflow of chromospheric material is known as chromospheric condensation (Ichimoto & Kurokawa 1984, Wuelser & Marti 1989). After the non-thermal HXR radiation stops, the slow decay of excess flare radiation due to cooling is known as the “gradual” phase of the flare, and can last several hours (Fletcher et al. 2011).

### 1.2.2 Flare classification

Historically, H $\alpha$  emission was used to compare the sizes of flare events. In the modern day, flares are categorised based on the amount of X-ray flux they emit. The Geostationary Operational Environmental Satellite program (GOES: Garcia 1994) measures the SXR flux from the whole Sun continuously in two bands: 0.5–4.0 Å and 1.0–8.0 Å. Flares are classified based on the peak flux in the 1.0–8.0 Å band, and are labelled as A, B, C, M and X corresponding to GOES peaks of  $10^{-8}$ – $10^{-4}$  W m $^{-2}$ . Each letter class contains a scale of 1–9 except X, which extends past X10. The Carrington Event is estimated to have been X45 ± 5 (Cliver & Dietrich 2013).

## 1.3 Solar periodicities

Much of the variation we see in our observations of the Sun is essentially random in nature, and can be interpreted as a type of noise. However, there are many sources of true periodic signals which can be identified in all parts of the Sun-Earth system, from within the solar interior to the solar wind at Earth's orbit (Potapov et al. 2013, Guglielmi & Potapov 2021). Periodic motion and oscillations are often signatures of waves, which are important physical processes for the transport of energy, for example in chromospheric and coronal heating. We will briefly introduce some examples of periodicities that are always present in the Sun, and also transient phenomena which have been observed to produce oscillatory signals. Both types of periodic signal (quiescent and transient) are important for the research presented in this thesis, as we investigate the ways flares can excite new oscillations or affect the periodicities which were already present in the lower atmosphere.

### 1.3.1 Sunspot cycles

Perhaps the longest-period cyclical variation of the Sun is found when plotting the number of sunspots visible on the solar disk over time. The practice of counting sunspots dates back to the middle of the last millennium (Clette et al. 2014) and reveals a robust 11 year oscillatory pattern. This is also known as the solar cycle, and is one way of predicting the average amount of solar activity (e.g. flares, CMEs) in the coming years.

### 1.3.2 Five-minute oscillations

In 1962 it was discovered that the Sun's surface showed ubiquitous oscillations in velocity on timescales of  $\sim 5$  minutes (Leighton et al. 1962). These are well-observed to this day and their frequencies are found to exhibit a spectrum with many localised fringes of oscillatory power, which peaks at around 3.3 mHz (Christensen-Dalsgaard 2002). The oscillations have been named *p*-modes (pressure-modes) and their study is part of the field now known as helioseismology, which is concerned with global oscillations of the solar interior. The explanation is that these modes are caused by acoustic waves travelling through the solar interior, which form standing waves after being reflected in the cavity between the surface and the deeper layers of the interior. The cause of the cavity and a key factor in the propagation of acoustic waves is the adiabatic sound speed  $c_S$ , given by

### 1.3 Solar periodicities

$$c_s^2 = \frac{\gamma p}{\rho} = \frac{\gamma R T}{\mu}. \quad (1.1)$$

Here  $\gamma$  is the adiabatic exponent ( $= 5/3$ ),  $p$  the pressure,  $\rho$  the density,  $R$  the ideal gas constant,  $T$  the temperature and  $\mu$  the mean molecular weight.

The temperature (and hence  $c_s$ ) increases towards the solar core, causing strong refraction of downward propagating waves, while upward travelling waves are reflected at the surface by the sharply changing stratification (layering), forming the cavity (Thompson 2004).

#### 1.3.3 Three-minute oscillations

While the 5-minute oscillations are characteristic of the photosphere, the chromosphere exhibits signals at approximately 3-minute periods. These were observed in the early 1970s in intensity and velocity data from supergranulation networks and sunspot umbrae (Bhatnagar & Tanaka 1972, Phllis 1975). The oscillations are most strongly seen over sunspots (Khomenko & Collados 2015). Initially it was thought by some that these are caused by waves trapped in a “chromospheric cavity”, analogous to their 5-minute counterparts (Uchida & Sakurai 1975). However, signatures of 3-minute signals have been observed in the lower corona (high above the chromosphere; Reznikova et al. 2012), indicating that there is not an upper boundary to trap the waves, or that the cavity is a “leaky resonator”. A prevalent explanation for the 3-minute periodicity is the acoustic cut-off frequency of the chromosphere.

#### Cut-off frequency

The acoustic cut-off frequency is an intrinsic property of plasma in a stratified medium. It places a lower bound on the frequency of waves that can propagate through a medium, and is caused by the dispersive nature of the chromospheric plasma. Alternatively we can refer to an upper bound on the period of waves — the cut-off period  $P_c$ . A dispersion relation describes how the group and phase velocities of waves in the plasma depend on their wavenumber  $k$  and angular frequency  $\omega$ :

$$\omega^2 = \omega_c^2 + k^2 c_s^2. \quad (1.2)$$

### 1.3 Solar periodicities

The cut-off frequency is  $\omega_c$  in the above equation. The group velocity (the rate at which a disturbance moves) is  $v_g = d\omega/dk = kc_s^2/\omega$ . For propagating waves  $k^2 > 0$ , i.e.  $\omega > \omega_c$ . If the angular frequency is below the cut-off value ( $\omega < \omega_c$ ),  $k^2$  is negative and the waves are evanescent, meaning they decay exponentially and do not propagate. The value of the cut-off frequency is given by:

$$\omega_c = \frac{\gamma g}{2c_s} = \sqrt{\frac{\gamma \mu g^2}{4RT}} \quad (1.3)$$

where  $g$  is the gravitational acceleration. Using values corresponding to the temperature minimum region of  $g = 273.6 \text{ m s}^{-2}$  and  $T = 4400 \text{ K}$  the resulting cut-off frequency is  $\omega_c = 0.03 \text{ rad s}^{-1}$ . This frequency corresponds to periods of  $P_c \approx 200 \text{ s}$  and agrees well with the observed oscillatory signals in chromospheric data (e.g. Deubner & Gough 1984, Duvall et al. 1991).

In the magnetised solar atmosphere it is necessary to think beyond the acoustic modes. In regions of high magnetic field, such as sunspot umbrae, photospheric disturbances can convert into magnetoacoustic waves in regions where the Alfvén speed and sound speed are similar, and the resulting waves travel along magnetic field lines. Due to the Sun's gravitational field, the waves become magnetoacoustic gravity waves (MAG waves: Bel & Leroy 1977) and the cut-off frequency becomes dependent on the angle between the magnetic and gravitational fields  $i$ , introducing a  $\cos i$  term to equation 1.3. This leads to running penumbral waves (RPWs: Jess et al. 2013), an observed behaviour where the period of oscillatory signals increases as one moves radially out from the centre of a sunspot, as the magnetic field inclination increases (Reznikova et al. 2012, Sych et al. 2020).

Theoretical models to explain the resultant chromospheric signals incorporate some driving process to excite the chromospheric plasma, which naturally resonates at its cut-off frequency. The source of this driving process has been modelled as a sinusoidal “piston” at the base of the chromosphere, meant to simulate the photospheric 5-minute oscillations (Fleck & Schmitz 1991), and velocity “kicks”, temporally localised injections of energy (Kalkofen et al. 1994, Chae & Goode 2015). This injection of energy could come from the underlying oscillations or from energy deposition during, for example, solar flares.

### 1.3 Solar periodicities

#### Chromospheric cavity

The chromospheric cavity is thought to exist between the temperature minimum region (altitude  $\sim 500$  km) and the transition region ( $\sim 2500$  km). The period of the resonance,  $P_r$  is approximately given by

$$P_r \approx \frac{2L}{\bar{v}_c n}, \quad (1.4)$$

where  $L$  is the length of the cavity,  $\bar{v}_c$  is the average speed of the waves and  $n$  is the harmonic number (Freij et al. 2016). With  $L = 2000$  km and  $\bar{v}_c = 10$  km s $^{-1}$ , the harmonics occur at 400 seconds, 200 seconds, e.t.c.

In an inclined field, the waves travel farther along their paths before being reflected by the cavity bounds, due to being guided by the field. A magnetic field of inclination  $i$  increases the periods of resonance by a factor  $1/\cos i$ , resulting in the same increase in period as that included in the MAG wave cut-off frequency.

#### Conflicting and cooperating theories

Modelling studies have attempted to determine if the 3-minute sunspot oscillations arise from cut-off effects or the chromospheric cavity. Fleck & Schmitz (1991) determined that the long-period photospheric driver was enough to excite the cut-off frequency indefinitely with no need for the cavity. Chae & Goode (2015) claimed that high frequency waves travel at higher group velocities and thus escape the chromosphere quickly, leaving behind oscillations near the cut-off frequency. In investigations using simulations, some authors conclude that both the cavity and cut-off frequency are responsible, such as Botha et al. (2011) who found results consistent with a leaky resonator, and thought that different temperature profiles could cause varying resonances. Similarly Felipe (2019) found that 3-minute resonances were impossible in a chromosphere without an upper reflective boundary. We investigate these effects in Chapter 4 by simulating chromospheric waves in a 2D atmosphere and varying several parameters which can affect the observed periodicities.

### 1.3.4 Quasi-periodic pulsations

The term quasi-periodic pulsation (QPP) is something of a catch all, being used to refer to oscillations observed around the time of solar flares across a wide range of timescales and in different types of data. The periods of QPPs range from sub-second (Tan & Tan 2012) up to several minutes (Li et al. 2015), and they are observed across the electromagnetic spectrum, from radio/microwave (Inglis et al. 2016) to X-rays and  $\gamma$ -rays (Nakariakov et al. 2010a). QPPs are often observed in sun-as-a-star observations with no spatial resolution (Van Doorsselaere et al. 2016), in wavelengths which are produced mainly by flare-temperature plasma (e.g. X-ray). There is evidence that the majority of solar flares exhibit QPPs, as Simões et al. (2015) found when studying SXR lightcurves from GOES. In a recent large scale statistical study Hayes et al. (2020) found a tendency for SXR QPPs in larger flares (class X). However, QPPs have been detected in smaller flares (Kumar et al. 2017, Nakariakov et al. 2018). Oscillatory signals can appear during the pre-flare, impulse or decay phases. QPPs are also known to evolve, with both amplitudes and periods changing over time (Reznikova & Shibasaki 2011). Most signals are short-lived, which is expected due to the transient nature of flares, but some persist long into the gradual decay phase (Hayes et al. 2019).

The wide variety in the types of QPP signals suggests a variety of physical explanations (McLaughlin et al. 2018). Signals in hard X-ray wavelengths, characteristic of bremsstrahlung radiation, could suggest pulse-like injections of accelerated particles on sub-minute timescales, while varying radio/microwave radiation from electron-gyrotron radiation could be caused by changing magnetic fields, and SXR/extreme UV emission could be from changing thermal properties of the plasma. Pulsating signatures could be from a bursty kind of reconnection, “magnetic dripping”, from the corona (Nakariakov et al. 2010b).

### 1.3.5 Sunquakes

Large flares are sometimes accompanied by photospheric disturbances which can develop as helioseismic waves, called sunquakes (Kosovichev 2015). Sunquakes are detected as expanding waves which are detected in running-difference dopplergrams (velocity maps) in photospheric data (e.g. Kosovichev & Zharkova 1998, Donea et al. 2006). It is thought that the large amount of energy and momentum which is transferred to the lower atmosphere during a flare can create an acoustic shock front which travels into the solar interior. These waves are then reflected by the increased density and temperature of the deeper layers of the convective zone, creating the sunquake when they return to the photosphere.

### 1.3 Solar periodicities

Alternative theories for the cause of sunquakes exist, such as a Lorentz force brought upon by magnetic field changes (Hudson et al. 2008, Fisher et al. 2012). A particularly powerful sunquake associated with the X9.3 flare of 6<sup>th</sup> September 2017 (Sharykin & Kosovichev 2018) was reported to have a detectable response in the chromosphere (Quinn et al. 2019). In recent statistical analyses, sunquakes were observed in  $\sim$ 20% of flares of class M or above (Sharykin & Kosovichev 2020) in photospheric data, and  $\sim$ 15% of those events showed clear seismic signatures in ultraviolet intensity data from higher in the atmosphere (Quinn et al. 2021). Despite the possibility of photospheric and chromospheric oscillations due to sunquakes, they are unlikely to factor into the results of the studies presented in this thesis, due to their extreme transience.

#### 1.3.6 Loop oscillations

The large coronal loops which lie above active regions can be seen to sway back and forth as the result of a flare or other eruptive process in the corona. First observed in the late 1990s (Aschwanden et al. 1999, Nakariakov et al. 1999), this phenomenon is important for the field of coronal seismology. Typically they oscillate with periods of a few to several minutes (Nakariakov et al. 2021) but have been observed up to hours long (Verwichte et al. 2010). They are often observed using EUV imaging (e.g. Aschwanden & Schrijver 2011, Allian et al. 2019) with several hundred being observed in the last solar cycle (Nechaeva et al. 2019). It is thought that loop oscillations can excite periodic signals at the footpoints of the loops, and vice versa, by waves travelling along the flux tubes.

#### 1.3.7 Chromospheric response to excitation

As discussed in Section 1.3.3, it is thought that the chromosphere can be excited by an energy injection, after which it will oscillate at the cut-off period (approximately 3 minutes). Milligan et al. (2017) found evidence of  $\sim$ 3-minute oscillations in sun-as-a-star Ly- $\alpha$  and UV emission during the impulsive phase of an X-class flare. The lack of periodic signals in HXR data suggested a chromospheric origin of the oscillation, and was interpreted as a dynamic response of the chromosphere to the energy deposited by the flare. Full-disk Ly- $\alpha$  QPPs have also been observed by Li et al. (2020), at 3-minutes but also at 1-minute periods during the impulsive phase, which was suggested to be indicative of magnetic dripping.

### 1.3 Solar periodicities

Kwak et al. (2016) reported velocity oscillations in the chromosphere of around 3 minutes after a downflow event was seen in chromospheric and transition region lines. This is another candidate for the source of a velocity kick. Recently, Farris & McAteer (2020) mapped the 3-minute power in UV channels and found localised areas of increased signal during an X2 flare, cospatial to HXR flare emission, which again suggests a chromospheric response to energy injection. Monsue et al. (2016) studied oscillations in H $\alpha$  intensity of flaring regions and reported enhancements at low frequencies (1 mHz) prior to and after the flares, while higher frequencies were suppressed. Excitation of oscillations over sunspots in flaring regions have been observed in the past (Kosovichev & Sekii 2007, Sych et al. 2009) with Sych et al. (2009) observing an increase in the power of 3-minute oscillations in the lead up to the flare. As of now the link between flare activity and sunspot oscillations is unclear.

The studies cited above utilise a variety of different techniques for identifying oscillatory behaviour. We will discuss many of these in Chapter 2, as well as describing the methods which we have used in our own observational work.

---

# 2

---

## Methodology

This chapter will contain descriptions of some of the techniques which were used to gather and analyse data throughout this thesis. We will present information about the sources of observational data including instruments of the Swedish Solar Telescope and NASA's Solar Dynamics Observatory. A discussion of different approaches to identifying oscillatory signals in data is then presented, before a short introduction to some methods which were used to carry out the studies presented in Chapters 3 and 5.

### 2.1 Observational methods

In order to understand as much of the Sun's atmosphere as we can, we must use data from a variety of sources. Ground-based instruments provide high-resolution imaging, spectroscopy, and polarimetry at optical and near-infrared wavelengths, while space-based observatories can observe the Sun almost constantly, and allow us to image in UV wavebands which are blocked by the Earth's atmosphere.

#### 2.1.1 The Swedish Solar Telescope/CRISP

The Swedish Solar Telescope (SST: [Scharmer et al. 2003a](#)) is situated on La Palma in the Canary Islands, and operated by the Institute for Solar Physics of Stockholm University. It consists of a 1-metre refracting telescope atop a 15 m tower, 2400 m above sea level. Light is focused down the tower which is kept as a near-vacuum, and directed to various instrumentation. In this thesis we present data from one of these instruments, the CRisp Imaging Spectro-Polarimeter (CRISP: [Scharmer et al. 2008](#)). All ground-based telescopes suffer from “seeing” effects of the Earth’s atmosphere — blurring caused by wavefronts

## 2.1 Observational methods

passing through turbulent air. The elevation of the SST reduces these effects as much as possible, as well as sophisticated adaptive optics systems (Scharmer et al. 2003b) and post-processing of the images (de la Cruz Rodríguez et al. 2015). The most common form of image post-processing for CRISP is the Multi-Object Multi-Frame Blind Deconvolution (MOMFBD) method (Van Noort et al. 2005). Images taken by the detector are a convolution of the true image and the point spread function of the instrument plus seeing noise, so in theory the true image can be found by deconvolution. The MOMFBD method utilises multiple detectors (objects) taking sets of images (multiple frames) at identical times, before deconvolving to obtain the best images.

The CRISP instrument is a dual Fabry-Pérot interferometer which can sample light from 5100–8600 Å, focusing it onto two CCD cameras. The instrument is able to measure polarisation of light using liquid crystal modulation and a polarising beam splitter (van Noort & Rouppe van der Voort 2008).

A Fabry-Pérot Interferometer (also called an etalon) consists of two partially reflective surfaces which must be extremely smooth and flat, held apart at distance  $d$ . A simplified configuration of an etalon is shown in Figure 2.1. In the following description we assume the refractive index of the exterior medium is unity.

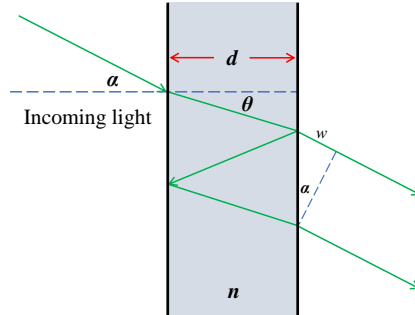


**Figure 2.1:** Fabry-Pérot Interferometer ray paths. The rays emerging on the right of the picture are parallel and undergo constructive interference.

Incoming light at incident angle  $\alpha$  is reflected between the two mirrors and transmitted through to detectors. The medium between the plates has a refractive index  $n$ , and the internal angle is  $\theta$ . The optical path length difference between the two outgoing rays  $\Delta p$  is given by the difference between the internal reflections and the length  $w$  depicted in Figure 2.1:

$$\Delta p = n \left( \frac{2d}{\cos \theta} \right) - w = \frac{2nd}{\cos \theta} - 2d \tan \theta \sin \alpha. \quad (2.5)$$

## 2.1 Observational methods

Using the fact that  $\sin \alpha = n \sin \theta$ :

$$\Delta p = 2nd \left( \frac{1}{\cos \theta} - \tan \theta \sin \theta \right) = 2nd \left( \frac{1 - \sin^2 \theta}{\cos \theta} \right) \quad (2.6)$$

and we arrive at

$$\Delta p = 2nd \cos \theta. \quad (2.7)$$

The optical path length results in constructive interference when  $\Delta p = m\lambda$  where  $m$  is an integer and  $\lambda$  is the target wavelength. These devices can then be used to select which wavelengths of light emerge by altering the space between the mirrors or the refractive index of the internal medium, such as by adjusting air pressure (Ball 2006). By finely tuning the interferometer CRISP can scan along spectral lines with sub-Angstrom accuracy. This means that the individual wavelength points of a scan are not recorded at exactly the same time.

### 2.1.2 Description of CRISP spectral lines

CRISP has the capability to study many spectral lines but two of the most common for observations of the chromosphere are H $\alpha$  and Ca II 8542 Å from the calcium IR triplet. To study the photosphere, iron lines are often used, such as Fe I 5250 Å, which we utilise in Chapter 5.

The chromosphere is optically thin to most radiation, meaning that photons can pass through the medium without being absorbed or scattered. The optical thickness  $\tau$  is wavelength dependent and is determined by the opacity  $\kappa$ , such that  $\tau = \int \rho \kappa dl$  where  $\rho$  is the column density and the integration is over the column length between the emission layer and the observer along the line of sight. The optical thickness is approximately the number of mean free paths before a photon is scattered or absorbed, meaning the point in the atmosphere where  $\tau_\lambda = 1$  represents where most of the observed light at wavelength  $\lambda$  originates. A high optical thickness means that the mean free path for photons is small, and the majority of photons passing through the medium will be absorbed or scattered.

In optically thick spectral lines (such as H $\alpha$  and Ca II 8542 Å), light from different points in the line can sample different heights in the atmosphere. A photon with exactly the line core wavelength, emitted deep in the atmosphere, has a small chance of passing through the upper parts of the atmosphere to escape and travel to the observer ( $\tau_\lambda$  is large). This means that light from the line core will typically emerge from a greater altitude than

## 2.1 Observational methods

light from the line wings. Formally, the intensity at some wavelength  $I_\lambda$  is the integral of the intensity contribution function  $C_I$  at each height  $z$  through the whole atmosphere;  $I_\lambda = \int C_I dz$  (Carlsson & Stein 1997). Estimates of the formation heights of spectral lines are found by one (or a combination) of: radiative transfer codes like RH (Uitenbroek 2001) which synthesise spectra based on an atmosphere; simulations of atmospheres with radiation included, such as the 3D radiative MHD code *Bifrost* (Gudiksen et al. 2011) or RADYN for 1D flare atmospheres (Carlsson & Stein 1992); and widely used semi-empirical model atmospheres such as VAL-C (Vernazza et al. 1981) or FAL-C (Fontenla et al. 1993).

$H\alpha$  is an important spectral line historically, and is one of the strongest chromospheric features in the solar spectrum. It is part of the Balmer series, and represents an electron transition between the  $n = 3$  and  $n = 2$  bound levels of hydrogen. It is located at  $\lambda = 6563 \text{ \AA}$ , in the optical range, and is characterised by its wide wings and strong core. It is thought to sample heights of  $\sim 1500 \text{ km}$  at its core and as low as  $\sim 200 \text{ km}$  in the wings (Vernazza et al. 1981).

The Ca II 8542  $\text{\AA}$  line is part of the calcium IR triplet, and has become prevalent in diagnoses of the solar atmosphere because it is far removed from other lines, meaning it is not blended, and is at a wavelength observable using ground-based telescopes. It is a magnetically sensitive line, meaning it can be used to probe magnetic fields with polarimetric datasets, and its core samples a thin range of altitudes in the middle chromosphere at around 1500 km from the surface.

Because of the variability of, for example, temperature stratification in the solar atmosphere, such as when comparing quiet Sun and active regions, chromospheric lines cannot be thought of as always sampling exactly the same altitudes. Leenaarts et al. (2012a) used 3D radiation-magnetohydrodynamic simulations to model  $H\alpha$  formation in a complex atmosphere, and found a large range of formation heights, 1500–2000 km, and reaching over 2500 km in magnetic structures such as fibrils.  $H\alpha$  and Ca II 8542  $\text{\AA}$  are usually thought to overlap, but Kuridze et al. (2015) found that  $H\alpha$  was formed higher in the atmosphere (1200 km) than Ca II 8542  $\text{\AA}$  (900 km) during a flare simulated using the RADYN radiative hydrodynamic code. In this case the two lines can complement each other, allowing a large height range for diagnostics.

The photospheric absorption line at 5250  $\text{\AA}$  is formed in neutral iron, and samples a height of approximately 300 km (Smitha & Solanki 2017). It is a suitable probe for the photospheric magnetic field, for example in Milne-Eddington (ME) inversions. The ME assumption is that the atmospheric parameters do not vary with height, except the source function (the ratio of emissivity to absorption), which varies linearly with optical depth.

## 2.1 Observational methods

This assumption is applicable at the photosphere, but chromospheric lines require more complexity.

### 2.1.3 Solar Dynamics Observatory

The Solar Dynamics Observatory (SDO: [Pesnell et al. 2012](#)) is operated by NASA and was launched in 2010, remaining in operation to this day. The observatory is situated in orbit around the Earth and houses three instruments: the Atmospheric Imaging Assembly (AIA: [Lemen et al. 2012](#)); the Helioseismic and Magnetic Imager (HMI: [Schou et al. 2012](#)); and the Extreme ultraviolet Variability Experiment (EVE: [Woods et al. 2012](#)). These instruments provide observations of the Sun in three key data types: imaging (AIA), magnetic field measurement (HMI) and high resolution spectroscopy (EVE).

#### Atmospheric Imaging Assembly

AIA consists of four 20-cm telescopes which use filters to select 10 separate wavelengths of light to image, each onto  $4096 \times 4096$  CCDs with a spatial scale of 0.6 arcseconds per pixel, imaging the whole solar disk out to  $0.5R_\odot$ . The telescopes image seven EUV wavelengths at 12 second temporal resolution spanning temperatures of  $\log_{10} T = 4.7 - 7.3$ , sampling the chromosphere to upper corona. Two UV bandpasses are imaged every 24 seconds, and a photospheric continuum image is taken every hour for calibration purposes. The AIA channels are summarised in Table 2.1.3, with their sampled atmospheric regions and characteristic temperatures. The region of atmosphere imaged by the two UV channels (1600 Å, 1700 Å) has not been well-defined, however a recent calibration study by [Simões et al. \(2019\)](#) found that both of these channels are dominated by chromospheric and transition region spectral lines in flaring data, and dominated by photospheric continuum emission in quiet Sun data. For this reason the UV channels can be used to study approximately the same region as the chromospheric lines in CRISP data. As seen in the Table 2.1.3, the EUV channels are sensitive to the corona, and extremely hot plasma associated with flares, making AIA an excellent diagnostic tool for their study.

#### Helioseismic and Magnetic Imager

HMI observes the photosphere using measurements of the Fe I 6173Å absorption line, imaging the whole solar disk with two cameras. The Doppler camera measures scalar

## 2.1 Observational methods

**Table 2.1:** The sampling of the various AIA UV and EUV filters (Lemen et al. 2012). Abbreviations: TMR, temperature minimum region; TR, transition region.

Channel name	Primary ion(s)	Region of atmosphere	$\log T$
white light	continuum	photosphere	3.7
1700 Å	continuum	TMR, photosphere	3.7
304 Å	He II	chromosphere, TR	4.7
1600 Å	C IV & cont.	TR & upper photosphere	5.0
171 Å	Fe IX	quiet corona, upper TR	5.8
193 Å	Fe XII, XXIV	corona, flare plasma	6.1, 7.3
211 Å	Fe XIV	active-region corona	6.3
335 Å	Fe XVI	active-region corona	6.4
94 Å	Fe XVIII	flaring regions	6.8
131 Å	Fe VIII, XX, XXIII	flaring regions	5.6, 7.0, 7.2

quantities such as continuum intensity, Doppler shift velocity, and line-of-sight magnetic field strength, at a cadence of 45 seconds. The Vector camera has a longer 135 second cadence and captures measurements to enable the vector magnetic field and some thermodynamical parameters to be inferred. However, to reduce noise, the final vector magnetic field data products and the individual Stokes parameters are available only at a 12-minute cadence (Hoeksema et al. 2014). The polarisation of the radiation is a consequence of Zeeman splitting, meaning we can measure the magnetic field with polarimetric observations. The vector field is calculated from the Stokes parameters using the Very Fast Inversion of the Stokes Vector (VFISV) code (Borrero et al. 2011, Centeno et al. 2014) which is an inversion code based on an ME atmosphere. The data products from HMI are freely available, meaning that we always have some idea of the photospheric field to accompany other observations.

## 2.2 Spectral analysis

The analysis in this thesis is focussed on the identification of oscillatory signals in data, usually without visually inspecting each timeseries. In many settings, this would be a simple task: transform the data into Fourier space, and select the frequency with the highest power. However, in many astrophysical systems real oscillatory signals exist atop a background spectrum of red noise, making the identification of oscillations tricky.

### 2.2.1 Power spectra

One of the most basic but powerful ways of identifying periodicities is by calculating a power spectrum corresponding to some timeseries. A power spectrum relays the prevalence (power) of signals at particular frequencies (or periods) that are present in the timeseries. Many different types of power spectra exist, but the one used throughout this thesis is the Fourier power spectrum. The Fourier power spectrum (FPS), is essentially a Fourier transform of the timeseries, converting a signal in time to frequency space. The frequency space that is sampled is determined by the limits of the timeseries. The highest frequency in the spectrum is called the Nyquist frequency and is calculated by  $1/2\Delta t$  where  $\Delta t$  is the timestep between data points. The total length of the timeseries affects the lowest frequency sampled which is found by  $1/N\Delta t$  where  $N$  is the number of data points. Because of this we must be careful when selecting datasets from which to determine periodicities. The cadence ( $\Delta t$ ) of a dataset is fixed for some instruments ( $\Delta t = 12$  s for AIA/EUV,  $\Delta t = 24$  s for AIA/UV) and variable for others, but high cadence will come at the expense of, say, spectral line coverage or the ability for polarimetric measurements. In order to identify a signal with a certain periodicity, one should make sure to chose a dataset with appropriate values for  $\Delta t$  and  $N$ . For example, a cadence of 10 seconds would be better suited to identifying 3-minute signals than those with periods of 20 seconds, and a time interval only 5 minutes long would be a poor choice for sources with 10-minute variability.

#### Calculating the Fourier power spectrum

We will now outline a standard practice for calculating the Fourier power spectrum of a timeseries, which we followed in our spectral analyses. First the timeseries must be normalised, by subtracting the mean and dividing by its standard deviation,  $\sigma$ . This is

## 2.2 Spectral analysis

necessary, as the Fourier power scales with the size of the fluctuations, making comparing results from locations with very different brightnesses redundant. Next, in a process called apodisation, a Hann window function is applied to the normalised signal. This is a function which smoothly falls to zero at either end of the timeseries. This removes any discontinuity between the first and last data points, reducing spectral noise, while maintaining the signals in the timeseries. The Fourier spectrum is obtained by: performing a Fourier transform on the apodised timeseries; removing negative frequencies and their associated amplitudes; taking the absolute value squared of the spectrum; finally normalising by the variance of the timeseries. The final normalisation is so that the result is of the same order as the global wavelet spectrum, seen later (Sections 2.2.3 and 2.2.6). This resulting spectrum is a measure of the power of a signal as a function of frequency or equivalently, period.

### 2.2.2 Signal detection in coloured noise

Noise is defined as any fluctuations in data that hinders the perception of signal. Noise exists in many forms and can come from many sources, for example photon counting uncertainty, instrumental effects, and systematic long-term variations. It is important to understand the type of noise present in any timeseries which is being studied. Different types of noise are often described by their colour, for example white, red, and pink. For the purposes of illustration, in this section we have generated different simple timeseries meant to represent various types of signal. We have generated the signals over a realistic time axis representing an observation with  $\Delta t = 12\text{ s}$  and  $N = 250$ , hence a total time interval of 50 min.

Coloured noise models have power spectra that are described as power laws, and exist of the form

$$P(f) = Af^{-\alpha}, \quad (2.8)$$

with  $P(f)$  describing the power as a function of frequency,  $A$  being a scaling factor and  $\alpha$  the power index. The value of  $\alpha$  defines the colour of the noise. When plotted on logarithmic axes the power law will be a straight line with slope  $\alpha$  and vertical offset  $A$ .

## 2.2 Spectral analysis

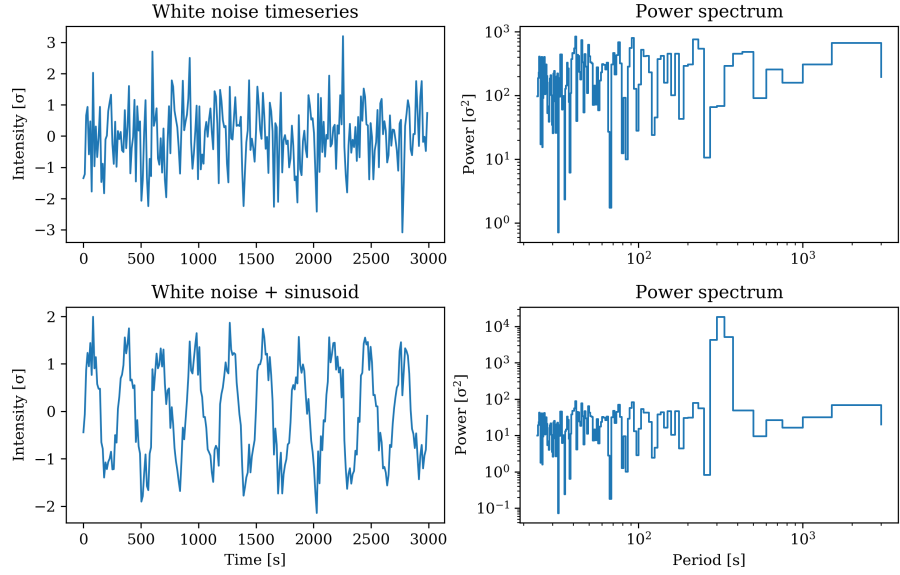


**Figure 2.2:** Synthetic timeseries generated over a realistic time axis on a white noise background, and corresponding power spectra. Top row: timeseries with no signal. Lower row: Same as first row with an added sinusoid with period 300 seconds.

### White noise

The term “white noise” is used to describe fluctuations which have approximately equal power at every frequency (analogous to white light), for example photon counting noise. The spectral index for white noise is  $\alpha = 0$ , and its power spectrum is flat, an example of which is seen in the top row of Figure 2.2. This was generated using Gaussian noise centred on zero, with a standard deviation of unity, over the time axis described above. We see that the signal is devoid of clear oscillatory signals and the power at all frequencies is approximately equal.

In the lower row of Figure 2.2 we show the same white-noise timeseries but with an added sinusoidal signal. The signal has a constant period of 300 seconds and this clearly dominates the power spectrum in the lower right panel. The power at  $\sim 300$  seconds is orders of magnitudes higher than the rest of the spectrum, which is flat and lies at a much lower power level than in the spectrum of the pure white noise (upper right panel).

## 2.2 Spectral analysis

### Red noise

Red noise is so named because it gives more strength to signals at low frequencies. It is also known as Brown noise — named for the botanist Robert Brown, not the colour. Brownian motion (Brown 1828, Einstein 1905) is present in all sorts of physical systems because it represents “random walks”. It is suitable for describing variations seen in flare data because we expect longer period signals to be more energetic, with small amplitudes for smaller timescale fluctuations. In fact, red noise is the natural result of a superposition of many small scale energy deposition events (Auchère et al. 2016). Some sources assign red noise a specific spectrum with  $\alpha = 2$ , while “pink” noise is  $\alpha = 1$ , but for simplicity we refer to red noise as any spectrum with  $\alpha > 0$ . Red-noise spectra are observed in a range of astrophysical conditions such as Seyfert galaxies (Vaughan 2005) and magnetars (Huppenkothen et al. 2013).

A synthetic red-noise timeseries was created over the same realistic time axis used for the white noise case, to simulate a solar intensity observation. The “random walk” was generated by integrating a white-noise signal centred on zero, each datapoint being travelled to from the last. The resulting timeseries and its Fourier spectrum are shown in the top row of Figure 2.3, and we see that the spectrum increases at longer periods (lower frequencies).

Similarly to the white noise case, we simulated an oscillatory signal on top of the background noise at a period of 300 seconds, shown in the middle row of Figure 2.3. In the white-noise spectrum (lower row, Figure 2.2), the oscillation period was orders of magnitude higher than the rest of the spectrum, and the periodicity could be found by selecting the frequency bin with the highest power. In this case, however, despite the oscillation being strongly visible in the timeseries, the power of the signal is just barely above values at the long-period end of the spectrum.

A third red-noise timeseries was generated, this time with the addition of a rapid brightening and exponential decay, in addition to the 5-minute oscillation. This is to simulate the effect of the bursty, almost step-function-like intensity increases which are seen in flaring pixel timeseries, with a gradual dimming after the initial impulse. The burst has a significant effect on the resulting power spectrum, seen in the lower row of Figure 2.3. It adds power at a wide range of frequencies, making signals of middling periods seem more significant, and suppressing the previously strong peak at the oscillating period. This represents a challenge in flaring datasets, especially when looking pixel-to-pixel, as

## 2.2 Spectral analysis

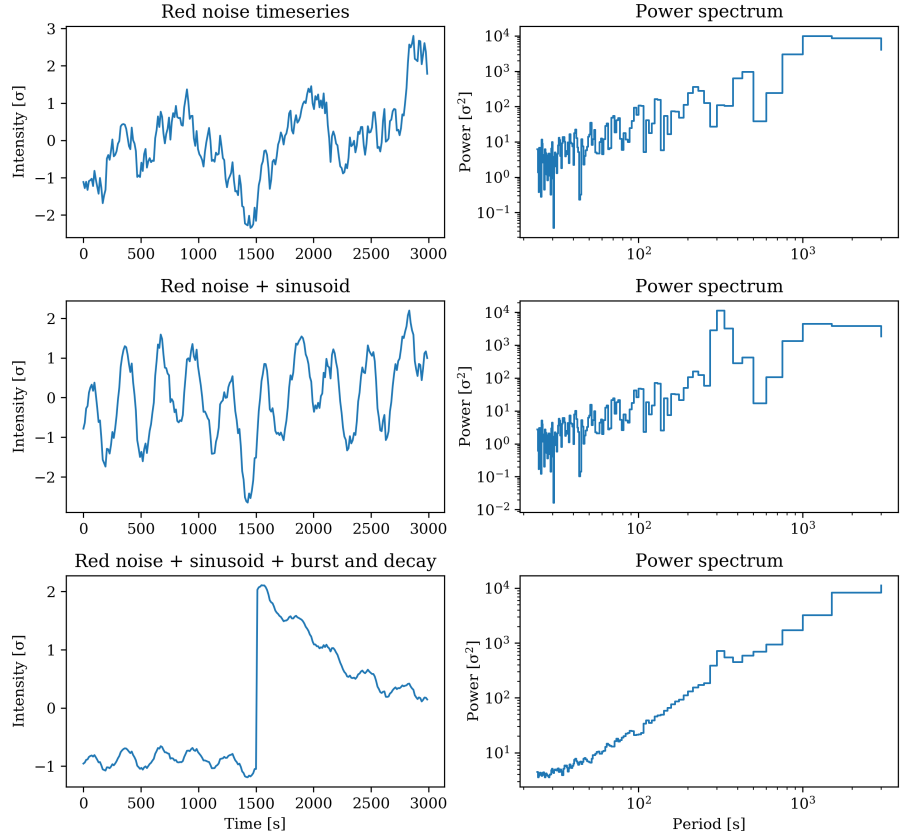


**Figure 2.3:** Synthetic timeseries (left column) to demonstrate various types of signal on a red-noise background, and their corresponding power spectral densities (right column). The timeseries represent: red-noise background with no additional signals (top), red noise with a sinusoidal wave added (middle), and a red-noise background with sinusoid and a steep burst with exponential decay (bottom).

rapid increases to brightness can make identifying oscillations very difficult, even when they are obvious to the eye.

### Problems with power

One popular method of analysing periodicities in solar active regions is the construction of “power maps”. The power spectrum is computed at each location, and the value of power at specific frequencies is then plotted over some field of view. Often the power in a small band of frequencies (e.g. 3–4 mHz) is selected instead. This is necessary as there is a certain amount of noise in the power spectrum itself, caused by the red-noise nature of

## 2.2 Spectral analysis

timeseries fluctuations. However, selecting a single frequency or band of frequencies can be a problematic approach.

Consider a search for 5-minute periodicities in the synthetic spectra presented in Figures 2.2 and 2.3. The power averaged over the five period bins around 300 seconds in the timeseries of the sinusoid on top of white noise (lower row, Figure 2.2) is approximately  $6 \times 10^3$ , while the power averaged over the same five bins of the sinusoid over red noise is around  $3 \times 10^3$  (middle row of Figure 2.3). So on a power map, one value is twice as powerful as the other, even though the oscillatory signal is exactly the same, and they differ only in the shape of their background noise spectra. The conclusion that there exists a stronger signal in one or the other is incorrect, because the whole spectrum is not taken into account.

Likewise, consider a search for periodicities with lengths of 3 minutes in the synthetic red-noise timeseries of Figure 2.3. Taking the average of the FPS in five bins centred at 180 seconds, the power values for each spectrum in this figure are 110, 49, and 100, respectively. This means that the timeseries made up of red noise with an added 5-minute signal would display a power drop at 3-minute periods of over 50% compared to the pure red noise, when in reality we have not removed 3-minute periodicities from the data. Comparing the timeseries with the sinusoid to the timeseries with the additional burst and decay, the 3-minute power is almost double in the latter. In the case of real data, one might report an increase in 3-minute periods in chromospheric intensity when really the pixel exhibits obvious and perpetual oscillations at a very different timescale, but has experienced a rapid brightening, which led to a false result.

With these examples we have demonstrated how comparing power at a single frequency or a frequency window can lead to false results, and missed periodicities that might be present in data. Another point of note is that a frequency window of, say, 1–2 mHz covers signals with periods of 500–1000 seconds. Combining signals within a vast range of periods such as this means valuable information can be lost, such as a periodicity growing in length. We conclude that while it is possible to gain some understanding of the oscillations in a dataset by focussing on certain frequencies and using power maps, it is susceptible to misleading results and we are much better off considering the spectrum as a whole.

### 2.2.3 Wavelet analysis

Analysis using Fourier power spectra has one significant drawback, that it has no time resolution. The whole timeseries is transformed into a one-dimensional spectrum, making

## 2.2 Spectral analysis

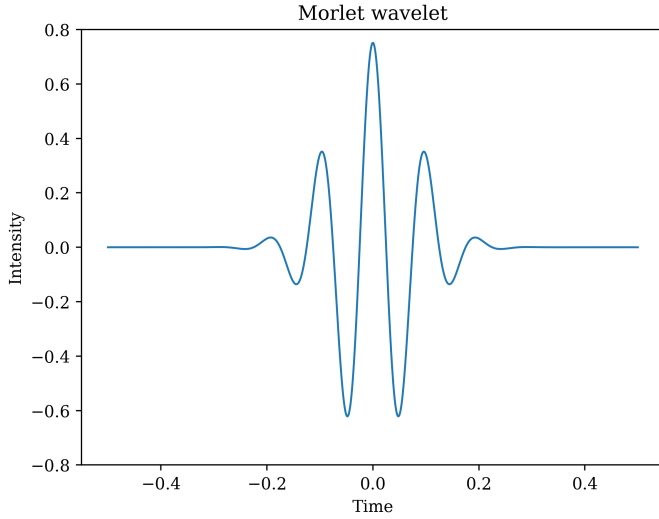


**Figure 2.4:** Example of a Morlet wavelet. This localised wave packet is the combination of a sine wave and a Gaussian.

it less than ideal to study QPP which are by nature transient. Wavelet analysis can provide an answer to this problem, because it gives information about periodic components of a signal as a function of time. The Wavelet Power Spectrum (WPS) is similar to the Fourier power spectrum, but is a two-dimensional function, giving power as a function of period and time. Wavelet analysis often follows the method outlined by [Torrence & Compo \(1998\)](#). This analysis technique has often been used to characterise QPPs ([Simões et al. 2015](#), [Milligan et al. 2017](#), [Dominique et al. 2018](#)).

The wavelet transform  $W_n$  of a timeseries  $x_n$  is found by the convolution of the series with a wavelet function – a small pulse localised in time and frequency space with zero mean. There are many types of wavelet function, but the most commonly used is the Morlet wavelet – a plane wave modulated by a Gaussian. An example of the Morlet wavelet is shown in Figure 2.4, and is calculated by

$$\psi(\eta) = \pi^{-1/4} e^{i\omega_0\eta} e^{-\eta^2/2}. \quad (2.9)$$

$\omega_0$  and  $\eta$  are non-dimensional frequency and time parameters respectively. The wavelet transform of a series with constant time spacing  $\Delta t$  is found by convolution with a scaled

## 2.2 Spectral analysis

and translated version of  $\psi(\eta)$ :

$$W_n(s) = \sum_{n'}^{N-1} x_{n'} \psi^* \left( \frac{(n - n')\Delta t}{s} \right). \quad (2.10)$$

The scale  $s$  determines the frequency (or equivalently, period) of the measured wavelet transform, and the asterisk ( $*$ ) denotes the complex conjugate. Computationally, this convolution is performed by applying fast Fourier transforms and using the convolution theorem: the Fourier transform of a convolution of two functions is equal to the product of the Fourier transforms of each function. The WPS at each point in the timeseries and at each scale is then  $|W_n(s)|^2$ .

After obtaining the WPS, it is often plotted on a periodogram, showing signal strength as a function of time and scale. Red-noise backgrounds necessitate careful significance testing in such studies. [Auchère et al. \(2016\)](#) evaluated whether the significance testing provided in the [Torrence & Compo \(1998\)](#) wavelet codes was appropriate, and found that the red-noise background included in the code was not valid for many timeseries, and should not be applied blindly.

### Averaged wavelet spectra

To understand the wavelet power over an entire timeseries, the wavelet power spectrum can be averaged along the time axis, resulting in the global wavelet spectrum (GWS). This is functionally very similar to the simple Fourier spectrum, and when normalised correctly can be used as a proxy for the Fourier power spectrum, with the advantage that it is often a smoother function.

Similarly, the WPS can be averaged over its scales, usually in a small range of periodicities. This results in the scale-averaged wavelet spectrum, and can be used to measure how the strength of a signal changes over the course of the timeseries.

#### 2.2.4 Detrending methods

Because variations in flux are small compared to the background trends, many authors have taken to removing large scale variations in QPP timeseries before applying Fourier or wavelet analysis to the data. This process involves obtaining a “smoothed” version of the lightcurve and subtracting this from the original.

## 2.2 Spectral analysis

A Fourier filter can be applied to data, by first performing a Fourier transform and removing part of the spectrum above some cut-off frequency. Inverse transforming the remaining spectrum results in a signal which has only large frequency (hence small timescale) components. This method was used by [Milligan et al. \(2017\)](#) but carries the risk of artificial power being generated at around the cut-off frequency. The power increases steadily with period in a red noise spectrum, so if all the power at large periods is removed, it can appear that the periods just below the filter point are more significant.

A simpler detrending method is to obtain a running average of data points, using a convolution of a flat window function over the timeseries [Dolla et al. \(2012\)](#). The window function can be varied in width, and this width would determine the length of signals which are smoothed out by this method. A similar functionality can come from a Savitsky-Golay filter ([Savitzky & Golay 1964](#), [Schafer 2011](#)), a process where an  $n$ -order polynomial is fitted to the lightcurve over a variable window length. While this function can be used to more accurately smooth a timeseries, it is more difficult to characterise any possible artificial signals added in the process. Another issue is that any random noise fluctuations in the original datapoints will not be independent after the smoothing process.

The final detrending method discussed here is the digital derivative method. A (say) linearly increasing timeseries with a small sinusoidal fluctuation, when differentiated will have the linear element removed, but the sine-like part will become cosine-like, the periodicity intact. This method has been used by ([Simões et al. 2015](#), [Hayes et al. 2016](#)), however, it requires extremely high signal-to-noise ratios, as small noise fluctuations can be amplified by the differentiation process. It is more appropriately used for signals such as GOES SXR flux, rather than pixel-to-pixel intensity fluctuations.

The process of detrending data must be treated carefully, as the procedure has a tendency to introduce artificial signals, particularly in wavelet analysis ([Auchère et al. 2016](#)). For example, a boxcar smoothing method such as that used in [Dolla et al. \(2012\)](#) with a width  $\delta t$  will introduce a sinc term in the power spectrum:  $\sin(\pi f \delta t)/\pi f \delta t$ .

### 2.2.5 The spectral fitting method

It is pertinent to avoid interfering with the original timeseries by detrending, if possible. We saw in Section 2.2.2 that it is also important to consider the entire power spectrum in the analysis, rather than focussing on specific periods. The method which we use also has to be applied blind to thousands of timeseries, and so necessarily has to be fairly

## 2.2 Spectral analysis

simple and not computationally expensive. Our preferred method will be referred to as the “spectral fitting method”, and it involves identifying localised bumps of power on top of background noise spectra.

[Vaughan \(2005\)](#) studied oscillatory signals that had been reported from X-ray binaries and Seyfert galaxies, and demonstrated a method of testing the significance of a signal in the red-noise spectrum. The method involved first performing a straight line fit on the (log-space) power spectrum and using the result to determine a significance level to test the prevalence of spurious frequency bins in the data. This test was adapted to solar QPP data by [Gruber et al. \(2011\)](#), who tested data from the Gamma-Ray Burst Monitor (GBM) on the Fermi satellite, in which QPP had been reported by previous studies. It was found that, when considering the power-law nature of the power spectrum, no significant oscillations were found in the data other than the 4-second rotational period of the spacecraft.

Building on these previous studies, [Inglis et al. \(2015\)](#) reevaluated QPPs which had been reported in high energy and radio data from several flares, by using two different models for the power spectra, and comparing how well the data were described by each. The first model was a double power-law, describing a red-noise spectrum combined with a white-noise spectrum (with index 0), and the second model was similar to the first but included a Gaussian bump in the spectrum, representing the excess power introduced by significant oscillations. Using Bayesian methods for fitting and comparing the spectra, it was found that only one of the 19 timeseries favoured the bump in the spectrum.

### Variations of the method

The method presented by [Inglis et al. \(2015\)](#) has been used in other works ([Inglis et al. 2016](#), [Auchère et al. 2016](#), [Threlfall et al. 2017](#), [Battams et al. 2019](#)) with slight variations. [Inglis et al. \(2016\)](#) introduced a third model to describe the spectra, a broken power law, motivated by the idea that a single-index power law might not adequately describe flare spectra. A variation presented by [Auchère et al. \(2016\)](#) fits a kappa function instead of the Gaussian bump used by [Inglis et al. \(2015\)](#). [Threlfall et al. \(2017\)](#) followed Auchère’s method, applying it to long-period variations in data from AIA and the Solar TErrestrial Relations Observatory (STEREO). In this variation, a significance level was placed above the kappa-shaped model and individual bins of power were identified which surpassed that level.

While there have been theories put forward as to why a power-law noise spectrum describes a solar timeseries, for example due to many small energy deposition events

## 2.2 Spectral analysis

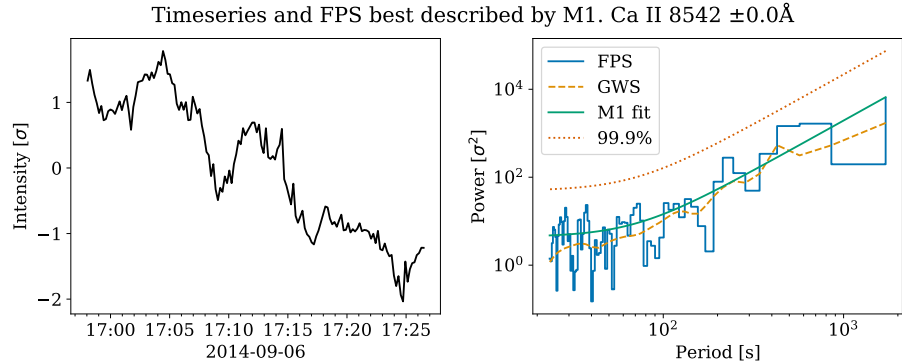


**Figure 2.5:** The timeseries (LH panel) and corresponding Fourier power spectra (RH panel) taken from the line core of Ca II 8542 Å at a location far from the main sunspot and the flare activity. Plotted with the FPS (blue stepped line) is the global wavelet spectrum (yellow dashed line), the mean spectrum fit by M1 (green line) and the 99.9% significance level (orange dotted line, explained in Section 2.2.7).

(Aschwanden 2011), there is little explanation for why an FPS should take the shape of a Gaussian bump or kappa function, as opposed to any other shape. Battams et al. (2019) used a Lorentzian bump instead of Gaussian, motivated by its physical meaning in the context of a damped oscillator.

### 2.2.6 Description of the spectral fitting method

The process of fitting models to the Fourier spectra of timeseries was selected for our analyses, by combining various aspects of the approaches used by the authors described above. We will now outline our process step by step, with a summary afterwards.

#### Spectrum models

Beginning with the timeseries we wish to analyse, its Fourier power spectrum is obtained by the method described in Section 2.2.1. We then use three different models to categorise the shapes of observed power spectra: red-noise background, red-noise with Gaussian bump, and red-noise with a kappa function. We use, as examples of each of these, timeseries drawn from the data described in Chapter 3 which are displayed in Figures 2.5–2.7.

The first model (M1: equation 2.11) which is used for the spectra is a power law with an additional constant,  $C$ , to describe a white-noise element in the data from photon

## 2.2 Spectral analysis

counting (technically this is two power laws summed together, one of which has index  $\alpha = 0$ ):

$$M1 = Af^{-\alpha} + C. \quad (2.11)$$

In Figure 2.5 a spectrum is shown for which the power-law noise model (M1) was preferred, and shows the types of random variations which can be attributed to coloured noise. The timeseries in the left panel was drawn from the line core of Ca II 8542 Å at a “quiet Sun” location. The power spectrum is displayed in the right panel, along with the M1 fit (solid line). The global wavelet spectrum (GWS) is plotted as a dashed line, and can be seen to follow the overall shape of the FPS quite closely. We also display the 99.9% significance level, showing that no signals in this spectrum deviate from the red-noise background.

The second model (M2: equation 2.12) includes a Gaussian bump term (Inglis et al. 2015) which is used to indicate enhanced oscillatory power in addition to the power described by M1. An additional three parameters are introduced to describe the height ( $B_G$ ), width ( $\sigma$ ) and position of the peak in frequency space ( $\beta$ ):

$$M2 = M1 + B_G \exp\left(\frac{-(\ln f - \beta)^2}{2\sigma^2}\right). \quad (2.12)$$

In Figure 2.6 we show an example of a spectrum with M2 as the preferred model. The spectrum shown in this figure is clearly of a different shape to its equivalent in Figure 2.5, and it is well described by a bump rising above the power-law spectrum. The timeseries has a clear oscillatory signal which produces an FPS with a clear increase of power around the approximate period of the oscillations. The exact length of each oscillation is not equal, and so the signal in the FPS is spread out somewhat, producing the bump. The parameter  $\beta$  gives us an idea of the most common periodicities observed in the timeseries, and can be converted to a period via  $e^{-\beta}$ .

The third model (M3: equation 2.13) to describe the shape of spectra was used because we observed cases where the FPS would appear to level off below certain frequencies, and this behaviour could not be described accurately by M1 or M2. It utilises a kappa function, similar to studies by Auchère et al. (2016) and Threlfall et al. (2017):

$$M3 = M1 + B_K \left(1 + \frac{f^2}{\kappa\rho^2}\right)^{-\frac{\kappa+1}{2}}. \quad (2.13)$$

## 2.2 Spectral analysis

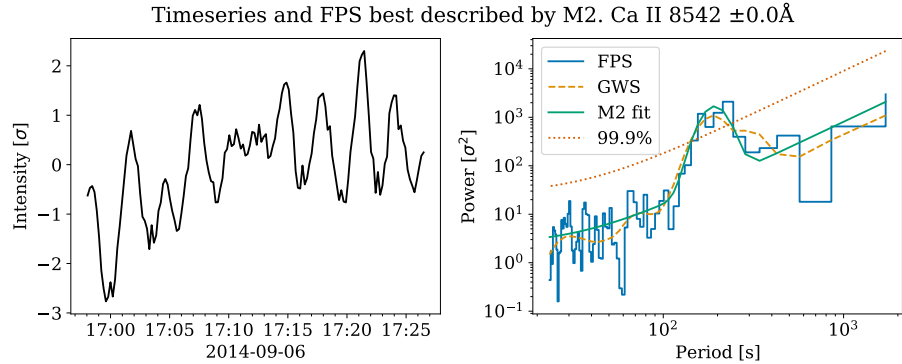


**Figure 2.6:** As in figure 2.5, but showing a timeseries from over a sunspot umbra. The confidence threshold (orange dotted line) is shown corresponding to the noise background with the bump removed. The peak of the Gaussian bump occurs at  $\beta = -5.26$  which corresponds to a period of  $\approx 190$  s.

In the above equation,  $\rho$  describes the width of the kappa function,  $\kappa$  describes its extent into the high-frequency wing, and  $B_K$  gives its height. An example of a spectrum which was well-fit by M3 is shown in Figure 2.7. It is clear from the timeseries that there is oscillatory behaviour here, however it is not sufficiently well localised to any particular frequency to create a defined bump. While it is possible that the kappa function gives some information about oscillatory behaviour it is more complex to define than the Gaussian bump case. In Figure 2.7 the oscillations are drifting in period over the  $\sim 30$  minute window, which could create a wide increase in power which manifests in the kappa shaped bulge. An apparent flattening of the spectrum could be caused by enhanced power at shorter periods or a decrease in power at longer periods, perhaps a sign of white noise dominating at both ends of the spectra. It is possible that the M3 shape depicts a manifestation of the cut-off frequency described in Section 1.3.3, in a timeseries with no prevalent single period. In the context of this analysis, these models can be seen as tools to identify FPSs which deviate from simple coloured noise, rather than descriptors of the physical processes behind the observed timeseries and Fourier spectra.

The fitting process was performed in Python using the `curve_fit` function from the `scipy` library (Virtanen et al. 2020). The algorithm minimizes a  $\chi^2$  function of the form

$$\chi^2 = \sum_i^N \left( \frac{y_i - M(f_i, \mathbf{p})}{\sigma_i} \right)^2, \quad (2.14)$$

where in this case  $y$  is the power spectrum (of which there are  $N$  values),  $f$  is the set

## 2.2 Spectral analysis

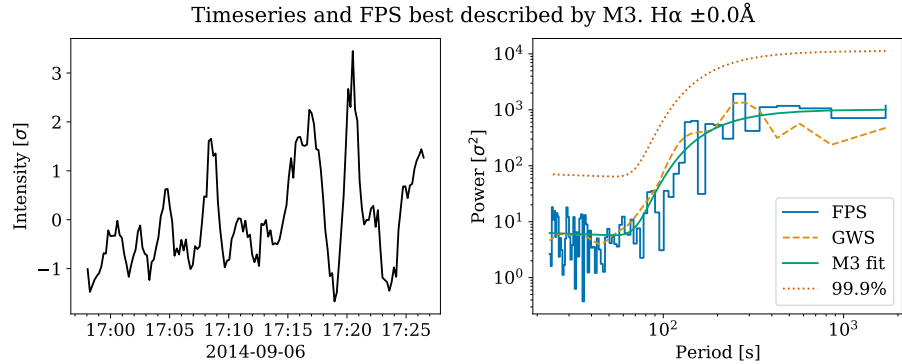


**Figure 2.7:** Similar to figures 2.5 and 2.6, but for a timeseries from the core of H $\alpha$  over the sunspot penumbra, where the preferred model was the kappa function (M3).

of frequency values,  $\mathbf{p}$  is a vector of parameters used in the model  $M$ , and each data point is weighted by  $1/\sigma_i$ . The individual data points for the power spectra span many orders of magnitude, so the weights are chosen to make each frequency point comparable. Following Auchère et al. (2016), the global wavelet spectrum (GWS) was used as a weighting function.

### 2.2.7 Determination of the preferred model

Identifying true oscillatory signals above noise is a very difficult task without visually inspecting each timeseries and spectrum, and therefore we set a number of criteria that each spectral fit must first meet. The first criterion to identify an M2 fit is that the Gaussian bump model must describe the observed data better than M1 and M3, based on a weighted residuals squared (WRS) measurement of each fit (of the same form as equation 2.14). M2 and M3 have three more free parameters than M1, and so these would be expected to produce a better fit in most circumstances. An F-test is used when comparing models with different numbers of parameters as in Battams et al. (2019), with the F-statistic defined as:

$$F = \frac{\left( \frac{WRS_1 - WRS_2}{k_2 - k_1} \right)}{\left( \frac{WRS_2}{N - k_2} \right)}. \quad (2.15)$$

In this equation,  $k$  is the number of parameters for each model and  $N$  is the number of data points in the spectrum. The null hypothesis for the F-test is that M1 describes the

## 2.2 Spectral analysis

data as well or better than M2 (or M3) and a  $p$ -value to reject it is obtained based on the value of  $F$  in the  $F(k_2 - k_1, N - k_2)$  distribution. It should be noted that a  $p$ -value below the threshold does not indicate that M2 (or M3) describes the data perfectly (or well at all), just that it is preferred over M1, and the test can be expected to be wrong a fraction of the time, determined by the  $p$ -value.

Spectra which are best described by M2 and which pass this F-test were then identified to have two main components: a Gaussian bump and a background noise spectrum described by M1. The background spectrum is found by using the parameters from the M2 fit, but setting the  $B_G$  parameter to zero, removing the bump. The significance of the bump was tested against the background noise level, based on a confidence threshold obtained using the parameter  $m$  from the following equation:

$$m = -\ln(1 - X^{1/N}). \quad (2.16)$$

This equation states that each of the  $N$  frequency bins of the Fourier spectrum has a probability  $X$  of being  $m$  times greater than the background noise spectrum. It is obtained from the fact that the Fourier spectrum is  $\chi^2_2$  distributed around the mean power value at each frequency, and is explained fully in [Auchère et al. \(2016\)](#). The spectral bump is taken to be significant if the fitted spectrum is more than  $m$  times the background spectrum at some confidence level (e.g. 99.9%). By applying these two different significance tests to the data the likelihood of identifying a timeseries which does not contain a significant deviation from the standard background noise was greatly reduced.

The final step in determining the significance of each Gaussian bump, was to remove results which contained bumps close to the edges of the spectra. This range was necessary because of the limitations of the data, that is, the cadence setting a lower limit to the detectable periods and the total length of each timeseries setting an upper limit.

### 2.2.8 Summary of the spectral fitting method

The method described above can be used to search for oscillatory signals in a variety of timeseries. For instance, we use this process for intensity data from several CRISP spectral lines in Chapters 3 and 5, as well as AIA UV channel intensity in Chapter 3 and velocity timeseries in Chapter 5. We summarise the process in a flow chart in Figure 2.8.

## 2.2 Spectral analysis

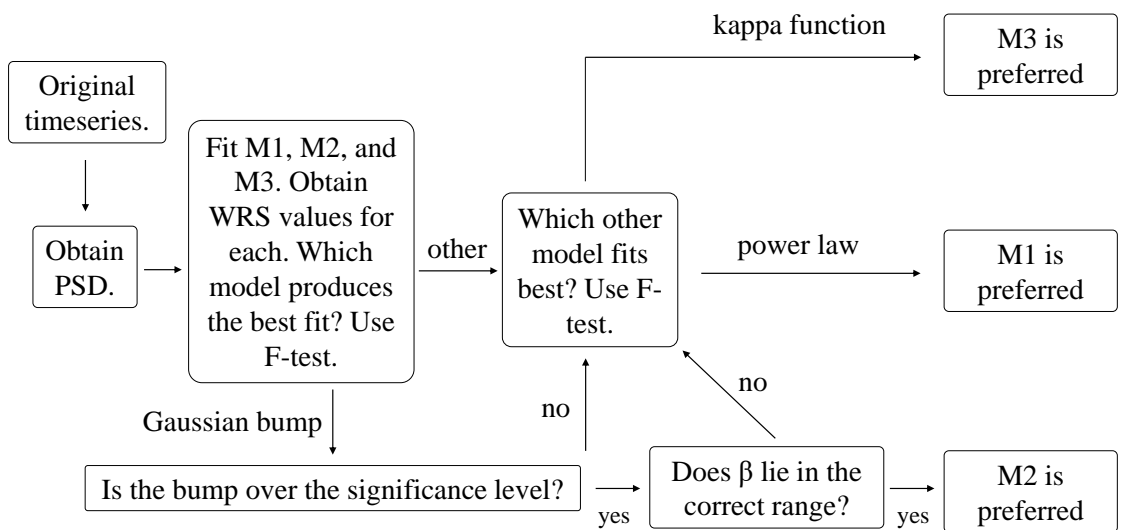


**Figure 2.8:** The spectral fitting method used throughout this thesis, including the significance testing steps outlined in Section 2.2.7.

## 2.3 Measurements and inversions

As we observe the Sun from afar, all the information we can learn about the atmosphere is derived from the light we receive. The process of obtaining physical parameters of the solar atmosphere from spectropolarimetric observations is called an inversion (del Toro Iniesta & Ruiz Cobo 2016, de la Cruz Rodríguez & van Noort 2017). Through the study of radiative transfer, we know (approximately) what the resulting spectra produced from the solar atmosphere should look like, an inversion is just the reverse of this process. However, one of the problems with inversion methods is that there is a degeneracy in the resulting spectra — two different atmospheres can produce the exact same result.

Inversion codes need to make assumptions about the atmosphere they are investigating. This is necessary because the underlying model atmosphere is used to test how well the inversion has been performed. Many codes synthesise spectra from a model atmosphere with some physical parameters (starting from an initial guess model), before changing the parameters slightly and recalculating, to see if the result improves.

The assumption of local thermodynamic equilibrium (LTE) is reasonable when considering, for example, only photospheric spectral lines. A Milne-Eddington atmosphere is, again, applicable for some lines with small ranges to their formation height for example the HMI VFISV (Borrero et al. 2011). Including lines formed higher in the atmosphere makes the LTE condition fail, and non-LTE conditions must be adopted. Most inversions assume that the atmosphere is one-dimensional, mostly because solving the radiative transfer equation in higher dimensions is incredibly complicated.

It is possible to gain information about how physical parameters are stratified in the atmosphere with some codes (e.g. NICOLE, Socas-Navarro et al. 1998), however it is important that atmospheric height dependency is not over-fit by the code. It is possible to arrive at an atmosphere which perfectly reproduces spectropolarimetric observations, but which does so by generating a temperature profile which is un-physical.

### 2.3.1 STiC

The STockholm inversion Code (STiC: de la Cruz Rodríguez et al. 2019, 2016) is an MPI-parallel non-LTE inversion code that utilises a modified version of the radiative transfer synthesis code RH (Uitenbroek 2001) to solve atom population densities assuming statistical equilibrium and plane-parallel geometry. It allows including partial redistribution

### 2.3 Measurements and inversions

(PRD) effects of scattered photons (Leenaarts et al. 2012b) and the radiative transport equation is solved using cubic Bezier solvers (de la Cruz Rodríguez & Piskunov 2013). STiC’s inversion engine uses an equation of state extracted from the Spectroscopy Made Easy code (SME: Piskunov & Valenti 2017).

The code works on a column-by-column basis and uses plane-parallel geometry. The starting model atmosphere is an input to the code, and requires values for the temperature  $T$ , line-of-sight velocity  $v_{LOS}$ , the turbulent velocity  $v_{turb}$ , line-of-sight magnetic field strength  $B_{\parallel}$ , horizontal field strength  $B_{\perp}$ , and the azimuthal angle of the magnetic field  $\phi$ . For the inputs to the code and all output atmospheres, the stratification of these six parameters is defined in terms of  $\log \tau_{5000}$ , the logarithm of optical depth at 5000 Å (often styled as simply  $\log_{\tau}$ ). The code can also work in terms of column mass or geometrical height. The gas pressure is derived from the equation of state assuming hydrostatic equilibrium. The electron pressure is found by assuming hydrogen is the main electron donor, and using RH to solve the statistical equilibrium equations for the hydrogen atom.

The stratification of parameters is defined by *nodes*. These are the free parameters of the model, and represent fixed points in the atmosphere from which the height profiles of the parameters are interpolated. It is important to chose the number of nodes correctly, as too many can lead to oscillatory behaviour of the parameters, and an over-fitted solution. The computation time also increases with the number of nodes, another reason to try and use the smallest number of nodes possible, while still returning meaningful results. Larger numbers of nodes are needed for the parameters which vary more throughout the atmosphere, such as temperature.

The code is underpinned by the Levenberg-Marquardt non-linear least squares minimization algortihm (LM: Levenberg 1944, Marquardt 1963). The LM algorithm applies corrections to the parameters of a function and seeks to minimize a  $\chi^2$  value, to return the best set of parameters that fit the observed data. In the STiC code, the standard  $\chi^2$  is modified by a regularization term, with  $\Lambda$  being the overall regularization weight and  $r(\mathbf{p})$  is the regularization as a function of the parameter space  $\mathbf{p}$ :

$$\chi^2 = \frac{1}{N_{\lambda}} \sum_{\lambda}^{N_{\lambda}} \frac{(O_{\lambda} - S_{\lambda}(\mathbf{p}))^2}{w_{\lambda}^2} + \Lambda r(\mathbf{p})^2. \quad (2.17)$$

In this equation,  $O$  represents the observed values,  $S$  the synthetic spectrum, and  $w$  the weighting applied, at each value of wavelength  $\lambda$ . The weighting values and the form of regularization can be modified to best suit the needs of the user. For instance, more weight

### 2.3 Measurements and inversions

is often granted to the  $Q$ ,  $U$ , and  $V$  Stokes parameters so that they influence the result more than  $I$  (this is done by reducing  $w$ ). We in fact use multiple different regularization functions, in order to apply different kinds of penalties on the various physical parameters. For instance, we can penalise changes in the gradient of a parameter, changes in the second derivative, or changes from a constant value.

The result of the code is an output model atmosphere, and the best-fit synthetic spectrum on the same wavelength grid as the observed spectrum. STiC has been applied in the study of various phenomena including chromospheric plage heating (Morosin et al. 2022), chromospheric fibrils (Kianfar et al. 2020), magnetic field configurations (Pietrow et al. 2020), and solar flares (Yadav et al. 2021).

#### 2.3.2 The weak-field approximation

The weak-field approximation (WFA: Degl’Innocenti & Degl’Innocenti 1973) is a powerful tool because it enables measurement of the magnetic field vector using a small amount of computing power compared to inversion codes such as NICOLE and STiC. The WFA is an approximate solution to the radiative transfer equation, that lets us predict the Stokes polarisation parameters for a spectral line  $Q$ ,  $U$  and  $V$  as a function of Stokes  $I$  and its derivatives, under some assumptions. The assumptions are that the magnetic field does not change over the depth we observe and that the line splitting due to the Zeeman effect ( $\Delta\lambda_B$ ) is significantly smaller than the Doppler width of the line ( $\Delta\lambda_D$ ). Care must then be taken, as we know that the magnetic field is stronger in the photosphere than in the chromosphere (Joshi et al. 2016). In the case of a line like Ca II 8542 Å where the wings sample much lower in the atmosphere than the core, the WFA approximation applied to whole line will give muddied results. The second assumption, that  $\Delta\lambda_B \ll \Delta\lambda_D$  can be written as a condition for the field strength  $B$  (Asensio Ramos 2011):

$$B < \frac{4\pi m_e c}{\bar{g}\lambda_0 e} \sqrt{\frac{2kT}{M} + v_{turb}^2}. \quad (2.18)$$

In the above equation  $m_e$  is the electron mass,  $c$  the speed of light,  $\bar{g}$  the effective Landé factor,  $\lambda_0$  the central wavelength of the line,  $e$  the electron charge,  $k$  Boltzmann’s constant,  $T$  the temperature,  $M$  the mass of the element which produces the line, and  $v_{turb}$  is the turbulent velocity. This condition for the magnetic field strength is often broken for photospheric lines over sunspots, but for chromospheric lines with low Landé factors ( $\bar{g} = 1.10$  for Ca II 8542 Å) and large Doppler widths due to the higher temperature of

### 2.3 Measurements and inversions

the chromosphere, the condition is more often met. The Ca II 8542 Å line has been used frequently for magnetic field measurement using the WFA (Pietarila et al. 2007, Kleint 2017, Morosin et al. 2020). Centeno (2018) studied the validity of Ca II 8542 Å WFA measurements by synthesising polarimetric data from a variety of atmospheric conditions and seeing if the WFA returned the correct field, and found that the line-of-sight magnetic field could be reliably measured up to  $\sim 1200$  G.

The following equations relate the other Stokes parameters to the derivatives of  $I$  (Degl’Innocenti & Landolfi 2004, Asensio Ramos 2011):

$$V(\lambda) = C_1 f_B B_{\parallel} \frac{\partial I(\lambda)}{\partial \lambda}; \quad (2.19)$$

$$Q(\lambda) = C_2 f_B B_{\perp}^2 \sin 2\phi \frac{\partial^2 I(\lambda)}{\partial \lambda^2}; \quad (2.20)$$

$$U(\lambda) = C_2 f_B B_{\perp}^2 \cos 2\phi \frac{\partial^2 I(\lambda)}{\partial \lambda^2}. \quad (2.21)$$

These equations incorporate the magnetic filling factor  $f_B$ , the line-of-sight and horizontal magnetic field strengths  $B_{\parallel}$  and  $B_{\perp}$ , the field azimuth angle  $\phi$ , and the constants  $C_1$  and  $C_2$ . We cannot always measure precisely the fine magnetic structures in the atmosphere, so the factor  $f_B$  is a measure of the fraction of the magnetic signal that the source is sensitive to. This will be set to unity for our analysis.

We will focus our analysis on the equation relating Stokes  $V$  to the line-of-sight magnetic field strength  $B_{\parallel}$  (equation 2.19). The constant  $C_1$  incorporates several other constants:

$$C_1 = -4.67 \times 10^{-13} \bar{g} \lambda_0^2. \quad (2.22)$$

Given an observed spectral line sampled at  $N$  wavelength points, we can construct a loss function to describe the difference between the observed Stokes parameter  $V_{obs}$  and a theoretical  $V_{th}$ .  $V_{th}$  is the Stokes  $V$  profile we can construct from the gradient of  $I$ , if we

### 2.3 Measurements and inversions

know the line-of-sight field exactly:

$$\chi^2 = \frac{1}{N} \sum_{i=0}^N \left( \frac{V_{obs,i} - V_{th,i}}{\sigma_i} \right)^2 \quad (2.23)$$

$$= \frac{1}{N} \sum_{i=0}^N \frac{1}{\sigma_i^2} \left( V_{obs,i} - C_1 B_{\parallel} \frac{\partial I_i}{\partial \lambda} \right)^2 \quad (2.24)$$

$$= \frac{1}{N} \sum_{i=0}^N \frac{1}{\sigma_i^2} \left( V_{obs,i}^2 - 2C_1 B_{\parallel} V_{obs,i} \frac{\partial I_i}{\partial \lambda} + C_1^2 B_{\parallel}^2 \left( \frac{\partial I_i}{\partial \lambda} \right)^2 \right). \quad (2.25)$$

We now differentiate  $\chi^2$  with respect to  $B_{\parallel}$ , and change the notation for  $V_{obs,i}$  to just  $V_i$ :

$$\frac{\partial \chi^2}{\partial B_{\parallel}} = \frac{1}{N} \sum_{i=0}^N \frac{1}{\sigma_i^2} \left( -2C_1 V_i \frac{\partial I_i}{\partial \lambda} + 2C_1^2 B_{\parallel} \left( \frac{\partial I_i}{\partial \lambda} \right)^2 \right). \quad (2.26)$$

The errors on each point  $\sigma$  will distribute through all terms and eventually cancel, as will the  $1/N$  factor, so we can drop them from the next step. We set the derivative equal to zero to minimize the  $\chi^2$  function:

$$2C_1^2 B_{\parallel} \sum_i \left( \frac{\partial I_i}{\partial \lambda} \right)^2 = 2C_1 \sum_i V_i \frac{\partial I_i}{\partial \lambda} \quad (2.27)$$

$$B_{\parallel} = \frac{\sum_i V_i \frac{\partial I_i}{\partial \lambda}}{C_1 \sum_i \left( \frac{\partial I_i}{\partial \lambda} \right)^2}. \quad (2.28)$$

Using known values for the Ca II 8542 Å transition, we can obtain an estimate for the line-of-sight magnetic field strength using only the Stokes  $I$  and  $V$  data and equation 2.28.

# 3

---

## The effect of a solar flare on chromospheric oscillations

In this chapter, we present a study of oscillatory signals in an active region which experienced an M1.1 solar flare on 6<sup>th</sup> September 2014. The results of this chapter were published in [Millar et al. \(2021\)](#). We studied the effect of flare activity on the oscillatory signals present in the active region AR12157 above a large sunspot, focusing particularly on the umbra/penumbra and flare ribbons, with imaging spectroscopy data from the CRISP instrument at the Swedish Solar Telescope. We aimed to identify oscillatory signals present both before and after the onset of the flare, to observe if the flare activity had induced oscillatory behaviour, or affected the signals which were present beforehand. The study was carried out on the H $\alpha$  and Ca II 8542 Å spectral lines, the 1600 Å and 1700 Å UV channels of SDO/AIA, and we used HMI vectorgrams and 171 Å SDO/AIA images in our interpretations of the results.

In Section 3.1 we overview the flare, describe the datasets used and the initial processing steps; in Section 3.2 we outline the methods used to identify oscillatory signals in the data; Section 3.3 outlines the main results from our analysis; we discuss limitations to our methods and investigate possible interpretations of the results in Section 3.4 before concluding in Section 3.5.

### 3.1 Event and datasets

The M1.1 flare SOL2014-09-06T17:09 occurred in active region AR 12157 ( $-732''$ ,  $-302''$ ). The analysis presented below is based on data from the CRISP instrument at the Swedish Solar Telescope, and the Atmospheric Imaging Assembly (AIA) on the Solar Dynamics

### 3.1 Event and datasets

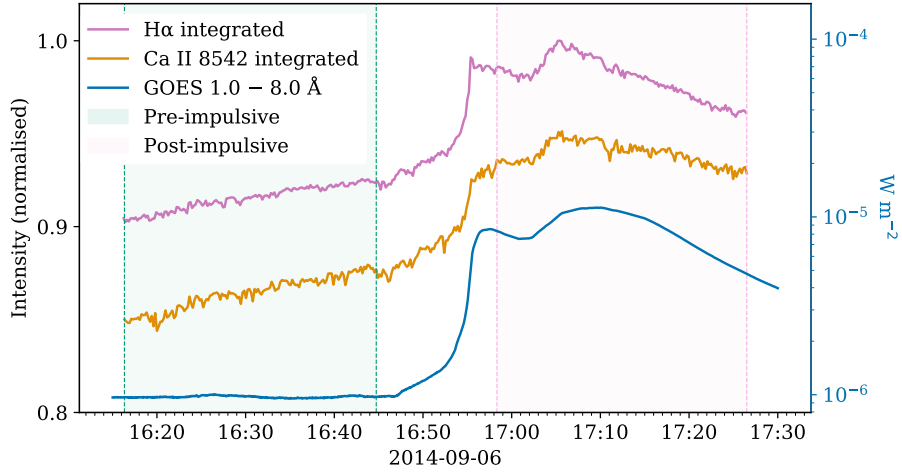


**Figure 3.1:** Lightcurves of GOES 1–8 Å and the H $\alpha$  and Ca II 8542 Å spectral lines from CRISP integrated across the field of view. The shaded areas bound by dashed lines indicate the two  $\sim$ 30 minute periods which were analysed separately: “pre-impulsive” (green) and “post-impulsive” (pink).

Observatory (SDO). The flare timeline is shown in Figure 3.1 with lightcurves from GOES 1–8 Å and from the CRISP lines, integrated over the field of view. Context images of the region during the flare activity from CRISP and SDO are shown in Figure 3.2, and these image coordinates (in terms of Solar X/Solar Y in arcseconds) are used in the figures throughout this chapter. The coordinates of the active region change as it moves across the disk due to solar rotation, but subsequent figures will be remapped so that they share spatial axes with those in Figure 3.2.

Individual pixels in the CRISP data show an extremely rapid increase in brightness during the flare onset at approximately 16:56. The rapid rise shown in the CRISP lightcurves in Figure 3.1 exemplify this, as the flare brightenings only affected a small portion of all the pixels (lower right panel of Figure 3.2). The AIA channels contain many saturated pixels at the impulsive phase, with much blooming and signal bleeding into neighbouring pixels, two effects which are detrimental to the analysis of oscillatory signals. Bursty lightcurves are unfavourable for the purposes of searching for periodicities (Section 2.2.2) and so we avoided the impulsive phase entirely. We selected two  $\sim$ 30 minute intervals to analyse, before the flare onset (16:15–16:45, “pre-impulsive”) and after the initial brightening (16:57–17:27, “post-impulsive”). Ideally the intervals would be much longer, so that the shape of the power spectra at longer periods could be better constrained. Unfortunately the observation ended at 17:27, and we required both intervals to be of equal lengths for proper comparison.

### 3.1 Event and datasets

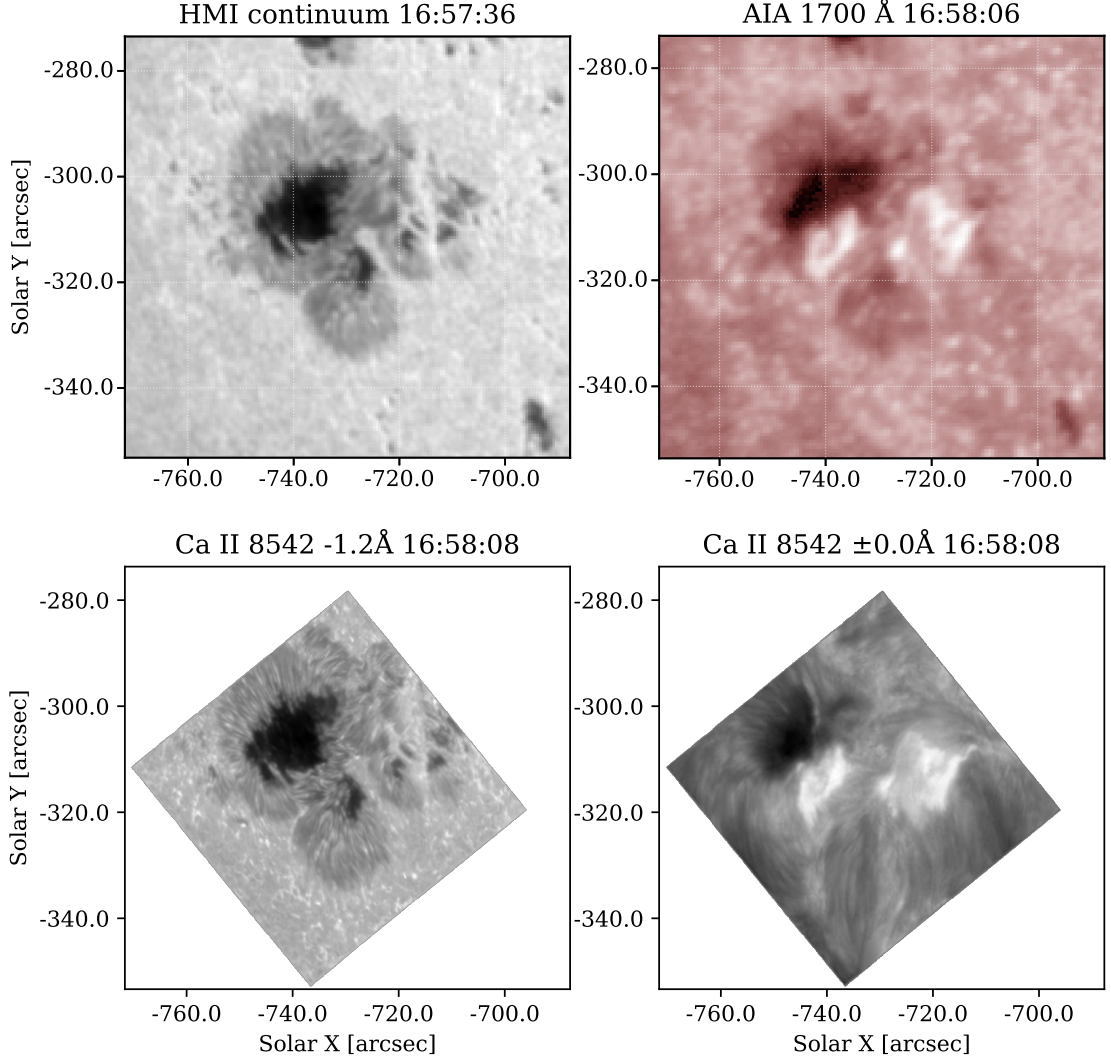


**Figure 3.2:** The area observed by CRISP at a time just after the flare onset, in several wavelengths from CRISP and SDO. The line wing (lower-left) displays the photosphere, similar to the HMI/SDO continuum image (upper-left), while the line core (lower-right) shows the chromosphere and can be compared to the AIA/SDO 1700 Å image (upper-right).

### 3.1 Event and datasets

#### 3.1.1 CRISP

The active region was observed by the CRISP instrument at the SST between approximately 15:30 and 17:30 in H $\alpha$  and Ca II 8542 Å, sampling the chromosphere and upper photosphere at 0.057" per pixel. The spectral dimension in H $\alpha$  covers  $\pm 1.4$  Å with a step size of 0.2 Å and Ca II 8542 Å covers  $\pm 1.2$  Å with step size 0.1 Å. Full spectral scans were obtained with a cadence  $\Delta t = 11.6$  s. The dataset is available on the F-CHROMA flare database<sup>1</sup>. The power spectra obtained in each time interval span periods from 24 s to 30 min, making them suitable for studying  $\sim$ 3-minute oscillations.

The CRISP images are aligned such that solar North points upwards along the y-axis, and the field of view rotates and moves, keeping features of interest fixed at the same pixels throughout the observation. For each 30 min analysis window (pre- and post-impulsive), only pixels which were in the field of view for the whole window were analysed. This accounts for the odd shape of the analysed field which will be seen in future figures.

The images were originally of dimension (1398, 1473), but were re-binned by a factor of 10 to be dimension (139, 147), after clipping the edges of the images. Timeseries for analysis were drawn from each 10x10 "macropixel". This was done to reduce the effects of seeing, and to reduce the required computation time.

#### 3.1.2 AIA

SDO/AIA samples various heights in the solar atmosphere at a resolution of 0.6" per pixel. When accounting for the re-binning of CRISP data, the spatial scales are approximately equal. For this analysis we used the 1600 Å and 1700 Å UV channels, which sample the lower atmosphere. The other AIA channels were not used, as they were greatly affected by the brightness increase caused by the flare activity, with the saturation and blooming effects continuing after the flare peak into the post-impulsive interval, mostly in bright loop structures.

AIA images for the chosen channels were obtained and prepped using the SunPy package (Mumford et al. 2020), before cutting out an area of interest slightly larger than the CRISP field of view with the `submap` method. Solar rotation was accounted for using `mapsequence_solar_derotate` from `sunpy.physics.solar_rotation`, which uses the differential rotation parameters from Howard et al. (1990). The larger field of view used for the

---

<sup>1</sup><https://star.pst.qub.ac.uk/wiki/public/solarflares/0450.html>

### 3.2 Methods

AIA analysis allowed us to sample more of the surrounding area, outside the active region. The cadence of the UV channels is approximately double that of the CRISP observations at 24 s, nevertheless this sampling is sufficient for our purposes.

## 3.2 Methods

From the re-binned CRISP images, intensity timeseries were drawn from each spectral line position over the pre-impulsive and post-impulsive time intervals. The 1600 Å and 1700 Å data were drawn from approximately the same time interval. Each timeseries was then analysed using the spectral fitting method described in Section 2.2.6. Of the three spectrum models; red-noise background (M1), red-noise plus Gaussian bump (M2), and red-noise plus kappa function (M3), a preferred model was determined by following the process summarised in Figure 2.8, using a significance level of 99.9% (i.e.  $p$ -values of 0.001). Examples of each of the three model fits are shown in Figure 3.3.

A 99.9% confidence level may seem rather stringent, however reducing the confidence level will introduce false positives; we believe that avoiding this is important. When we performed the same analysis using a 95% level it (unsurprisingly) returned more M2 results, but the overall occurrence patterns and changes were the same as those obtained using the 99.9% confidence level. On inspection of individual power spectra and their fits, many M3-like spectra, with a kappa function appearance, had been incorrectly assigned as M2 at the 95% confidence level. Since the main results of the analysis remained the same, the 99.9% level was determined to be more appropriate in this case.

## 3.3 Results

### 3.3.1 Preferred models

From the spectral fitting method, we obtained a preferred model for each macropixel in the pre-impulsive and post-impulsive intervals. The results are visualised in Figures 3.4–3.7, which display the areas showing oscillatory signals at various wavelength points, along with contours showing the outlines of the sunspot umbrae and penumbrae, and coloured patches showing the positions of the flare ribbons, for reference. It should be noted that the ribbons were not present at the time of the pre-impulsive interval. For the sake of brevity, only every second wavelength point is displayed in these figures.

### 3.3 Results

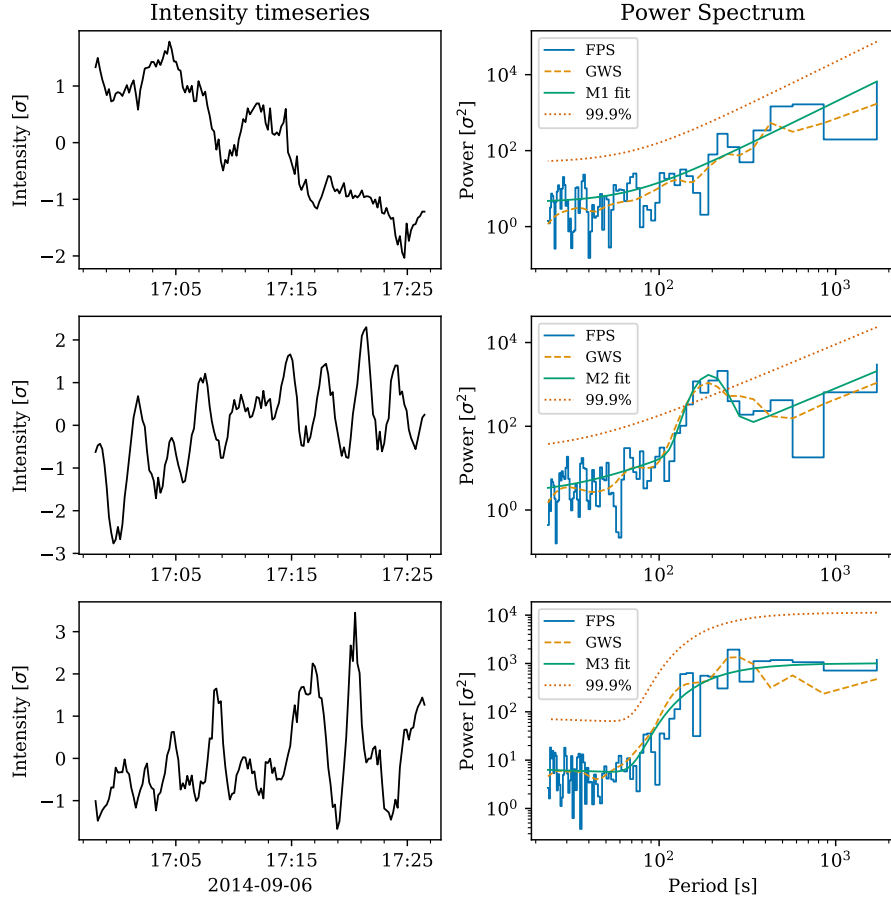


**Figure 3.3:** Timeseries (left column) and their respective Fourier power spectra (right column) drawn from the CRISP dataset, showing examples of each of the three available models. The right-hand panels contain the FPS (blue stepped line), the global wavelet spectrum (yellow dashed line), the mean spectrum fit (green line), and the 99.9% significance level (orange dotted line). Top row: Ca II 8542 Å core timeseries from quiet Sun, which was classified as fitting M1 (red-noise background). Middle row: Ca II 8542 Å core timeseries from the sunspot umbra, fit with M2 (Gaussian bump). Bottom row: H $\alpha$  core timeseries from the sunspot penumbra, classified as M3 (kappa function). This figure is a combination of Figures 2.5–2.7.

### 3.3 Results

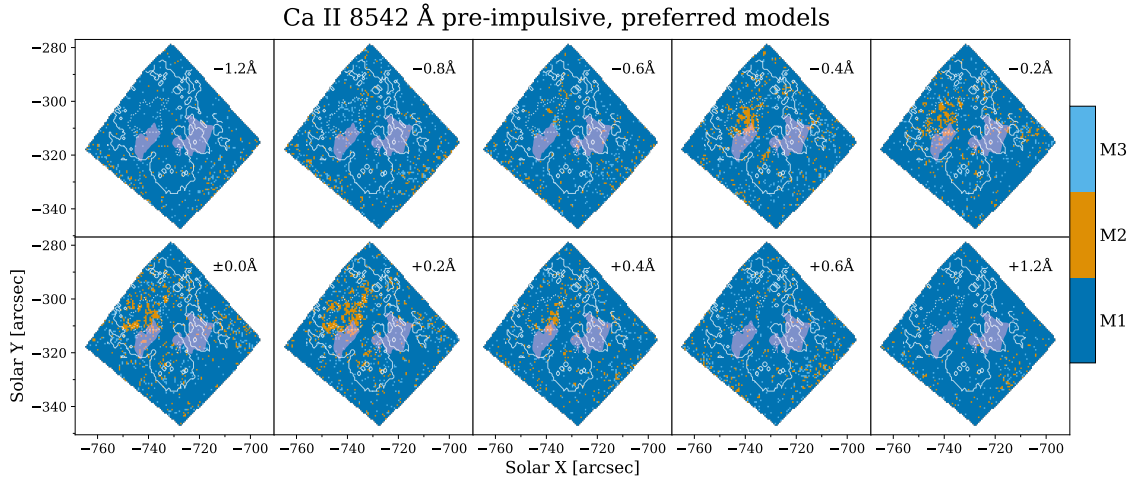


**Figure 3.4:** The models which best describe the spectra of individual macropixels at several points across the Ca II 8542Å line, during the pre-flare period (16:15-16:45). Each model is assigned a different colour, and the edges of the sunspot umbra and penumbra (drawn from 40% and 75% intensity levels of the first wing image) are shown in dotted and solid contours, respectively. The locations of the flare footpoints are indicated by the semi-transparent solid patches, showing pixels over 55% of the maximum intensity of a line core image from the post-impulsive period.

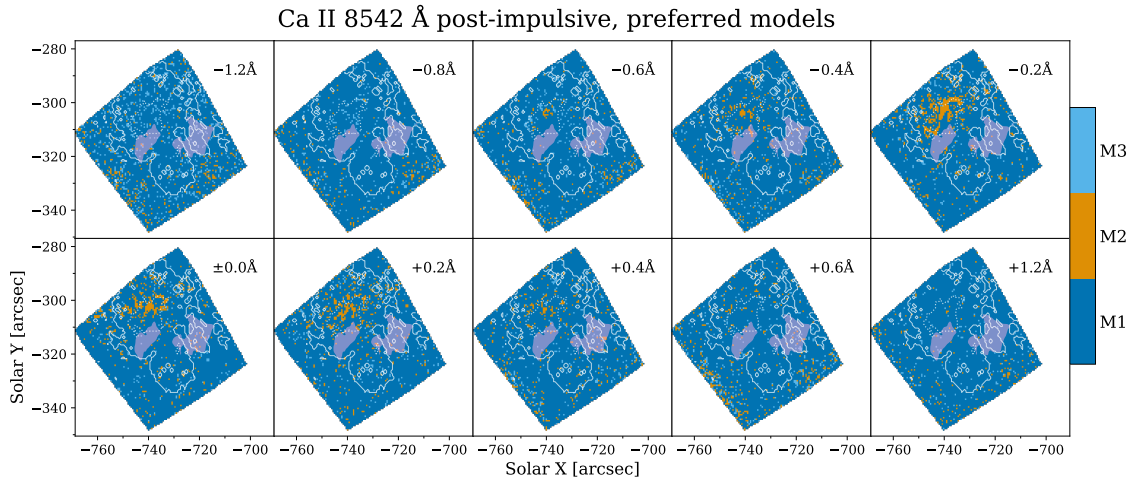


**Figure 3.5:** Similar to Figure 3.4 but during the post-impulsive period (16:57-17:27). The shape of the plots is different than in the pre-flare case because of the rotation of the CRISP field of view. Note the northern umbra/penumbra border with concentrations of M2 fits at several wavelengths.

### 3.3 Results

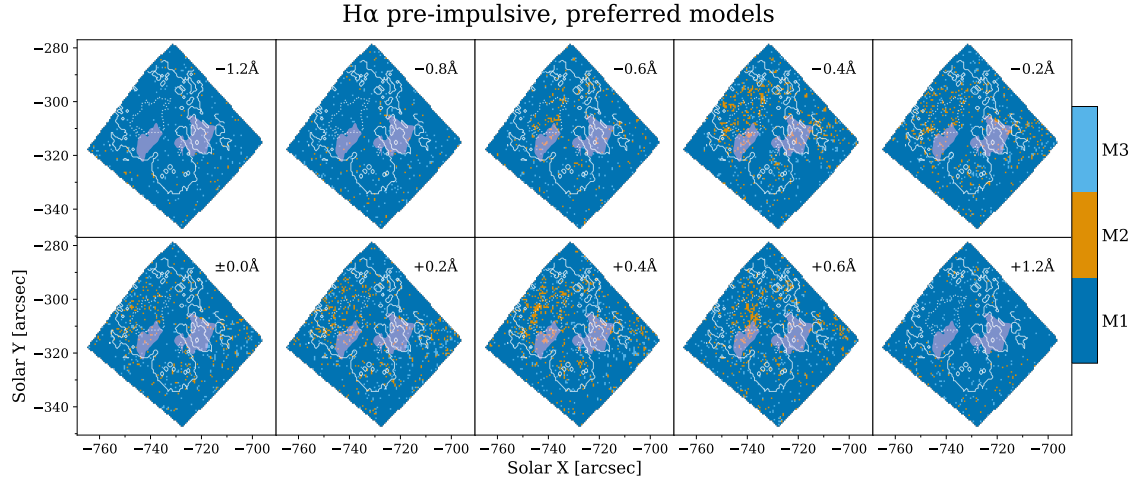


**Figure 3.6:** Similar to Figure 3.4 but for the H $\alpha$  line.

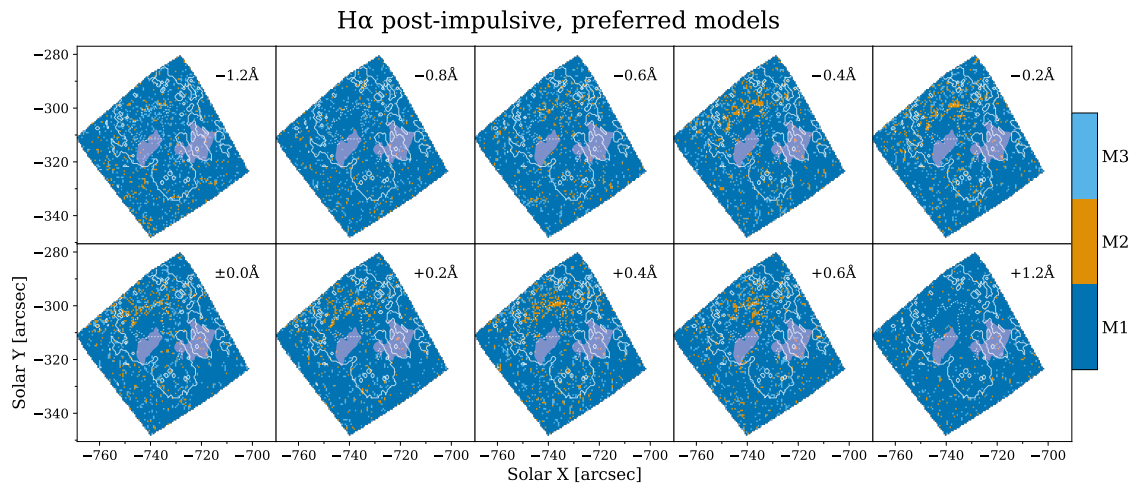


**Figure 3.7:** Similar to Figure 3.4 but for H $\alpha$  after the initial flare activity.

### 3.3 Results

The first thing to note from these plots is that M1, the power-law coloured-noise model, was the most common result, being the preferred result in 83% of all pixels, compared with 6% for M2 which includes the Gaussian bump, and 11% for the M3 kappa function. This is unsurprising as M1 is the simplest and therefore most generally applicable shape of the three. Table 3.1 shows the percentage of M2 and M3 fits which were assigned to macropixels in select wavelengths and in both the pre-impulsive and post-impulsive time intervals.

Broadly, it appears that more M2 fits are found for power spectra at wavelengths closer to the centres of the lines, out to  $\pm 0.4 \text{ \AA}$ , and areas with many M2 fits are found over the largest sunspot umbra, and around its border. As we move in wavelength away from the line core towards the wings, the occurrence of M2 fits drops considerably. Many more pixels in the wings show fits to M3, especially in the post-impulsive data for both lines.

Although there appears to be correlation between the positions of M2 fits and the sunspot umbra, there is not much distinction between the penumbra of the sunspot and the surrounding area.

The locations of the oscillatory signals compared to the flare ribbons are another important aspect to the results. These locations are superimposed on both the pre- and post-impulsive results (Figures 3.4–3.7), for easy reference between figures. There appears to be little to no oscillatory behaviour at the locations of the flare ribbons in the post-impulsive results, with most of the M2 fits located near the northern umbra-penumbra border of the largest sunspot. There were however some signals of oscillations at the location of the eastern ribbon in the pre-impulsive data, which may indicate the effect of the flare on the oscillations. This is discussed in more detail in section 3.4.2.

#### Ca II 8542 Å preferred models

Before the flare onset in the Ca II 8542 Å line, M2 fits are found concentrated over the large sunspot umbra at the line core, with the results at  $\pm 0.2 \text{ \AA}$  appearing similar (Figure 3.4). Moving away from the core, at the  $\pm 0.4 \text{ \AA}$  positions there are some M2 fits over the umbra but these are much more concentrated spatially. Further from the core, M2 fits are very scarce, with the majority of the pixels being described best by the standard coloured-noise background (M1).

After the impulsive phase of the flare, the appearance of the 8542 Å results is quite different (Figure 3.5). There is an increased number of M3 fits, in particular in the line wings,

### 3.3 Results

**Table 3.1:** Percentage of all macropixels which had preferred model fits M2 (Gaussian bump) and M3 (kappa function) for each wavelength and for the pre-impulsive and post-impulsive intervals.

Wavelength	Pre M2	Pre M3	Post M2	Post M3
8542 – 1.2Å	1.9%	2.9%	3.9%	9.5%
8542 – 0.8Å	3.1%	4.8%	2.5%	4.0%
8542 – 0.6Å	2.7%	3.9%	3.2%	4.6%
8542 – 0.4Å	5.7%	4.9%	4.2%	4.0%
8542 – 0.2Å	5.7%	3.8%	7.1%	3.3%
8542 ± 0.0Å	7.1%	4.7%	5.6%	2.7%
8542 + 0.2Å	7.8%	4.1%	5.7%	3.1%
8542 + 0.4Å	4.1%	3.6%	4.2%	3.8%
8542 + 0.6Å	3.2%	4.4%	4.4%	4.6%
8542 + 1.2Å	1.6%	1.9%	2.2%	2.5%
H $\alpha$ – 1.2Å	0.7%	1.7%	3.2%	8.1%
H $\alpha$ – 0.8Å	0.9%	2.5%	2.2%	5.9%
H $\alpha$ – 0.6Å	2.7%	2.3%	3.6%	6.5%
H $\alpha$ – 0.4Å	5.9%	3.6%	5.1%	6.7%
H $\alpha$ – 0.2Å	4.6%	3.8%	4.8%	7.7%
H $\alpha$ ± 0.0Å	3.4%	3.3%	4.4%	6.6%
H $\alpha$ + 0.2Å	4.9%	4.3%	3.8%	5.6%
H $\alpha$ + 0.4Å	6.3%	4.0%	5.6%	6.8%
H $\alpha$ + 0.6Å	5.3%	4.2%	4.5%	7.3%
H $\alpha$ + 1.2Å	1.0%	2.8%	1.5%	3.2%

### 3.3 Results

and a decreased number of M2 fits in general. The  $-0.2\text{ \AA}$  position seems to show an enhancement of M2 fits over the umbra, while at the line core and at the  $+0.2\text{ \AA}$  position the number of M2 fits has dropped, and there is a change in the location of the oscillatory signals: the positions where M2 fits occur is in fact quite different from the pre-impulsive case. The places showing M2 fits in the line core and  $+0.2\text{ \AA}$  positions during the post-impulsive interval are now mostly at the northern umbra/penumbra border, rather than more towards the centre of the largest sunspot (compare with Figure 3.4).

#### H $\alpha$ preferred models

The results for H $\alpha$  are in some ways very similar to the Ca II 8542  $\text{\AA}$  case. For example, there are more M3 fits towards the far wings and in the post-impulsive data. However, unlike Ca II 8542  $\text{\AA}$  the M2 model fits are most prevalent in the  $+0.4\text{ \AA}$  and  $+0.6\text{ \AA}$  line positions, as opposed to the line core. Additionally, the area where M2 was the preferred fit is far smaller in both the pre-impulsive and post-impulsive cases than their counterparts in Ca II 8542  $\text{\AA}$ . Unlike for Ca II 8542  $\text{\AA}$ , there seems to be very little evidence of concentrated oscillatory signals before the flare occurs, even at the centre of the sunspot, except in the  $+0.4\text{ \AA}$  and  $+0.6\text{ \AA}$  panels of Figure 3.6.

After the impulsive phase, H $\alpha$  shows a large number of M3 fits which are not only confined to the wings of the line. Unlike the Ca II 8542  $\text{\AA}$  line, in many wavelength positions it appears that after the impulsive phase there has been an increase in the number of macropixels showing oscillatory signals, and we see lots of M2 fits occurring from the core out to  $\pm 0.6\text{ \AA}$ . While the total area of M2 fits is fairly sparse compared to Ca II 8542  $\text{\AA}$ , there is a considerable amount of oscillatory signal focused on the northern umbra/penumbra border where there was a lot less in the pre-impulsive results.

##### 3.3.2 Periods and locations of Gaussian bump peaks

In pixels where M2 was the preferred fit, we can use the periods at which the Gaussian bumps M2 fits peak to diagnose the characteristics of the oscillatory signals coming from those pixels. These results are shown in Figures 3.8–3.11 for the Ca II 8542  $\text{\AA}$  and H $\alpha$  lines, in both the pre-impulsive and post-impulsive time intervals. Only wavelength values near the line core are presented, and the field of view has been cropped to focus on the largest sunspot, where the majority of the oscillatory signals were detected.

### 3.3 Results

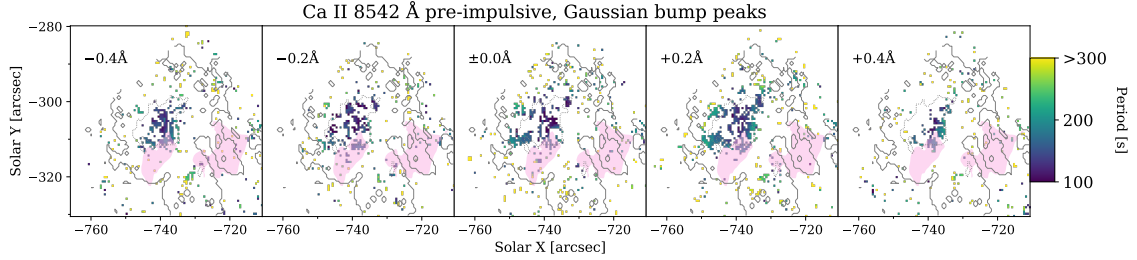


**Figure 3.8:** This plot is similar in layout to Figure 3.4 but it shows periods at the peaks of Gaussian bumps, in macropixels where M2 was the preferred fit. Those macropixels which were not best fitted by M2 are left blank. This shows the difference in the period of oscillatory signals which are seen at different spatial positions across the images. In general, the period of the oscillations is shorter towards the centre of the sunspot. The contours showing the umbra and penumbra are identical to figures 3.4–3.7, and the footpoints are shown similarly.

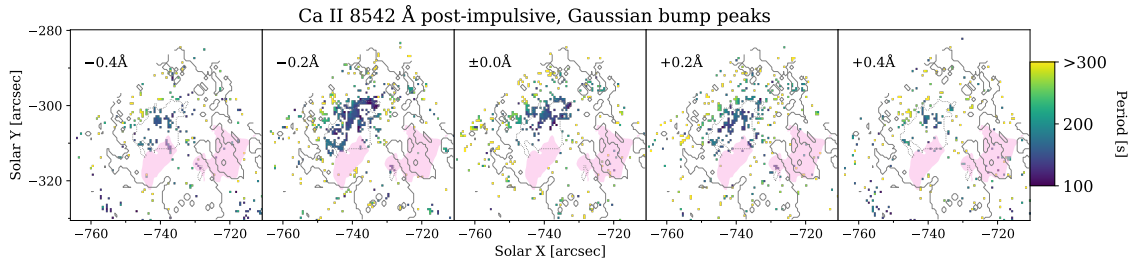


**Figure 3.9:** Similar to Figure 3.8 but for the post-impulsive period.

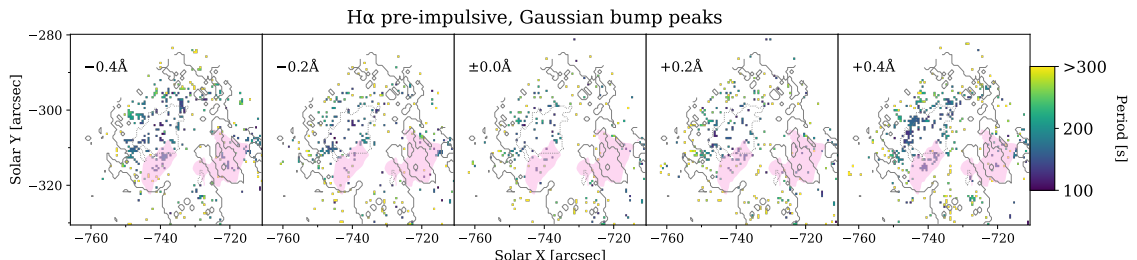


**Figure 3.10:** Similar to Figure 3.8 but for the H $\alpha$  line.

### 3.3 Results

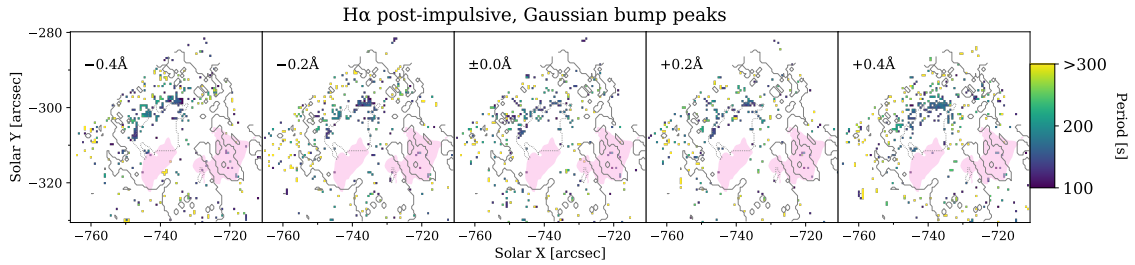


**Figure 3.11:** Similar to Figure 3.8 but for H $\alpha$  in the post-impulsive period.

From these plots we see a difference in the periods of the bump peaks when moving from the centre of the sunspot outwards. In general the periods of the oscillatory signals are shorter in the centre of the sunspot, at 100–150 s, and gradually increase into the 200–250 s range towards the edges of the umbra. In the penumbra the periods reach 300s and above. This is most clearly seen in the Ca II 8542 Å data due to the larger area of M2 fits, but the effect is present in the results from both lines. These results could be interpreted similarly to those of Reznikova et al. (2012) and Jess et al. (2013), as evidence of a changing magnetic field inclination from the centre of the sunspot outwards.

There are some differences between pre-impulsive and post-impulsive results, with periods in post-impulsive data tending to be longer than in the pre-impulsive case. Again this is clearer to see in Ca II 8542 Å results (compare the  $\pm 0.2 \text{ \AA}$  and line core panels of Figures 3.8 and 3.9), due to the larger area of M2 pixels in this line, compared to H $\alpha$ . Again, this could be caused by a differing magnetic field inclination. However, in this case the difference between pre-impulsive and post-impulsive period distributions could suggest that the magnetic field through the sunspot chromosphere has been affected by the flare itself, perhaps because of the reconfiguration of magnetic field taking place during the flare.

#### 3.3.3 AIA Results

The preferred models found for pixels from AIA 1600 Å and 1700 Å are shown in Figure 3.12, containing both pre-impulsive and post-impulsive results. These plots are in contrast to those in Figures 3.4–3.7 in that there is little convincing evidence whatsoever of concentrated oscillatory signals above the large sunspot, or in the surrounding active region. Instead, there is an abundance of M2 fits seen outside the active region, around the edges

### 3.4 Discussion

**Table 3.2:** The percentage of all pixels in AIA wavelengths which had preferred fits M2 and M3, for the pre- and post-impulsive time intervals.

Wavelength	Pre M2	Pre M3	Post M2	Post M3
AIA 1600 Å	9.2%	4.9%	8.6%	5.7%
AIA 1700 Å	15.8%	4.4%	15.9%	5.1%

of the plots. These match spatially with the intensity of the ultraviolet channels: immediately surrounding the sunspot umbra and penumbra is a large region of brighter plage as seen in Figure 3.2, where scarce oscillatory signals are seen.

Table 3.2 shows the percentage of M2 and M3 fits for the two AIA channels. This table and also Figure 3.12 show that the 1700 Å channel contains far more pixels with oscillatory signals than the 1600 Å filter. There is also little change in the number of M2 fits between the pre-flare and post-impulsive periods in either channel.

The most noticeable change between the pre- and post-impulsive results is the appearance in post-impulsive data of many locations best fitted by M3, at locations near the flare ribbons. As discussed in Section 2.2.6, a successful fit to M3 does not directly tell us anything about oscillatory behaviour, however we can say that these timeseries must have deviated significantly from the coloured-noise background, which is perhaps to be expected due to the large variations in brightness in these pixels caused by the flare.

## 3.4 Discussion

### 3.4.1 Limitations

In this study, we have analysed intensity variations at specific wavelengths, however there are several physical effects which can contribute to the fluctuations in brightness at a particular wavelength, including Doppler shifts of the core of the line. Other approaches to the detection of oscillations utilise such velocity signals, particularly in the photosphere where intensity variations are hard to detect (Khomenko & Collados 2015). While using the evolution of the line profiles to infer velocity oscillations in our observations would allow a more in-depth understanding of the physical reasons for the oscillations, in terms of what we focus on here — the locations of the oscillations and their changes — we expect that this would return similar results to our investigation based on intensity. In fact, upon inspection of the evolution of spectral line shapes in this data, while macropixels with

### 3.4 Discussion

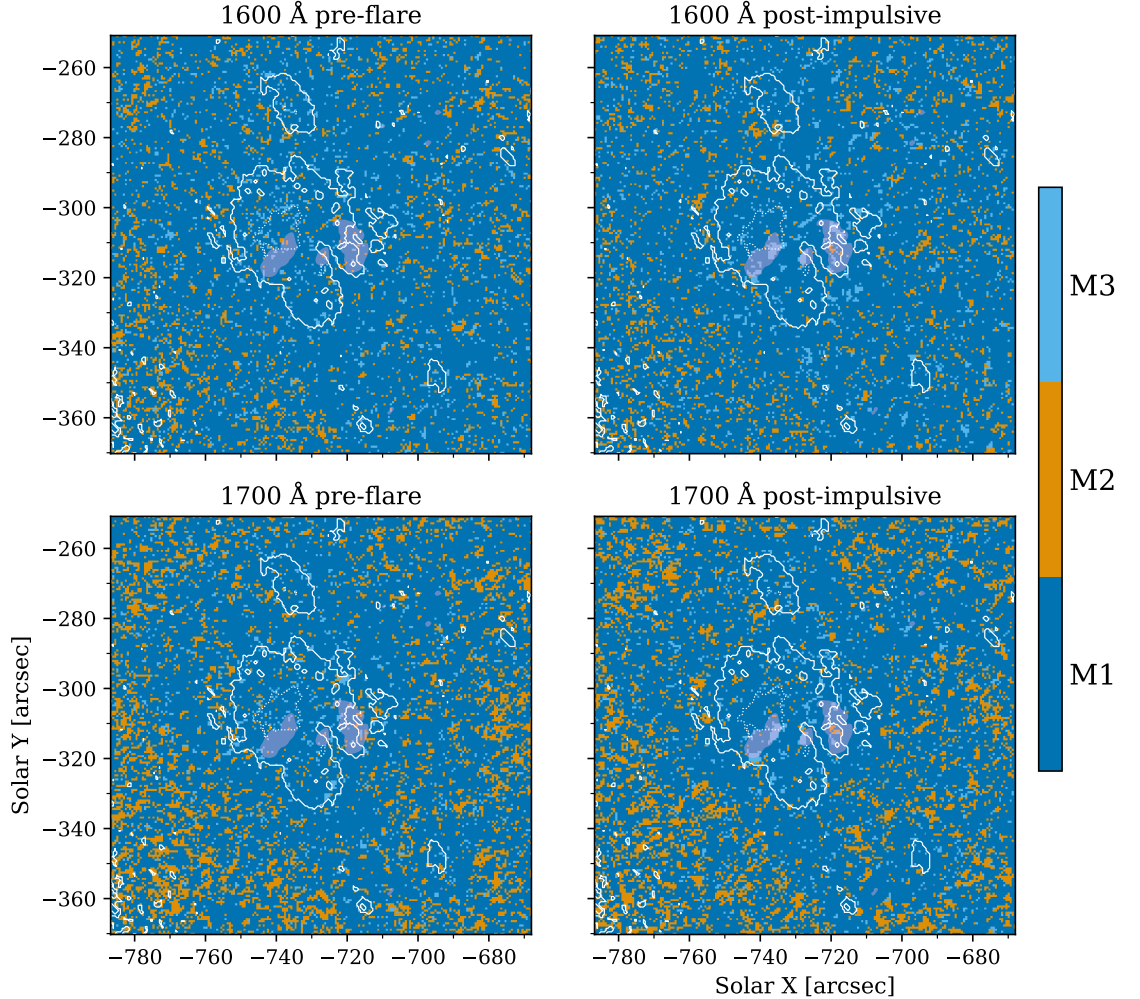


**Figure 3.12:** Similar to the corresponding plots for CRISP wavelengths (Figures 3.4-3.7) but for the two AIA channels, with pre- and post-impulsive displayed on the left and right, respectively. Note the field of view is slightly larger than in the CRISP figures. Overplotted are contours of 30% and 73% intensity from the first HMI continuum image to show the positions of the sunspot umbra and penumbra. Filled contours at over 15% of the maximum intensity in 1700 Å at the beginning of the post-impulsive period show the locations of the flare footpoints.

### 3.4 Discussion

strong velocity signals also produced an oscillatory behaviour in intensity at a particular wavelength, as would be expected, we also found that intensity oscillations were not always accompanied by clear changes in the spectral line shape. Such cases could have been missed by an analysis relying on Doppler line shifts alone. In this respect our approach is just as valid as one based on spectral line profiles, while being simpler to carry out. Nevertheless, care should be taken when drawing conclusions from these results, and there is certainly more to be learned from the full line profiles.

While the spectral fitting method used here is a powerful technique and has been proven useful in many previous studies, there are limitations to its effectiveness. One of the first things to consider is our choice of models. The results of this methodology are dictated by the models, as the data are forced to fit one of three models we choose. For example, if some process exists which produces two separate periods in the same timeseries, the resulting Fourier spectrum could contain two bumps. This could either result in the selection of one of these two bumps and not the other, or it could fail to fit the Gaussian bump model altogether. The case of double periods has been known to happen in QPP data ([Inglis et al. 2015](#)), and could be better handled by, for example, wavelet analysis. However wavelet analysis is difficult to automate for large datasets like the one studied here.

One of the main reasons the kappa-shaped model was fitted in addition to the coloured-noise background and Gaussian bump models was due to the initial choice of models being insufficient. On inspection of M2 fit results by eye, some spectra were selected as an M2 fit when they had flattened off in the long-period regime, instead of returning to the red-noise background level. These poor results at the low frequency part of the Fourier power spectra could have been because the fitting technique is biased towards the high frequency end, due to the nature of the frequency space covered by the Fourier transform. When transformed into periods, there are more datapoints at the low period end, leading to a greater influence on the goodness of fit.

The CRISP observation for this dataset finished at approximately 17:30, putting limits on the length of the post-impulsive timeseries we could analyse. The length of the timeseries relates to the lowest frequency which can be studied using the Fourier transform. Longer timeseries would also reduce noise in the spectra we obtain, and hence lead to better (or at least, faster converging) fits.

### 3.4 Discussion

#### 3.4.2 Interpretations

The CRISP results showed considerable variation across the wavelength steps of the spectral lines. This could be because different points in the lines have sampled different heights in the atmosphere: both H $\alpha$  and Ca II 8542 Å sample the mid-chromosphere at their cores ( $\sim$ 1Mm, [Kuridze et al. 2015](#)) and the photosphere at their wings. Strong, isolated oscillatory signals could be present only above a certain height, beyond the altitude at which long period signals from the photosphere have decayed.

Another effect which applies here is that radiation at a particular wavelength does not always originate from exactly the same altitude, as its contribution function can be spread out. If there are local pressure disturbances in the atmosphere caused by MAG waves, then sampling from a wide range of heights would lead to muddied signals, with the potential for destructive interference occurring. MAG waves could be travelling through the lower parts of the sunspot chromosphere, but not be detectable in this kind of observation because of the broad contribution function. Conversely, if we receive light which is emitted from a more vertically compact atmospheric slab, it is more likely that signals will be preserved.

The results in H $\alpha$  and Ca II 8542 Å look very different, which raises questions as these lines are often considered to sample similar heights in the chromosphere. We do not know the exact heights at which the emergent radiation of these lines are formed, but we can look to examples from authors who have used e.g. RADYN to simulate their contribution functions, such as [Kuridze et al. \(2015\)](#) who used this method to synthesise the line formation for the same CRISP flare dataset as we use here, although their study was for flaring pixels. The formation height of Ca II 8542 Å was found to be lower in the atmosphere than H $\alpha$ . As another example, [Costa et al. \(2015\)](#) simulated H $\alpha$  and Ca II 8542 Å lines from an M3.0 flare at both very early times (similar to pre-flare) and late times, finding no overlap in height of the contribution functions at the line cores, with H $\alpha$  core emerging from 1.6–2.2 Mm and Ca II 8542 Å emerging from 1.3–1.5 Mm. If the spectral lines behaved similarly in our case, this could account for the discrepancies between the lines, and also the lack of strong signals in H $\alpha$ , as the contribution function at the core is far more spread out than its Ca II 8542 Å counterpart.

Similar effects could also explain the results from the AIA UV channels in Section 3.3.3. These channels are very broad filters and the heights which they sample are perhaps not precise enough to detect localised oscillations in the active region by this method. The results for the AIA 1600 Å and 1700 Å channels showed a lack of oscillatory signatures

### 3.4 Discussion

over the umbra, and more in the penumbra and plage. These results are similar to those obtained by Battams et al. (2019) who used a power spectrum fitting analysis and found spectral bumps across almost the whole disk in the 1700Å AIA channel, except in the area immediately surrounding a sunspot. The difference between the active region and “quiet” Sun results could be due to a difference in the spectral distribution of the radiation transmitted by the filters. Observations of reduced wave power over sunspots compared to quiet Sun have been noted by many previous authors. Several theories exist to explain the phenomenon including absorption and scattering of MAG waves after conversion from p-modes (Braun et al. 1987, Cally et al. 2003, Rijs et al. 2016), less wave excitation due to a reduction of underlying convection (Goldreich & Kumar 1988), and reductions of attenuation lengths in highly magnetic regions (Jain et al. 1996, Hindman et al. 1997).

A study by Simões et al. (2019) showed how the temperatures sampled by these filters can be different in flare and plage data, with flare data sampling the chromosphere and plage data sampling the photosphere, generally. It is possible that in active regions the UV filters sample heights more similar to the flare data studied by Simões et al. (2019), perhaps from higher in the atmosphere with a smaller oscillatory component. A similar phenomenon named “height inversion” has been observed by other authors, where 3-minute signals are seen to be strong in chromospheric sunspot umbrae, but almost non-existent in the photosphere which is dominated by 5-minute oscillations (Kobanov et al. 2008, 2011).

Milligan et al. (2017) found flare-related oscillatory signatures in 1600Å and 1700Å data, which they attributed to flare induced chromospheric signals. These were signatures integrated over a large field-of-view, and the flare-related oscillatory signals were during the impulsive phase which we did not study due to the saturation effects. Farris & McAteer (2020) conducted a spatially resolved study of flare-induced 3-minute signals in AIA UV channels and found increases to their power at some locations. However, this was using a very different analysis based on power maps, so comparing our results to theirs is tricky (Section 2.2.2).

The positions where significant oscillatory bumps were identified in CRISP data appear to have changed after the flare activity. Comparing the bottom right panel of Figure 3.2 to the results in Figures 3.4–3.11, we see that one of the flare ribbons develops over the lower corner of the sunspot umbra. This could explain the lack of M2 fits in this area in the post-impulsive results. The number of macropixels with M2 fits increased at the northern boundary of the umbra in most wavelengths at  $\pm 0.4$  Å, and it is possible the same would have happened at the southern boundary but the natural oscillations, which

### 3.4 Discussion

are connected to the temperature of the plasma, may have been dramatically affected by flare heating.

If we assume the oscillatory signals we detect here are caused by MAG waves travelling from below, along the sunspot field (Section 1.3.3), the results from Sections 3.3.1 and 3.3.2 may be linked to properties of the magnetic field in the chromosphere above this sunspot. For instance, the areas of the field of view which produced a lot of concentrated M2 fits are different in much of the pre- and post-impulsive results. This could be caused by the magnetic fields having a different orientation after the flare process, causing the MAG waves travelling along the field lines to be guided to a different spatial location. As a speculative example, if we consider the chromosphere to be 2000 km thick, and observe the locations of signals to move by  $\sim 5$  arcseconds, this would correspond to a magnetic field line which was originally normal to the solar surface inclining by  $\sim 60$  degrees. Strong, flare-related changes in field inclination have previously been inferred from line-of-sight magnetograms (Sudol & Harvey 2005) or observed in vector magnetograms (Petrie 2019). The locations of signal changes, over the large sunspot umbra, do not exhibit brightenings which could lead to a change in opacity.

Further evidence for the changing magnetic field interpretation can be seen in the results of Section 3.3.2 where the periods at which Gaussian bumps peak changed after the flare event. In MAG waves the acoustic cut-off frequency determines the period of the oscillations. As discussed in Section 1.3.3, the inclination of the field  $i$  introduces a cosine factor:

$$\omega_c = \frac{\gamma g \cos i}{2c_s} \propto \frac{g \cos i}{\sqrt{T}}. \quad (3.29)$$

Following this equation, the fact that  $g$  has negligible variation, and observing that temperature change is unlikely to be a factor as the areas of M2 fits were far removed from the flare ribbons and do not show any intensity variations, the inclination angle is the only factor which could cause the change in cut-off frequency in this case. Following our example from above of a 60 degree inclination change, the cut-off frequency would be halved, and the prominent period would be doubled.

To test the theory of a changed magnetic field leading to a change in the oscillatory behaviour around the sunspot, we studied data from the HMI instrument on SDO, described in Section 2.1.3. To avoid the effects of solar rotation and line-of-sight changes, we accessed `hmi.sharp_cea_720s` dataseries from 15:00 to 19:00. This series is a reprojection of the magnetic field into three cylindrical equal area (CEA) components:  $B_r$ ,  $B_\phi$ , and  $B_\theta$ , and is available at a cadence of 12-minutes (Hoeksema et al. 2014). We looked for evidence

### 3.4 Discussion

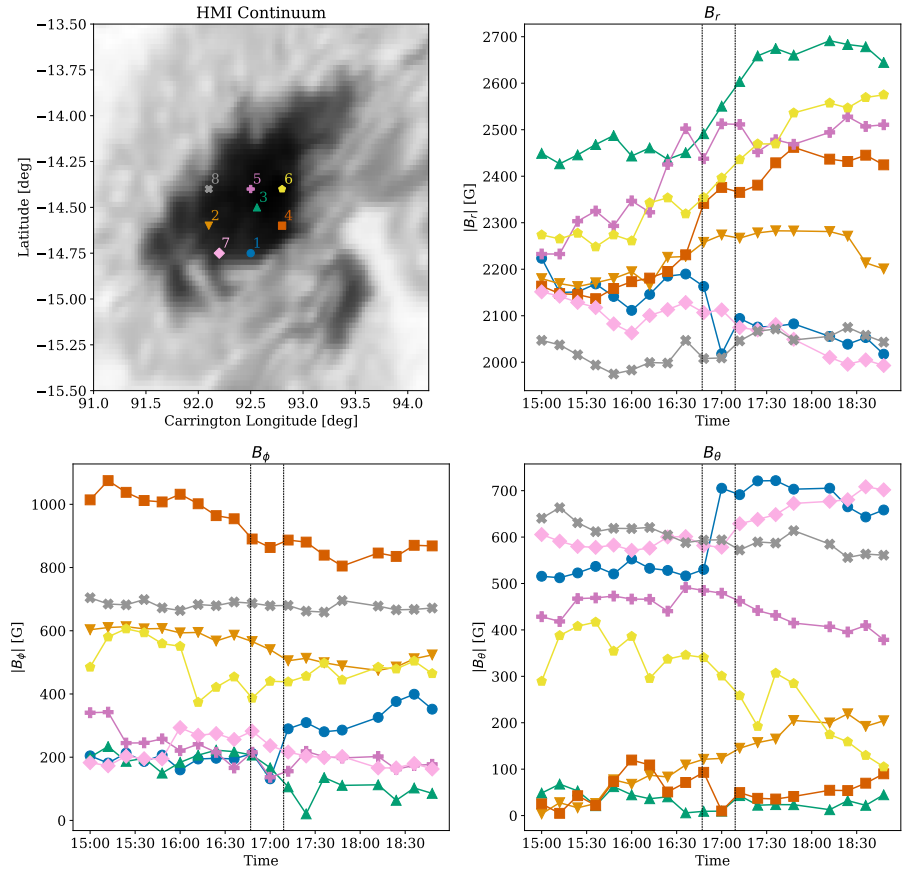


**Figure 3.13:** Timeseries of the three CEA magnetic field components measured by HMI, taken from selected points in the sunspot umbra. The vertical lines show the times of the start of the impulsive phase and the time of the flare peak.

### 3.4 Discussion

of magnetic field changes at the time of the flare activity which was not part of a more gradual change of the field. We investigated the site where oscillatory behaviour was detected after the flare impulse but not before (the northern umbra/penumbra border), and found no significant evidence of field changes which correlated to the appearance of the oscillations. Conversely, there were several areas where there were oscillations before the flare which seemed to disappear after the impulsive phase. Previously we found similar behaviour under the flare ribbons and attributed the lack of oscillations in post-impulsive data to the flare heating. When analysing the HMI timeseries we found that there were many locations which lost oscillatory signal after the flare activity but were not under the ribbons, and instead showed sudden changes to one or more of the magnetic field components.

In figure 3.13 we show several examples of magnetic field timeseries at a variety of locations. Timeseries 1 is under the flare ribbon and shows a clear, abrupt and persistent change to the  $B_\theta$  and  $B_\phi$  components during the flare impulse. Timeseries 4 shows a change to the radial component of the field  $B_r$ , and is located very near the flare ribbon, where oscillatory signal was lost after the flare. Towards the centre of the umbra, away from the ribbons are points 3, 5 and 6, whose timeseries show changes to  $B_r$  and show a lack of oscillations after the flare activity. While this evidence of changing magnetic field parameters could explain why the oscillations at these locations were interrupted, we also find many examples of locations where the magnetic field did not change considerably, such as at points 2, 7 and 8.

From our analysis of HMI data, there were no obvious signs of field changes which correlated with all of the changes in oscillatory behaviour we observed with CRISP, however we found evidence of strong field changes at locations where oscillations disappeared after the flare. An important distinction here is that HMI samples the photosphere, and the CRISP line cores sample the chromosphere. The chromosphere is such a magnetically complex part of the atmosphere that HMI magnetic field values do not necessarily match to e.g. measurements of the chromospheric magnetic field as measured by the weak-field approximation in Ca II 8542 Å (Kleint 2017). It is possible that magnetic field extrapolations based on HMI data may shed some light on the exact configuration, however the presence of the flare directly over the active region makes this analysis very difficult to achieve.

To investigate our interpretations further, we have plotted in Figure 3.14 images from the AIA 171 Å channel, one from before the flare and one from the end of the CRISP observing window. This channel is the most suitable to get an impression of the magnetic activity in the active region. The flare ribbons seen in the CRISP line cores are linked by a newly

### 3.5 Conclusions

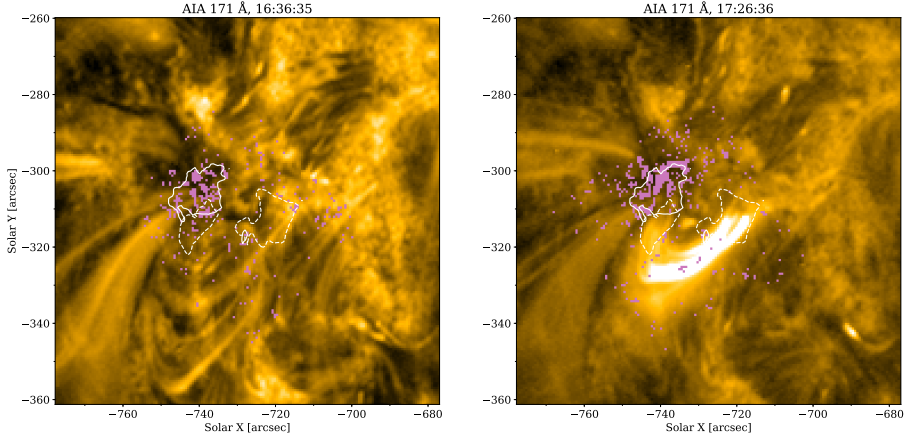


**Figure 3.14:** Images from the 171Å passband from AIA from before (left) and after (right) the flare. The colour scales of the images are different, for the best contrast. Plotted in pink are the locations of macropixels with spectra which produced Gaussian bumps in the Ca II 8542 – 0.2Å results. The solid contours outline the sunspot umbra, using the 40% intensity level of the line wing, and the dashed contours show the flare ribbons, determined by 55% of the maximum intensity value of 8542 Å core at the start of the post-impulsive period.

formed hot loop, which develops after the flare activity into the bright structure shown in the right panel of Figure 3.14. Other larger loop structures are seen emerging from the active region, to the east and north-east of the flare footpoints and sunspot umbra. It can be seen that these loops undergo changes during the flare activity, with some contraction of the loops visible. It is clear from observing this particular wavelength that the magnetic structures in this active region have been altered during the flare activity and this gives weight to our interpretation regarding a change of the magnetic field inclination.

## 3.5 Conclusions

We studied this active region to try and understand the types of oscillatory signals which can be affected or induced by flare activity. We found significant oscillatory behaviour consistent with the theory of MAG waves both before and after the flare. In this first spectrally-resolved analysis of flare chromospheric oscillations using the spectral fitting method, we found that the periodic signals seen in H $\alpha$  and Ca II 8542 Å line core observations were not seen in the line wings or the AIA ultraviolet channels, possibly due to the broader range of heights sampled by line wing observations.

There is evidence of the oscillatory behaviour being altered indirectly by the flare, both in

### *3.5 Conclusions*

the locations of the signals and the periods of the oscillations. The signals were found to have moved from covering almost the whole sunspot umbra before the flare, to being concentrated on the northern umbral border afterwards. There was a lack of signals at the locations of the chromospheric flare ribbons, perhaps due to the intense heating of the plasma at these locations. Significant magnetic field changes in HMI data were observed at some other locations where the oscillatory behaviour disappeared after the flare activity. In both pre- and post-impulsive intervals, the periods at which the oscillations were observed increases radially out from the umbra, but in post-impulsive data the periods are in general longer.

We believe these results are evidence of a changed magnetic environment in the sunspot as a result of the flare activity, and this interpretation is supported by sudden field changes observed by HMI and by images of coronal loops which are connected to the site. Our work provides evidence of the ways solar flares can affect the solar atmosphere, in particular the chromosphere, and that the influence of the flare can be felt over the whole active region.

---

# 4

---

## Simulations of sunspot oscillations

In this chapter, we examine magnetohydrodynamic (MHD) simulations with which we investigated the results of Chapter 3. In that chapter, we presented evidence of changes to chromospheric oscillations over a sunspot, and proposed that the changes were due to a change in the inclination of the magnetic field at the sunspot. We sought to create a simplified version of the atmosphere from which the observations were made, after which we simulated waves propagating through the atmosphere. By altering the starting atmosphere in three ways, we observed changes to the oscillatory structure in the resulting simulations, to validate which is the most likely explanation for the results of our observations. As discussed in Section 1.3.3, the origin of strong chromospheric oscillations over sunspots is thought to be related to the cut-off frequency of the medium, and may necessitate the presence of a chromospheric cavity (Felipe 2019). By using simulations in 2D, we can investigate the magnetic field inclination  $i$  and its effect on the resulting waves. We also study the different oscillatory structures when using two different atmospheric temperature profiles, suggested by Botha et al. (2011) as a cause for changing oscillatory behaviours. The length of the chromospheric cavity is thought by some to have an influence on the oscillatory makeup of sunspots. We investigate this approach by altering the height of the transition region in one set of simulations, and comparing to the simulations which varied  $i$ .

The simulations were performed using the Lare2d code (Arber et al. 2001). A very brief introduction to the code will be presented in Section 4.1, followed by detailing the setup of the experiments in Section 4.2 and then presenting the results of the simulations in Section 4.3. Discussion of the results and conclusions are found in Sections 4.4 and 4.5.

## 4.1 LareXd

LareXd<sup>1</sup> is a pair of Lagrangian remap codes which solve the non-linear MHD equations, using a staggered grid in either two dimensions or three (Lare2d/Lare3d).

The code requires, as inputs, values for the ratio of specific heats,  $\gamma$ , the average ion mass,  $\bar{m}$ , and normalisation factors for length,  $L_0$ , magnetic field,  $B_0$ , and mass density,  $\rho_0$ . All of the variables used in the code are normalised by a combination of these three user-inputted values. The normalised MHD equations as they appear in the code are

$$\frac{D\rho}{Dt} = -\rho \nabla \cdot \mathbf{v}, \quad (4.30)$$

$$\frac{D\mathbf{v}}{Dt} = \frac{1}{\rho} (\nabla \times \mathbf{B}) \times \mathbf{B} - \frac{1}{\rho} \nabla p, \quad (4.31)$$

$$\frac{D\mathbf{B}}{Dt} = (\mathbf{B} \cdot \nabla) \mathbf{v} - \mathbf{B} (\nabla \cdot \mathbf{v}) - \nabla \times (\eta \nabla \times \mathbf{B}), \quad (4.32)$$

$$\frac{D\epsilon}{Dt} = -\frac{p}{\rho} \nabla \cdot \mathbf{v} + \frac{\eta}{\rho} j^2, \quad (4.33)$$

where  $D/Dt = \partial/\partial t + \mathbf{v} \cdot \nabla$  is the advective derivative,  $\mathbf{v}$  is the velocity,  $\mathbf{B}$  is the magnetic field vector,  $p$  is the thermal pressure,  $\eta$  is the resistivity,  $\epsilon = p/\rho(\gamma - 1)$  is the specific internal energy density and  $j$  is the current density.

The code also includes a gravitational term, which is defined along the  $y$  direction in Lare2d. This means the momentum equation (4.31) becomes

$$\frac{D\mathbf{v}}{Dt} = \frac{1}{\rho} (\nabla \times \mathbf{B}) \times \mathbf{B} - \frac{1}{\rho} \nabla p - \mathbf{g}. \quad (4.34)$$

with  $\mathbf{g}$  being a vector describing the gravitational acceleration, which can vary with height.

The code is set up with a staggered grid system, with the capability for non-uniform cell sizes. This means that in every rectangular grid cell, scalar properties (e.g.  $\rho$ ,  $\epsilon$ ) are

---

<sup>1</sup>A practical guide to using the code can be found at <https://warwick.ac.uk/fac/sci/physics/research/cfsa/people/tda/larexd/>

## 4.2 Code setup

defined at the cell centre, while velocities are defined at cell corners and the magnetic field components are defined at the cell edges.

Each timestep of the code is split into a Lagrangian step followed by a remap onto the original Eulerian grid. A Lagrangian specification of a fluid is one which follows the movement of pieces of material, while an Eulerian specification observes physical quantities at fixed spatial locations (Batchelor 1967). The Lagrangian step is a predictor-corrector scheme and contains all of the physics, which is second order accurate in space and time and fully multi-dimensional. The remap step is a geometrical one, which maps the variables used in the Lagrangian step back onto the original grid, in one-dimensional sweeps.

## 4.2 Code setup

The simulations were configured to approximate the Sun’s atmosphere above a sunspot, with representative temperature stratification and simple magnetic field structures. The atmosphere was driven from beneath the photosphere with a spectrum of frequencies to simulate the convective motions which generate waves in the upper atmosphere. The domain covers  $-5400 \text{ km} < x < 5400 \text{ km}$  in the horizontal direction and  $-9000 \text{ km} < y < 9000 \text{ km}$  vertically (that is, radially outwards from the surface). The grid spacing is uniform in  $x$  with  $n_x = 50$  cells, whereas the  $y$  domain has  $n_y = 200$  and is stretched such that greater resolution is given between the photosphere and transition region. The non-uniform grid spacing,  $dy$ , as a function of height,  $y$ , is generated via

$$dy(y) = q_0 \times \tanh\left(\frac{|y - q_1| - q_2}{q_3}\right) \quad (4.35)$$

with  $q_{0-3}$  being variables used to obtain different specific amounts of stretching. The results of the stretching function are shown in figure 4.1.

For the temperature stratification, it is typical to employ a semi-empirical model atmosphere, such as the well known FAL-C (Fontenla et al. 1993) for the quiet Sun. The atmosphere above a sunspot is, however, slightly different and so for studies on sunspot oscillations many authors (e.g. Botha et al. 2011, Jess et al. 2020) employ the “Sunspot M” model by Maltby et al. (1986). The Maltby atmosphere is of roughly the same shape as the FAL-C profile (Fontenla et al. 1993) but is overall at a lower temperature. To investigate an atmosphere more closely resembling our data, we use an inversion of data from

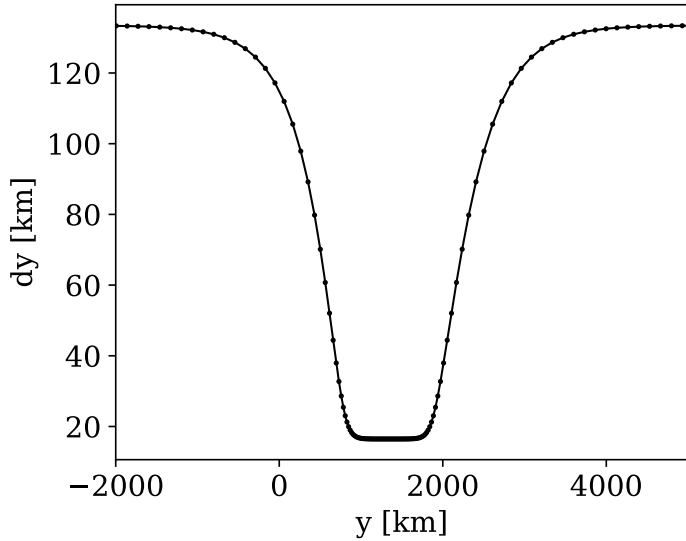


**Figure 4.1:** The spacing between cell centres in the  $y$ -direction, as a function of height, generated with equation 4.35.

the SOL2014-09-06T17:09 flare dataset described in Chapter 3 to get an approximation for the temperature profile in the umbra of the observed sunspot. The inversion was performed with the STockholm inversion Code (STiC), which is described in more detail in Section 2.3.1. A single Ca II 8542 Å line profile was extracted from the centre of the sunspot umbra and inverted using a FAL-C atmosphere as the starting point for the inversion process. Though an averaged profile would be free of discrepancies caused by e.g. localised shocks, we believe a single profile is appropriate as long as the shape of the line is simple, because the main contributor to the resulting temperature profile is the intensity. The temperature profile produced by the code (the “STiC” or “umbral” profile) is displayed along with the FAL-C and Maltby profiles in Figure 4.2. The Ca II 8542 Å line is not sensitive throughout the whole atmosphere, so care must be taken when using only this one line in the inversion process. As seen in Figure 4.2 the profile looks generally similar to the Maltby profile, but at a lower temperature throughout the atmosphere. We stress that this temperature profile was not observed, rather inferred from an observed line profile. The chromosphere of the STiC profile, the region of greatest sensitivity for Ca II 8542 Å, shows the greatest deviation from the other two profiles, while near  $y = 0$  km and at the transition region, the profile matches FAL-C and Maltby quite closely, leading us to conclude that it is an appropriate starting atmosphere for the simulations. Before implementing the profile in Lare2d it was altered at the  $y = 0$  km point to match the Maltby profile exactly, in order to remove the kink in the profile, and ensure a smooth

## 4.2 Code setup

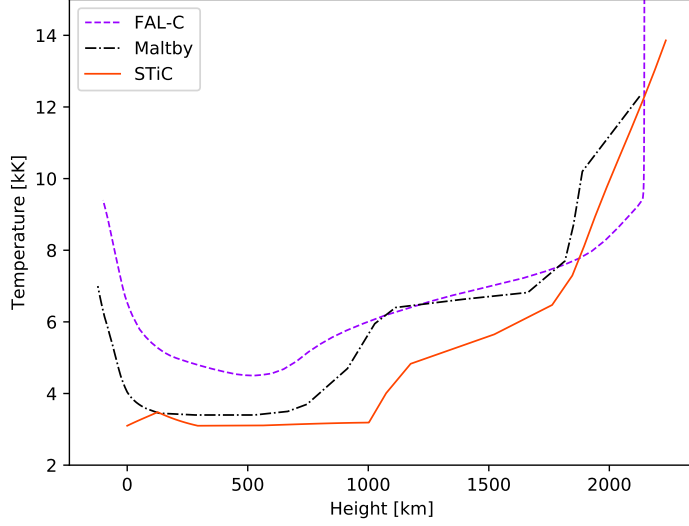


**Figure 4.2:** Comparison of the FAL-C (dashed line) and Maltby (dot-dashed line) temperature profiles with the one returned by the STiC inversion of the Ca II 8542 Å profile from an umbral pixel (solid line).

transition at the “surface”.

The temperature profile of the simulation initial conditions is drawn from the chosen model, but that only covers the range of heights between the photosphere and the start of the transition region. Outwith these bounds, the temperature profile is of the following form:

$$T(y) = \begin{cases} T_{ph} - Ay, & y < 0. \\ T_{ph} - 1 + (T_c - T_{ph})^B, & y > y_{TR}, \end{cases} \quad (4.36)$$

where

$$B = \frac{\tanh(\frac{y-y_c}{b}) + 1}{2}, \quad (4.37)$$

$A$  and  $b$  are constants, and the subscripts  $ph$ ,  $TR$ , and  $c$  correspond to the photosphere, transition region, and corona respectively.

The magnetic field was set to be uniform across the grid in all of the simulations. The strength of the field  $B$  was set at a typical value for the observed sunspots, 2.4 kG, and the field inclination  $i$  determined the two components of the field via  $\mathbf{B} = (B \sin i, B \cos i)$ .

### 4.3 Results

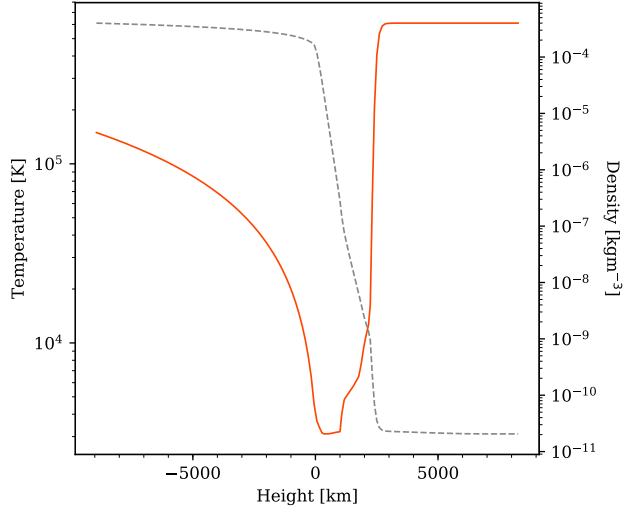


**Figure 4.3:** The temperature (solid line) and density (dashed line) stratification across the entire vertical span of the simulation grid, when using the umbral model.

Hydrostatic equilibrium was achieved by setting  $Dv/Dt = 0$  in equation 4.34 and solving to find the required density stratification when setting the initial conditions for the code. There were no forces in the horizontal direction due to the lack of temperature and magnetic field gradients. Gravitational acceleration was set to a constant  $280 \text{ m s}^{-2}$  for the majority of the grid, dropping to zero at the top of the corona. The resulting temperature and density profiles in the umbral atmosphere are shown in Figure 4.3.

The atmosphere was driven at the lower  $y$  boundary by a spectrum of sinusoidal waves with only a  $y$  component of velocity, made to resemble a red-noise background (equation 2.8, Section 2.2.2) with index  $\alpha = 1.2$  and random phase values at each frequency. The velocity driver was the same for each simulation which was carried out. Outputs from the code were drawn so that the results had a “cadence” of  $\Delta t = 17 \text{ s}$ .

## 4.3 Results

We begin by explaining the outputs of the simulations and how they relate to a typical observation with a solar telescope. We then look closely at the results from a simple simulation — one with the STiC umbral temperature profile and a uniform, vertical magnetic field. We then present three sets of simulations which each investigated different effects.

### 4.3 Results

The same simulation setup was repeated several times while altering the magnetic field inclination,  $i$ . We performed five simulations, where the field was inclined by increments of 15 degrees in each iteration, from zero up to a maximum of 60 degrees. In this set of simulations (Set 1) we investigate the effect of the magnetic field inclination on the resultant oscillations.

Second, an equivalent set of simulations will be discussed, but using the Maltby temperature profile, instead of the umbral profile which was extracted from the observed data in Chapter 3. The same five magnetic field inclinations were used as in Set 1, to investigate the difference in temperature and how it affects the dominant periodicities. This will be referred to as Set 2.

Lastly, in Set 3, five simulations were carried out using the STiC umbral temperature profile, but scaled in the  $y$ -direction so that the transition region was placed at different physical altitudes. The scaling was achieved by multiplying by a scaling factor, with values (0.6, 0.8, 1.0, 1.2, 1.4). The magnetic field inclination was kept at zero (vertical field) for all of these simulations, so that the only change was the geometrical length of the cavity between the temperature minimum and the transition region.

#### 4.3.1 Relationship of simulated parameters to observables

By looking closely at how different physical parameters measured in the simulations evolve over time, we can see how in the real solar atmosphere these waves generate observable intensity oscillations, as well as the more obvious velocity signals which are inherent in the velocity vector within the code. Figure 4.4 shows six parameters sampled in the upper chromosphere of the vertical magnetic field simulation (the  $i = 0^\circ$  simulation of Set 1): the two orthogonal velocity components,  $v_x$  and  $v_y$ , mass density, pressure, temperature, and the velocity along the direction of the magnetic field,  $v_i$ . This is a useful measure because for the most part the waves are guided along the field lines, and we can see that in the vertical magnetic field ( $i = 0^\circ$ ) this is identical to the vertical velocity,  $v_y$ . In the first simulation in Set 1, almost all of these parameters exhibit clear oscillatory behaviour, with the exception of the horizontal velocity  $v_x$ .

When observing with telescopes, we can measure the intensity of the light we receive from sources, its wavelength, and its polarisation state. Velocities can be obtained from, among other things, the shift of spectral features resulting from movement of the source object along the line of sight. The line-of-sight velocity would closely follow the vertical velocity

### 4.3 Results

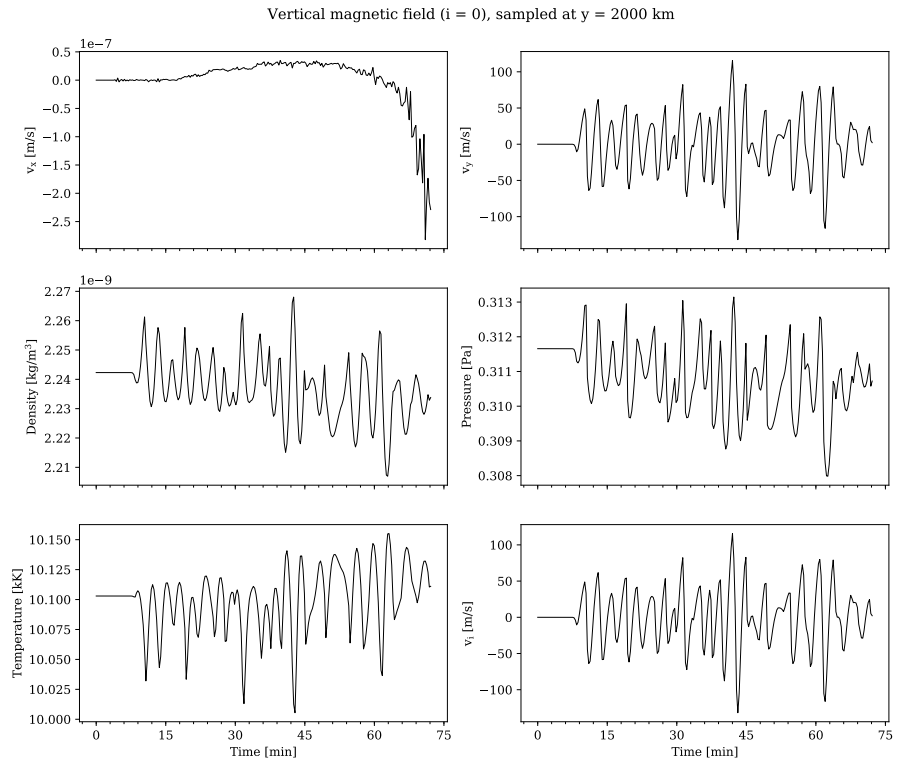


**Figure 4.4:** A variety of physical parameters in the vertical magnetic field simulation, drawn from a height of 2000 km. The bottom right panel displays the velocity in the direction of the magnetic field lines,  $v_i$ . Note that the scaling of the  $v_x$  panel is significantly smaller than the other velocities.

### 4.3 Results

$v_y$  if one was observing something in the centre of the solar disk. The polarisation state of light can be related to the components of the magnetic field vector, which can be directly drawn from the simulation results, and measured in spectropolarimetric observations by the weak-field approximation or inversions (see Section 2.3).

The intensity of light is slightly more obtuse, and requires considering the radiative transfer through the atmosphere to fully understand. Generally speaking, small increases in temperature should correspond to increases in brightness of the continuum radiation and the line core intensity. However, changes to density will affect the scattering, absorption and emission of the atomic populations which result in the observed spectral line shapes. The Lare2d code assumes a single species population, meaning that local concentrations and non-uniform ionisation fractions of, say, Ca II atoms cannot be accurately represented. For these reasons, we will be analysing oscillations in the velocity at various locations on the simulation grid, as an analogue to observed velocity fluctuations.

However, all measurements we make are of light which has undergone the radiative transfer process through the Sun's atmosphere. As discussed in Section 2.1.2, light at a wavelength  $\lambda$  can originate from a range of heights, mostly measuring the altitude where  $\tau_\lambda = 1$ , for optically thick lines. This means that we cannot be sure that we are measuring the same atmospheric height at all times, as the opacity of the atmosphere can be affected by, for example, heating due to flare activity.

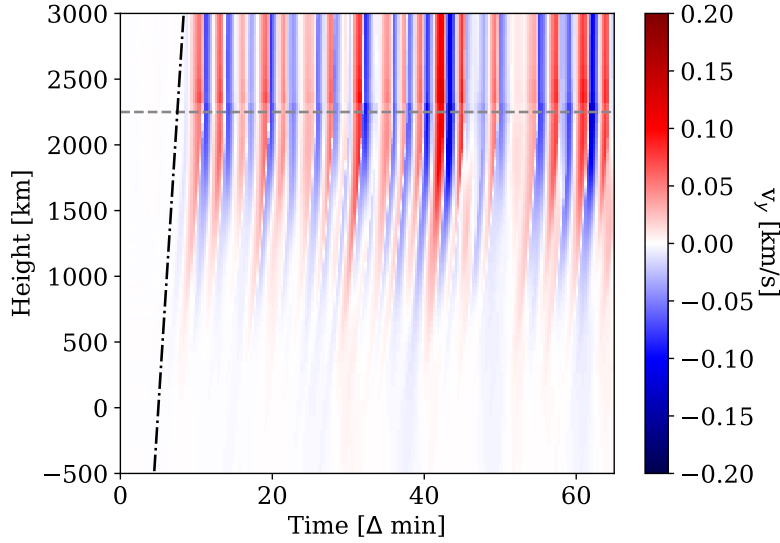
#### 4.3.2 Vertical magnetic field

Figure 4.5 shows the vertical velocity  $v_y$  in the atmosphere as a function of height, for the simulation using the STiC umbral temperature model and with a constant magnetic field with no inclination. Here one can see evidence of the waves travelling upwards from below the surface into the chromosphere; it is  $\sim 10$  minutes into the simulation before the waves are visible there. The amplitude of the waves increases in the upward direction, due to the drop in density (refer to the dotted line in Figure 4.3). The waves travel at the sound speed of the plasma,  $c_S$ , introduced in Section 1.3.2, which can be calculated with

$$c_S^2 = \frac{\gamma p}{\rho} = \frac{\gamma n k_B T}{n \bar{m}} = \frac{\gamma k_B T}{\bar{m}}, \quad (4.38)$$

where  $k_B$  is the Boltzmann constant,  $n$  is the number density, and  $\bar{m}$  is the average particle mass. Using approximate values for the chromosphere of  $T \sim 10^4$  K,  $\bar{m} \sim m_{proton}$ , the

### 4.3 Results



**Figure 4.5:** The velocity in the vertical direction as a function of height and time drawn from part of the umbral atmosphere simulation with a vertical magnetic field. The horizontal dashed line is at  $y = 2250$  km and shows the point of the steepest temperature gradient. The dashed-dotted line shows the gradient equal to the sound speed at a temperature of  $10^4$  K.

sound speed is found to be of the order  $10 \text{ km s}^{-1}$ . The temperature increases so rapidly over the transition region and into the corona that the waves fill the remainder of the simulation grid almost instantly once they reach this point.

We can get an understanding of the typical periods of the waves which are present in the velocity data by calculating the Fourier power spectrum (FPS) of the corresponding timeseries (Section 2.2.1). In Figure 4.6, the FPS has been calculated for each height in the atmosphere, which allows us to see the dominant periods as the waves propagate through the atmosphere. At  $y = 0$  km the maximum power is located at around 320 seconds, while at chromospheric heights power is concentrated at lower periods. A strong peak is visible at 220 seconds, with some weaker signals from 100–200 seconds. We must keep in mind that the velocity driver was set up with a red-noise spectrum, so power increases as period grows. Any deviations from that shape must be due to physical processes as the waves propagate in the simulated atmosphere. Refer to the top panel of Figure 4.7 shows a velocity timeseries from far below the “surface” of the atmosphere. The cut-off frequency of the plasma filters out longer period signals, so in the power spectrum we expect to see a steady rise in power up to a certain period value (at the cut-off), after which the power drops off.

### 4.3 Results

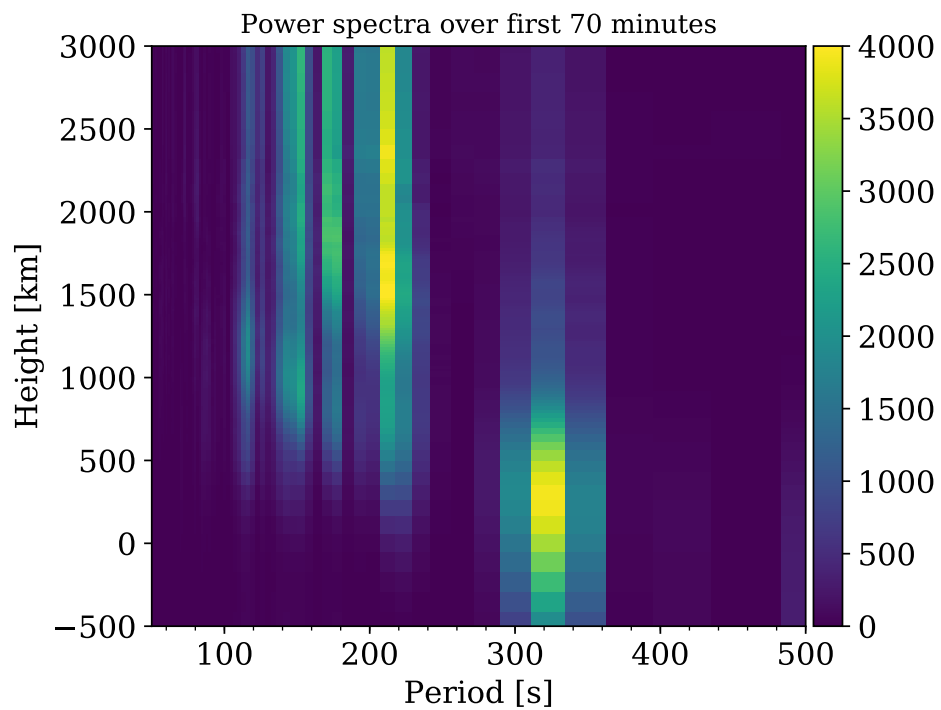


**Figure 4.6:** The colour scale shows the Fourier power of periodic signals (in arbitrary units, on a linear scale) in vertical velocity as a function of height in the umbral atmosphere and period of the signal.

### 4.3 Results

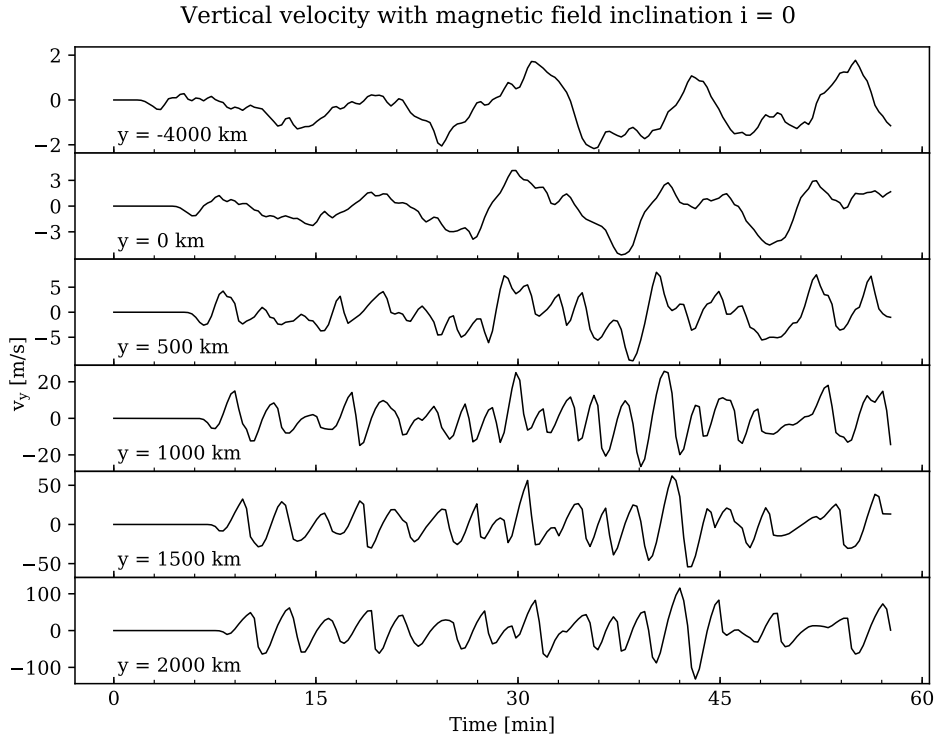


**Figure 4.7:** Each subplot shows a different height in the atmosphere, and the vertical velocity at that height over the first  $\sim$ hour of the umbral atmosphere simulation with  $i = 0$ .

An interesting feature of Figure 4.6 is that the strong power which is present throughout the atmosphere at  $y > 0 \text{ km}$  is displayed as vertical bands on the plot. The temperature in the atmosphere is at its lowest between  $0\text{--}1000 \text{ km}$ , after which it rises to chromospheric levels before rapidly increasing at the transition region at approximately  $2500 \text{ km}$ . The fact that there is not a blending of power across period bins as one moves up the atmosphere shows that the cut-off point resonance (identified by the drop off in power) does not follow the temperature as it changes, rather that the cut-off frequency filter operates at the base of the atmosphere (at the minimum temperature) and the remaining waves propagate through the upper atmosphere.

As seen in Figure 4.5 the waves change some of their properties as they propagate up the atmosphere. A more in-depth look at the height variations in Figure 4.7 shows timeseries of the vertical velocity at specific values of height: deep below the “surface” at  $y = -4000 \text{ km}$  and also increasing heights above the surface to the upper chromosphere in  $500 \text{ km}$  steps. We can see that the velocity profile below the surface has an amplitude of around  $1 \text{ m s}^{-1}$ , with a variety of oscillatory timescales, which are generated by the driven lower boundary.

### 4.3 Results

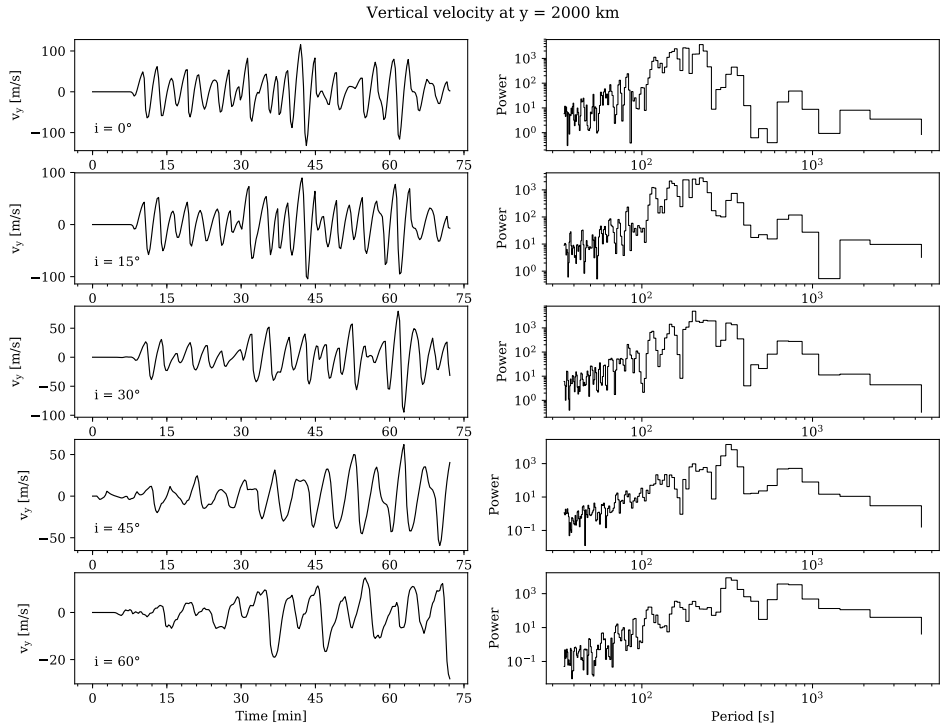


**Figure 4.8:** Vertical velocity oscillations from Set 1 simulations, with the magnetic field inclination increasing with each row of the figure. Each row shows the  $v_y$  signal at a height of 2000 km in the left panel, and its corresponding Fourier power spectrum in the right. Note the decreasing scale of the  $y$ -axes in the left column.

At  $y = 0$  km the velocity timeseries looks much the same as at the subsurface level, with a phase difference caused by the travel time. It is at the heights above the surface that the strong signals at the 1–5 minute period range come through. There is certainly  $\sim$ 3-minute periodicity present at  $y = 500$  km, however the clearest signals emerge at greater heights. This verifies Figure 4.6, as we can see the highest values of power at these periods are above 1000 km.

#### 4.3.3 Comparing magnetic field inclinations

The rest of the Set 1 simulations investigated the effect of changing the magnetic field inclination. The inclination was varied in 15 degree steps, up to 60 degrees, keeping the total magnetic field strength constant at  $B = 2400$  G. Figure 4.8 shows vertical velocity oscillations from the upper chromosphere, drawn from each of these simulations. Note that the upper left panel in this figure is the same timeseries as in the lower panel of

### 4.3 Results

Figure 4.7, over a slightly different time interval. The vertical velocity amplitude scales grow smaller as the inclination increases, going from maximum values of  $100 \text{ m s}^{-1}$  at  $i = 0^\circ$  to  $20 \text{ m s}^{-1}$  in the case where  $i = 60^\circ$ .

In Chapters 2 and 3, we saw that power was seen to increase or level off at longer periods in observations, and we used red-noise backgrounds to categorise the spectra. Comparing the power spectra seen in the right-hand column in Figure 4.8 to the results from observations (Figures 2.6 and 2.7), we see that power *decreases* at longer periods in the simulated spectra. This is likely because the only source of waves in the simulations are those from the lower boundary which are being filtered out, whereas in real physical data there is a much greater amount of interfering signals originating from above and around the measured space. In addition, the velocity from the simulations is drawn directly from an exact position, while in real data, an intensity or velocity signal measures a spread of heights from across the sensitivity of the spectral line.

The timeseries in Figure 4.8 from simulations with  $i > 30^\circ$  look very different to the others. The points where the power stops increasing with period,  $P$ , are at much higher values of period with peaks at  $\sim 300$  seconds, as opposed to the peaks closer to  $\sim 200$  seconds in the  $i \leq 30^\circ$  simulations. However, when comparing  $i = 45^\circ$  and  $i = 60^\circ$ , the power spectrum peaks are almost identical at  $P \approx 330 \text{ s}$ . When  $i = 60^\circ$  the behaviour of the spectrum below the peak period is different, with more pronounced minor peaks between 100–200 seconds.

There is a local peak in power at  $P \approx 330 \text{ s}$  in all five of the simulations, but in the cases where  $i \leq 30^\circ$ , this peak is suppressed, just below the global maximum at around  $P = 200 \text{ s}$ . This is evidence of the cut-off frequency being much lower in the atmospheres with highly inclined fields. The fact that power remains present at  $\sim 330\text{s}$  in the other simulations is possibly because of the distance travelled, and the speed of the waves. If the distance from the surface to the chromosphere is  $\sim 2000 \text{ km}$  and the waves travel at  $\sim 10 \text{ km s}^{-1}$ , then the waves reach the top of the chromosphere in only 200 seconds, meaning longer period disturbances have not had time to fully decay by the time we detect them. Because of this, their significance is drastically reduced but not fully removed from the spectrum. We note that this effect would be lesser in the  $i > 0^\circ$  cases, as the inclination of the field means a longer travelling distance for the waves as in the vertical field.

Figure 4.9 allows us to compare the vertical velocity as a function of height and time, across the five different simulations in this set. By comparing each of the panels, it is clear that in the simulations with more inclined fields, the oscillations in vertical velocity have

### 4.3 Results

longer periods. There is very little difference in the first two panels ( $i = 0^\circ$  and  $i = 15^\circ$ ), which is expected as the inclination change translates to a  $\cos(15) = 4\%$  difference.

In the two simulations with  $i > 30^\circ$ , there are velocity signals in the upper parts of the atmosphere at times before the waves from the driven lower boundary could have reached those locations. These are most likely initial pressure imbalances at the upper boundary, as one can see in the  $i = 45^\circ$  panel of Figure 4.9 the velocity signals seem to start at the upper left of the plot, and travel downwards, losing amplitude. These signals are apparent in the timeseries plotted in Figure 4.8 but are quickly overtaken by the driven waves travelling upwards.

The corresponding power spectra as a function of height are displayed for Set 1 of the simulations in Figure 4.10. Note that the  $x$ -axis is a logarithmic scale, and the colour scale is displaying  $\log_2 \text{Power}$ . In all these plots we can see that the velocity driver imparts a lot of power at 600–700 s and also at  $\sim 300$  s at the base of the atmospheres. In the  $i = 0^\circ$  and  $i = 15^\circ$  simulations, the resulting power spectra at higher locations look very similar, with power growing as period increases steadily until a dropping-off point. We would expect this drop to occur at the cut-off period, and this seems the case for these two simulations as the power drops rapidly at just over 200 seconds in the spectra above  $y = 500$  km. Although the cut-off period for these two cases is seemingly almost identical (and should be 4% different if following the theory), the more minor bands of power between 100–200 seconds are not exactly the same.

The simulation with  $i = 30^\circ$  shows different behaviour to the previous two. While the actual peak bin of power in the spectra is at a slightly lower period value than in the  $i = 0^\circ$  and  $i = 15^\circ$  simulations, there is a large “smudge” of power at higher periods (200–300 s) which could be evidence of a larger cut-off period. The  $i = 45^\circ$  and  $i = 60^\circ$  simulations look very similar to each other, both of which keeping much the same spectral structure when comparing the photospheric and chromospheric heights. The  $i = 45^\circ$  simulation has very strong power at  $P \approx 300$  s in the upper atmosphere, having grown in power when compared to the power at  $y = 0$  km, and the  $i = 60^\circ$  simulation has additional signal above 300 seconds.

In the latter three panels in Figure 4.10 there are three distinct vertical bands of power covering the whole atmosphere between periods of 100–200 seconds. On close inspection one can see these bands in the first two panels, though they are less evident. It is unclear whether the power at these periods is an indication of physical processes such as reflections within the chromospheric cavity. What is likely is these signals are at frequencies

### 4.3 Results

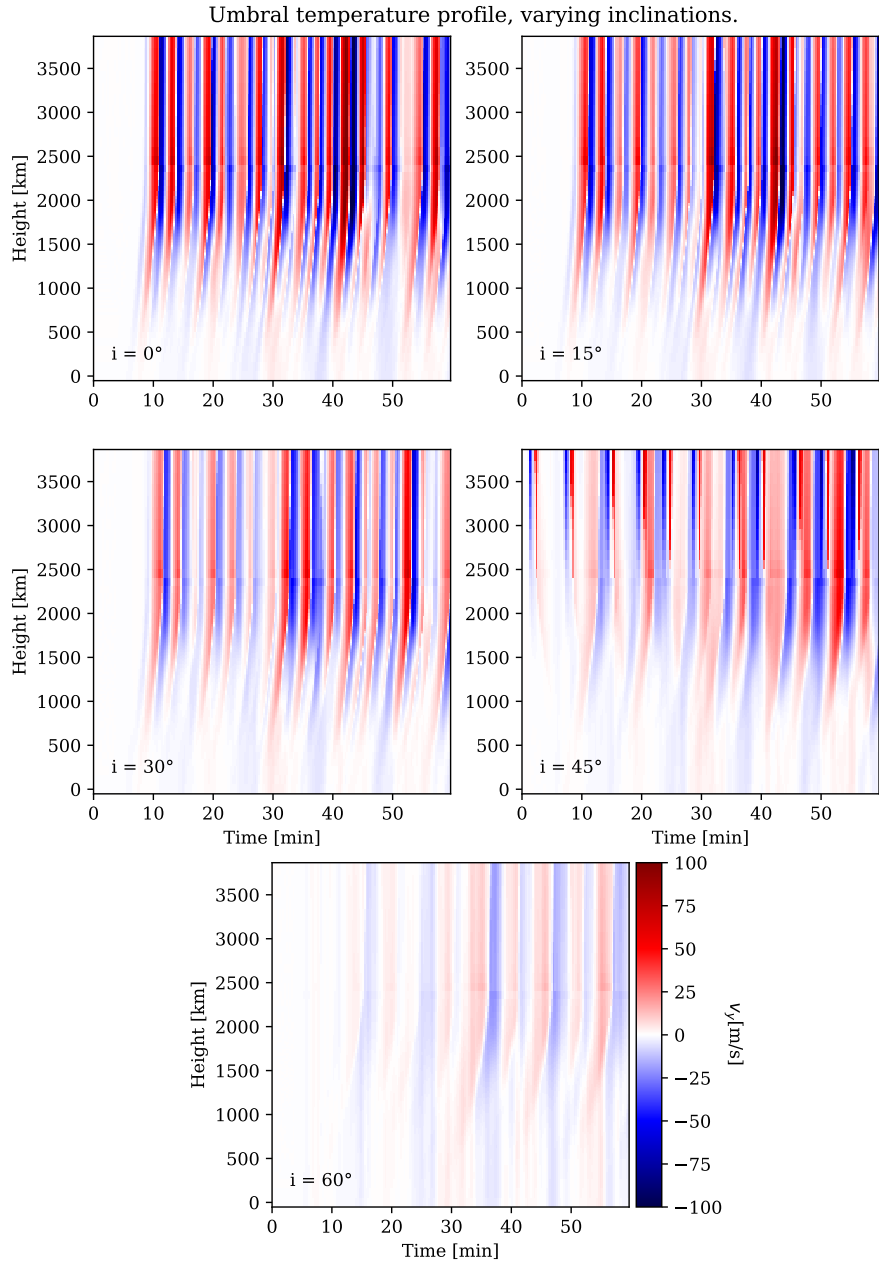


**Figure 4.9:** The vertical velocity as a function of height and time over the first  $\sim$ hour of simulations with the umbral temperature profile and varying magnetic field inclinations. The colour scale is constant across the five subplots.

### 4.3 Results

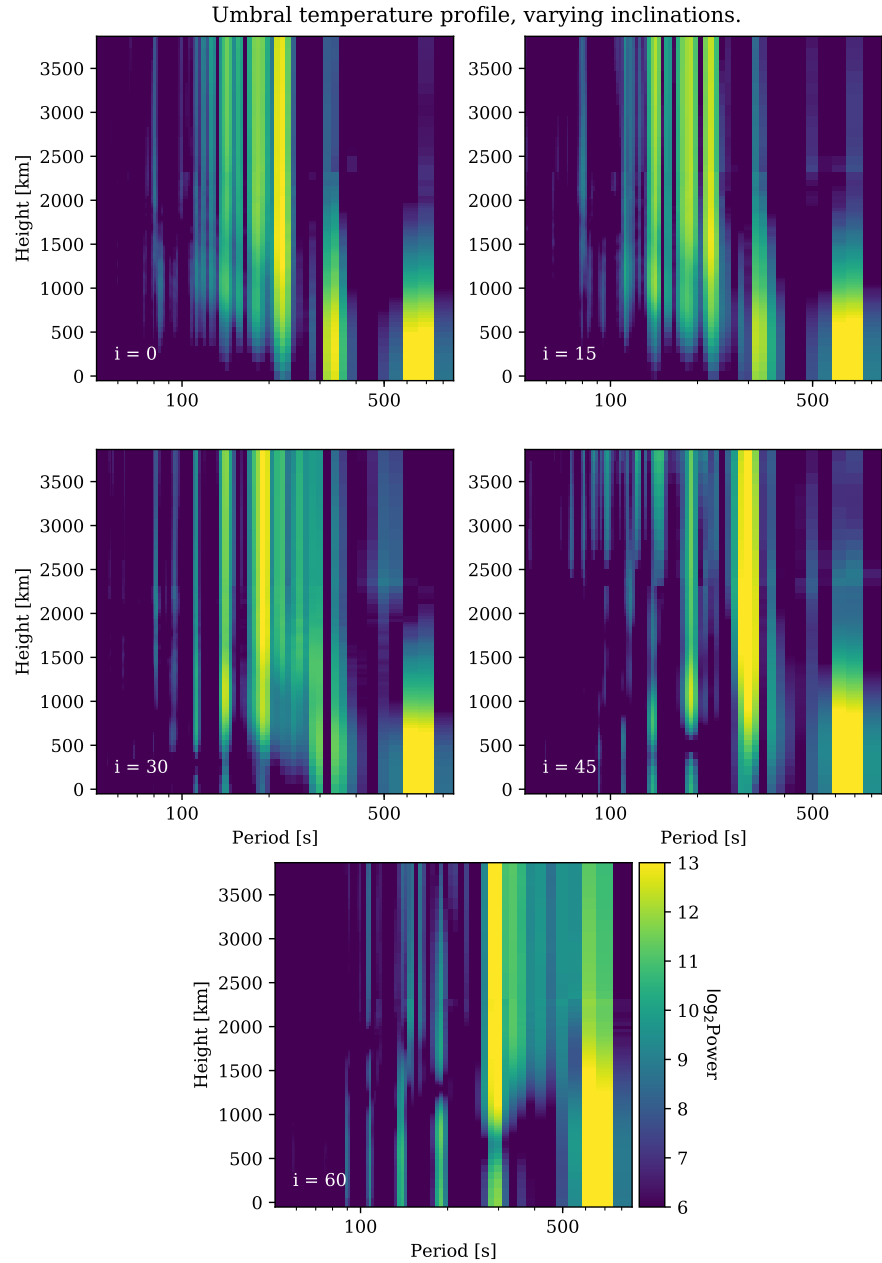


**Figure 4.10:** Power spectrum of  $v_y$  as a function of height, comparing simulations with umbral atmospheres and varying field inclinations. Note that the x-axis is logarithmic, and the colour scale is logarithmic in base 2 and is constant across all subplots.

### 4.3 Results

which were strong in the velocity driver spectrum, and because they are below the cut-off period these were not heavily affected by the Lamb effect.

#### 4.3.4 Maltby profile atmospheres with varying inclinations

Figure 4.11 shows the power spectra as a function of height of vertical velocity oscillations in the simulations of Set 2. In this set the temperature profile used was the Maltby Sunspot M profile. The Maltby atmosphere has a similar shape to the umbral atmosphere in terms of the locations of the large temperature gradients, but the atmosphere is hotter by  $\sim 2$  kK at the lower chromosphere than the umbral profile. This temperature difference corresponds to a change in the cut-off period of the medium at the chromosphere, as shown in Figure 4.12. Here we show the theoretical cut-off period in a vertical magnetic field, calculated at each value of height using the pressure and density —drawn from the simulation results at the first timestep— to obtain the sound speed,  $c_S$ . The cut-off period  $P_c$  is then calculated via

$$P_c = \frac{2\pi}{\omega_c} = \frac{4\pi c_S}{\gamma g \cos i}, \quad (4.39)$$

where  $g = 280 \text{ m s}^{-2}$  is the gravitational acceleration, and  $\omega_c$  is the cut-off (angular) frequency (Equation 1.3). What we see here is that the cut-off period for the hotter Maltby atmosphere is  $\sim 100$  seconds greater than the umbral atmosphere at the point of greatest difference. However, comparing the sub-panels of Figures 4.11 to the ones shown in Figure 4.10, for each value of inclination the cut-off period throughout the atmospheres is very close to equal. This can be explained by what was mentioned above, in Section 4.3.2, that it is actually the value at the lowest temperature part of the atmosphere which mostly affects the resulting oscillations. From Figure 4.12, the minimum values of the cut-offs from these two temperature profiles differ by only  $\sim 10$  seconds.

The results displayed in Figure 4.11 (Set 2) look very similar to Figure 4.10 (Set 1), because although the temperature profiles vary, their minimum temperature values are quite similar. We see the same behaviour in the panels with increasing inclinations, as fewer long period signals are filtered, and in the panels with  $i \geq 45^\circ$  there is little to no filtering of the long period signals. The main difference between the two sets of simulations is the appearance of dark sloping bands in the power spectra/height plots which are clear in the top two panels of Figure 4.11, and present but less obvious in the  $i = 30^\circ$  panel. On closer inspection there is a similar trend in the power plot of the first simulation

### 4.3 Results

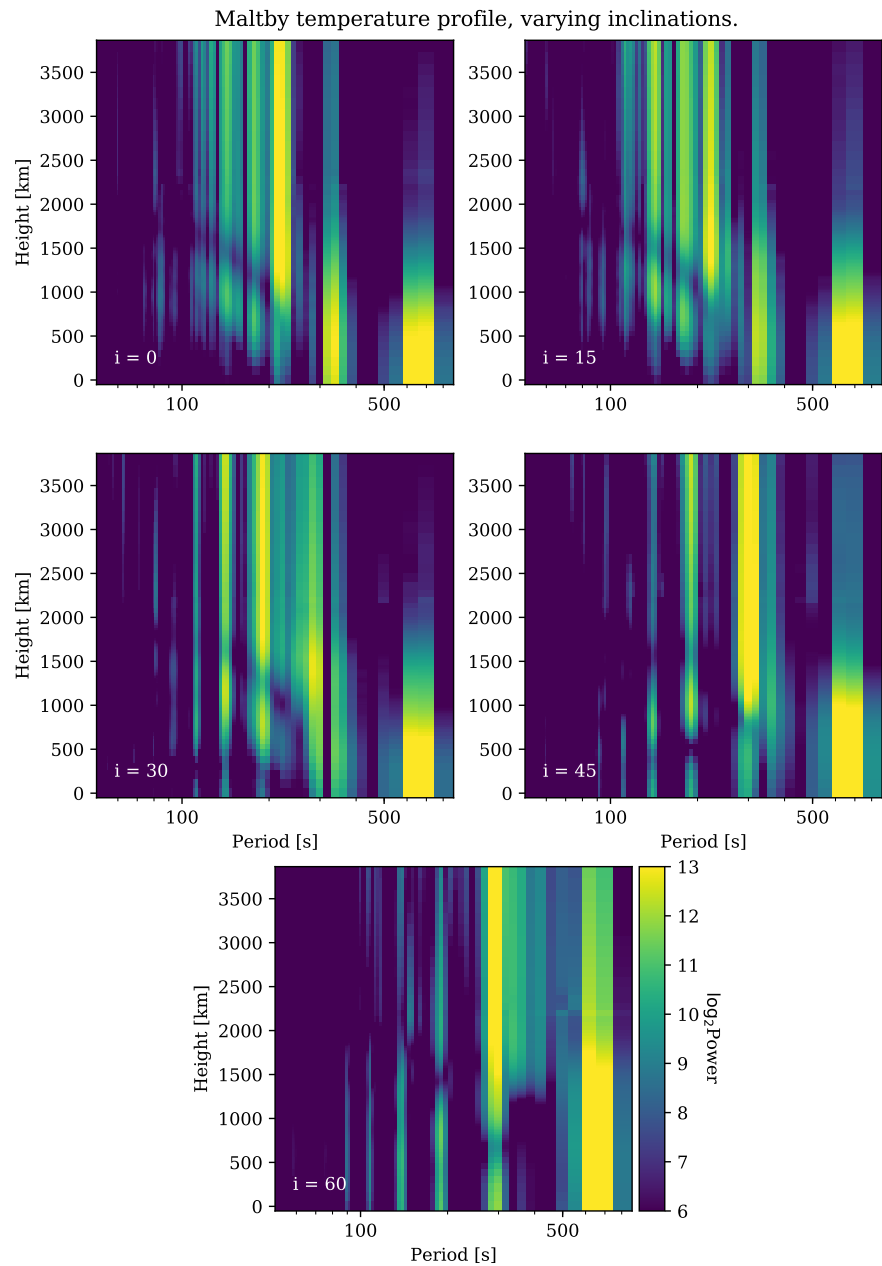


**Figure 4.11:** Similar to Figure 4.10, but for the set of simulations which used the Maltby temperature profile.

### 4.3 Results

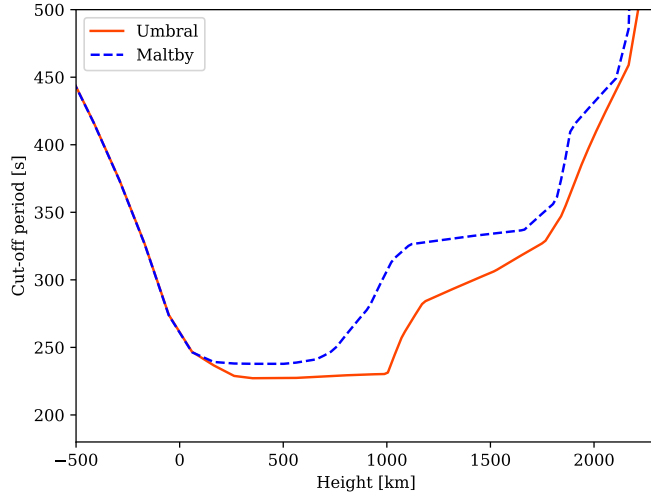


**Figure 4.12:** The variation with height of the theoretical value for the cut-off period in the STiC umbral (orange solid line) and Maltby (blue dashed line) atmospheres.

from Set 1 (Figure 4.10), but it is much less obvious than in the Set 2 equivalent. The bands indicate a drop in power at a certain period under 200 seconds for each height between approximately 1000–2000 km, the period of which falls as the height grows. This could be evidence of reflected waves causing destructive interference at different heights. The presence of the dark bands in Maltby simulations but not STiC umbral temperature profiles could be due to fine differences in the locations and steepnesses of temperature gradients.

The dark bands appear to be linear when comparing height to period on linear axes between  $P = 100$  s and  $P = 180$  s. The gradient of the lines for the first two simulations in Set 2 was estimated by observing the height of minimum power at each value of period, and both were found to fit well with gradients of  $-6.85$  and  $-6.58$  for the simulations with  $i = 0^\circ$  and  $i = 15^\circ$ . Since the gradient of the line would have units of  $\text{km s}^{-1}$ , it is possible the gradient is related to the sound speed throughout the lower atmosphere which is of the order  $\sim 10 \text{ km s}^{-1}$ . The intercepts of the lines were similar, both having values of approximately 2450 km, which is the approximate height of the transition region. This gives credence to the idea that the drops in power at these heights are a consequence of reflected waves in the cavity between the transition region and the photosphere.

### 4.3 Results

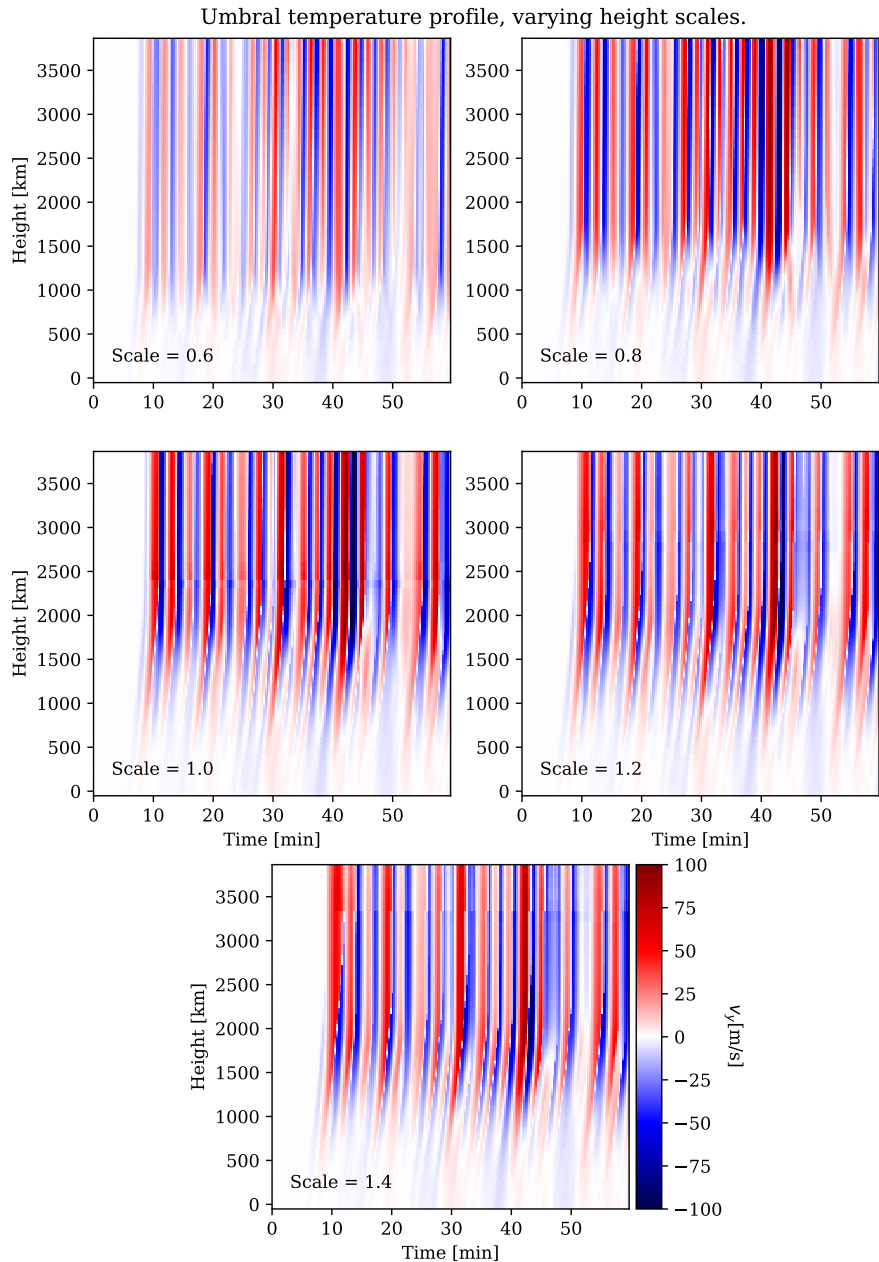


**Figure 4.13:** Similar to Figure 4.9, but for the set of simulations with varying temperature profiles.

### 4.3 Results

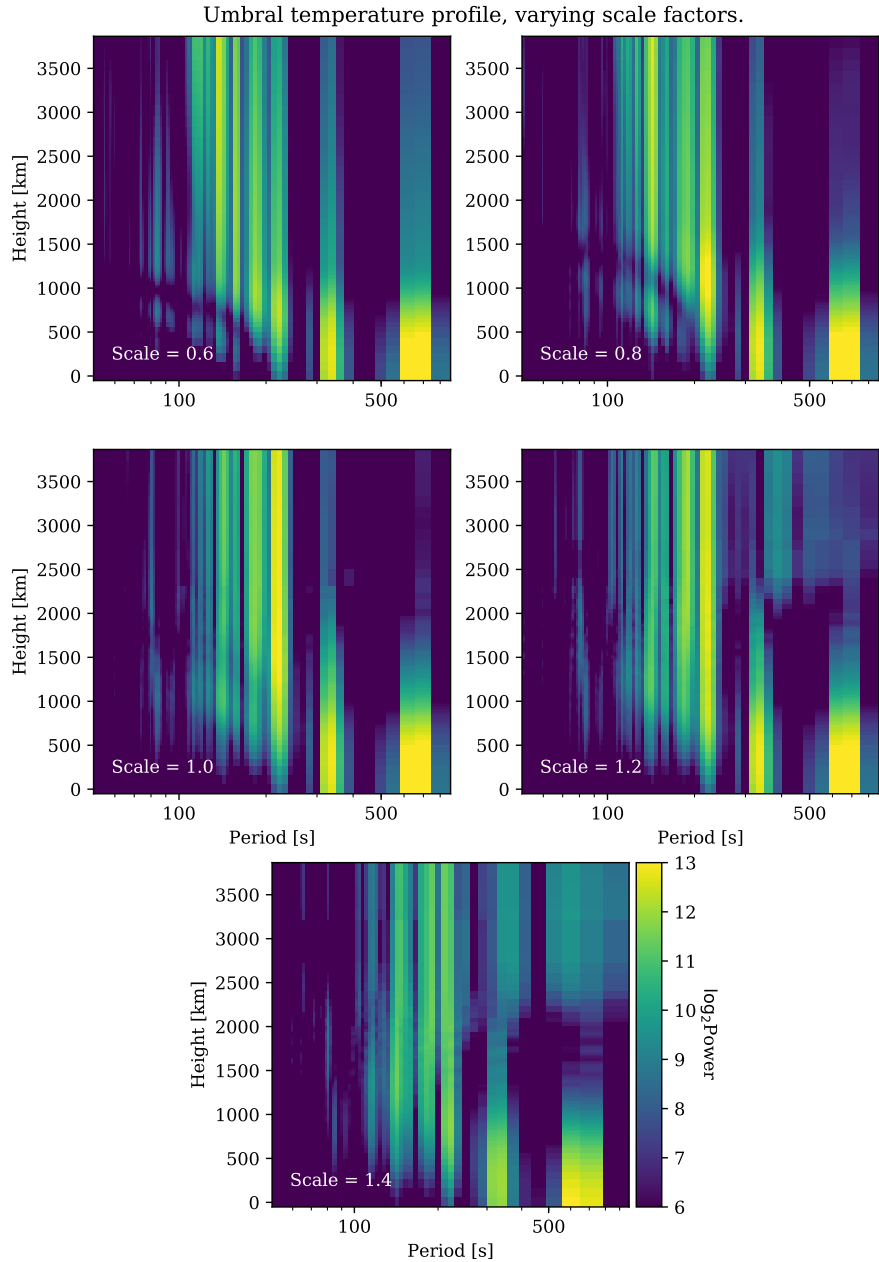


**Figure 4.14:** Similar to Figure 4.10 but for the set of simulations which varied the height-scaling of an identical temperature profile.

### 4.3 Results

#### 4.3.5 Varying the height of the transition region

The final set of simulations (Set 3) kept the magnetic field fixed at vertical alignment, and instead altered the height scale of the STiC umbral temperature profile between each individual simulation. This was performed before setting up the density to achieve hydrostatic equilibrium in the initial conditions, and therefore the density structure for each of these simulations was similarly changed. Figure 4.13 shows the vertical velocity as a function of height and time for each of the scaled atmospheres. The amplitude of the velocity signals increases as the scale factor increases, again due to differences in density. Each of the simulations features a region where the most interference from reflected waves is visible. This “reflection zone” starts a few hundred kilometres from the surface and covers a greater height range as the scale factor increases. In particular the first two panels of Figure 4.13 display the reflected waves clearly. They are identifiable where disturbances move down the atmosphere (in height) as time increases. It is possible that the reflected waves in the other simulations are present but masked by stronger upward travelling waves.

As seen in Figure 4.14, in simulations with varying height scales, the most dominant period at chromospheric heights remains at approximately 200 seconds for all scale factors. The spectra below 200 seconds show similar behaviour in each simulation of the set (steady increase of power with period), but the specific makeup of this part of the spectra does differ when comparing the different scales, suggesting the change in cavity size affects the shorter-period part of the spectra but not the cut-off period itself. There is a noticeable amount of power at high periods in the upper atmospheres of the simulations with a greater than one scale factor. The cause of this is not immediately obvious, but the power increase is still orders of magnitude smaller than the peak period signals, and would be unlikely to affect the dominant oscillatory period in observations made of these atmospheres.

The same dark sloping band which was discussed in section 4.3.4 is visible in the first two height scales. By observing this behaviour on linear axes we were able to see that the same linear trend is visible, with similar gradients to the measured bands from Set 2 of approximately  $6.5 \text{ km s}^{-1}$ . However, in this case the trends are shifted down the height axis, with intercepts on the height axis of roughly 1200 km and 1650 km for scaling factors of 0.6 and 0.8 respectively. The fact that the behaviour of the drops in power follow the height scaling, suggests that it is indeed linked to the size of the chromospheric cavity.

## 4.4 Discussion

In the previous section we presented three different sets of five simulations, with the hope of exploring various effects which could alter sunspot oscillations in the way which was observed and reported in Chapter 3. Simulation Set 1 used a temperature profile inverted from observations of a sunspot umbra, and varied the magnetic field inclination. Set 2 was similar to the first but used the Maltby sunspot model M atmosphere for the temperature stratification. The third set of simulations kept the magnetic field constant and instead changed the height scaling of the STiC umbral temperature profile, in effect altering the physical length of the cavity between the temperature minimum and the transition region, similar to (Jess et al. 2020), but keeping the cut-off period constant. All of the 15 simulations used the same velocity driver, and we analysed how the waves developed throughout the atmosphere by plotting the velocity as a function of time as well as the power spectra of velocity timeseries as a function of height.

The value obtained for the cut-off period in the vertical magnetic field was just over 220 seconds (Figure 4.12). This is just slightly higher than the often-quoted “3-minute” oscillations that we expected. The theoretical value depends on the gravitational acceleration and the sound speed, which itself varies with the temperature and the average particle mass  $\bar{m}$ . In our simulations, we chose a single species which is fully ionised and with an average ion mass of  $1.2m_p$  and  $\bar{m} = 0.6$ . This is most likely the reason for a longer cut-off period, as it varies as  $\bar{m}^{\frac{1}{2}}$ . At the temperature minimum region, the value of  $\bar{m}$  would likely be closer to 1.2–1.3, yielding a period of  $P_c \approx 160$  s.

It was noted that in all of the power spectrum stratification plots (e.g. Figure 4.10) the distribution of power did not change much above  $\sim 500$  km despite the fact that the temperature (and hence, the cut-off period) is not constant throughout the photosphere and chromosphere. The power does often change as you look along the height axis for any given period value, but the most powerful periods themselves do not change. This suggested that the filtering process occurs only at the lower part of the atmosphere, at the minimum temperature. Additional evidence of this is seen when comparing the simulations of Set 2 with Set 1. The dominant period of waves in the Maltby chromosphere is almost the same as in the umbral atmosphere, despite the cut-off periods at the chromospheres being up to 100 seconds different. We then can say that only the minimum cut-off period that waves travel through matters in these simulations. This is perhaps obvious when one considers that if long-period disturbances are filtered out by the Lamb effect, even if the local cut-off period is higher at a higher altitude, the long-period signals are no

#### 4.4 Discussion

longer present. We could therefore expect to see different results if waves are excited locally at the chromosphere, as the waves will not have passed through the temperature minimum. This scenario is easy to imagine in the real observable solar atmosphere, as the energy from, say, a flare can provide a “kick” to the chromospheric material from above (Section 1.3.7).

In both the first and second sets of simulations we saw evidence of the changing cut-off period as magnetic field inclination increases. If the cut-off for the  $i = 0^\circ$  case is  $P_c = 220$  s then the theoretical cut-off period for the remaining values of  $i$  would be 227, 254, 311, and 440 seconds. The exact shape of the resulting spectra is complicated and is influenced by the specific driver frequencies which were applied, but in Figure 4.8 we can see power being shifted to higher values of period, despite not having definitive peaks at the exact theoretical cut-off value. For instance looking at the bottom two rows of Figure 4.8, both spectra have global peaks at just over  $P = 300$  s and minor peaks at around  $P = 800$  s, however there is more power at periods between 300–400 seconds in the case where  $i = 60^\circ$ . This result then gives weight to our proposition that the change to oscillatory behaviour in our observations was due to a change in the field inclination. However, we also must consider that the specific dominant frequencies present in the velocity driver seem to influence the resulting oscillations. The source of the velocity driver in the real solar atmosphere is convective motion underneath the surface which is a phenomenon which can vary with location.

An important feature of our results is the role of inclination angle for the amplitude of the waves travelling through the chromosphere. We see in, for example, Figures 4.8 and 4.9 that the waves in atmospheres with inclined fields have smaller amplitudes in  $v_y$ . We can refer to Figure 4.15 to see the individual velocity components and also the total velocity and velocity in the direction of the magnetic field. On inspection we see that the total wave velocity,  $v_{tot} = \sqrt{v_x^2 + v_y^2}$ , is reduced at a given height, although the  $v_x$  component increases, as the inclination angle increases, up to  $i = 45^\circ$ . At  $i = 60^\circ$  both the components of velocity decrease, which is possibly significant as this inclination angle is the only one we have studied where  $B_x > B_y$ . We would expect that the motion of waves at an angle against the inclined field would cause some perturbation to the magnetic field and therefore some energy loss in the velocity waves. On inspection of the magnetic field variation over time we find some variation in the  $B_x$  component, and no variation to  $B_y$ . These variations are very small, on the order of  $10^{-7}$  of the mean, but could account for this reduction in wave amplitudes. The variations in  $\mathbf{B}$  might be more pronounced in an atmosphere with a weaker field strength.

#### 4.4 Discussion

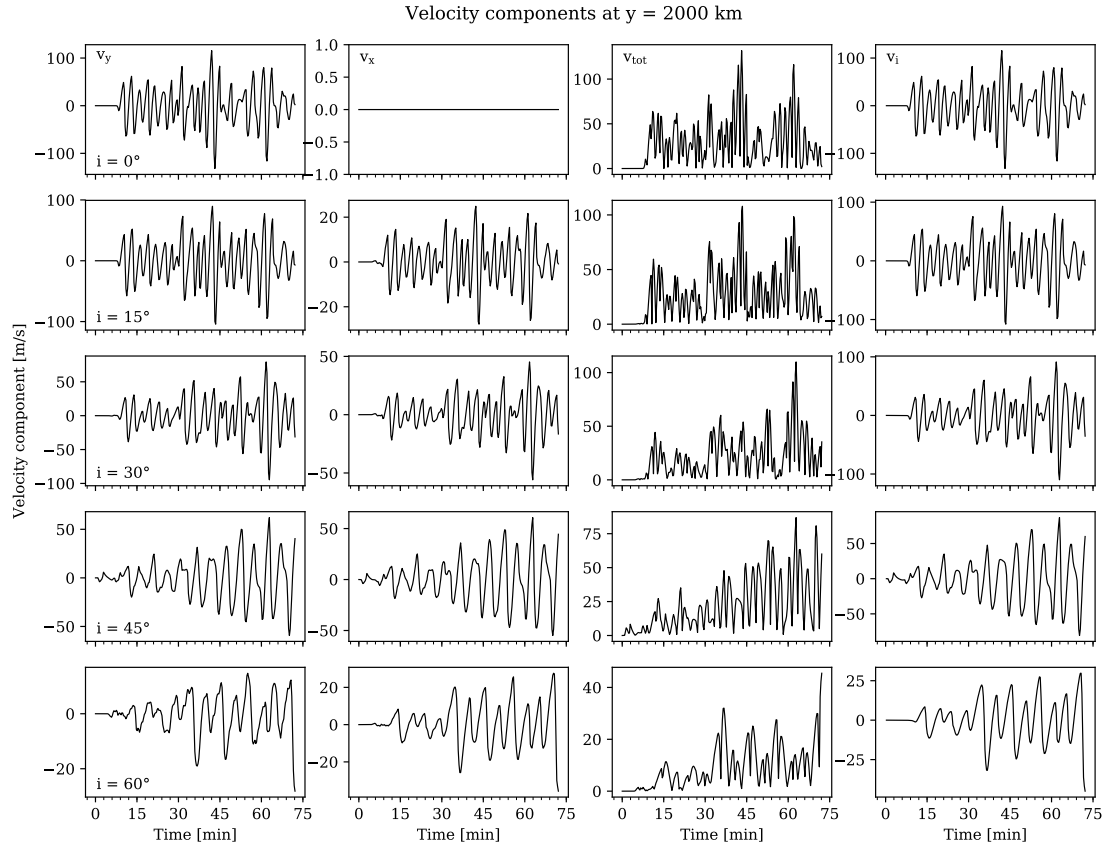


**Figure 4.15:** The various components of velocity at a fixed height of 2000 km across the five simulations in the first set. Each row shows a different field inclination and each column contains a different velocity component: y-velocity, x-velocity, total velocity, and velocity along the magnetic field inclination angle. The y-axes are varied but all are in units of m/s.

#### 4.4 Discussion

The theory of the chromospheric cavity accounts for field inclinations as a cause for an increase in the typical periods of waves. In the case of MAG waves the disturbances follow the magnetic field lines, meaning in an inclined field the length of the cavity gets extended by a factor of  $1/\cos i$ . The additional power at high periods seen in the first two sets of simulations could then be caused by a resonant cavity, rather than the cut-off period. We refer to the results of simulation Set 3 to investigate this. In this set, with different height scale factors, we see in Figure 4.14 that the dominant period of waves throughout the atmosphere does not appear to change as the scale factor changes. The spectrum peak remains at a period just over 200 seconds, just as in the  $i = 0^\circ$  simulations in the first and second sets. The main element that seems to be affected by the change of height scale is the reduction in power at certain periods (the previously mentioned dark band) which varies with height, clearly seen in the simulations of Set 2 (Figure 4.11) and in the first two simulations of the Set 3 (Figure 4.14). This effect appears to then be caused by something related to the cavity scale, such as waves reflected from the transition region. The dark band in power was not evident in the first set of simulations, which used the STiC umbral temperature profile. The fact that the (un-scaled) umbral profile does not produce this effect in a noticeable way is perhaps due to finer details of structure of the temperature profile. Using Figure 4.2 for reference, the differences in the umbral and Maltby profiles are subtle, but the Maltby has a more gradual temperature rise at  $y \approx 1000$  km and then a sharper increase at the start of the transition region, when compared to the STiC profile. In the third set of simulations, one thing to consider is the non-uniform grid scaling which was introduced to give greater resolution at chromospheric heights in the un-scaled atmosphere (Figure 4.1). In the scaled temperature profile simulations of Set 3, the temperature values were scaled but then applied to the same grid as the previous sets. Because the location of the chromosphere changes in the scaled versions, the higher resolution is lost in these simulations, which might affect the prevalence of, say, reflected waves.

The simulations of scaled temperature profiles in Set 3 is similar to the simulations of (Jess et al. 2020), who also used Lare2d. Their aim by varying the height scale was to probe the chromospheric cavity size towards the edges of a sunspot umbra, and the changes to the resulting spectra. The Set 3 results are consistent with the results of Jess et al. (2020), who do not report a change to the dominant period in their simulated upper-chromosphere velocity power spectra, but a secondary peak in the high-frequency range. The value of the slope of the spectrum in the high-frequency region of their results was linked to the length of the cavity. In our Set 3 results we can see a change to the shape of the power spectra in the low-period regime (high-frequency) which was caused by changing the cavity length. It

#### 4.5 Conclusion

is possible that the results are reflective of each other, though our height-resolved spectra reveal that the shapes of the low-period spectra can differ as we move through the same oscillating atmosphere. The fact that our Set 1 simulations did not return changes to the low-period spectra is at odds with the idea presented in Section 1.3.3, that the geometrical cavity length can cause changes to the dominant observed oscillation periods.

There is much to consider when comparing these simulations to observations of the solar atmosphere. To begin with, the simulations are in two dimensions, which limits the scope of processes such as wave coupling. For the sake of simplicity the simulations were set up with uniform magnetic fields, which is of course very different from the “chromospheric canopy”, the spreading out of the magnetic field in the upper chromosphere to essentially horizontal. In the case of a canopy, the cut-off period would increase locally as the inclination increased and also due to the increasing temperature of the chromosphere with height. Comparing to our results, a canopy shape might not change the results significantly, as we saw that only the minimum value of the cut-off period was important when considering waves which originate at or below the solar surface. What would likely be more influential is the magnetic field itself in terms of the guiding of waves, in cases where the inclination goes beyond the scope of our simulated scenarios. The chromosphere is an extremely complex environment and there are many physical processes which were not considered in these simulations such as radiative losses and thermal conduction. While the Lare code has the capability for these built in, we elected to keep our simulations as simple as possible to focus on particular effects. The magnetic field was also static in time, meaning that the effect of, say, a magnetic reconfiguration due to reconnection could not be recreated within the same simulation. These represent a few of the possibilities for further research which could be pursued in the future.

## 4.5 Conclusion

We set out to investigate the results from our observations and test our interpretation that a change to the magnetic field could cause a significant increase to the oscillations seen over a sunspot. We observe that only the minimum value of the cut-off period in the atmosphere is relevant, and this usually occurs at the temperature minimum, which is unlikely to be affected during a solar flare (though heating by a few hundred K in very strong flares is possible). Changing the length of the chromospheric cavity had no effect on the most dominant period, however it did alter the overall shape of the spectrum in the  $P < P_c$  regime. From the various parameters which we altered, the most significant

#### *4.5 Conclusion*

change to the dominant periods seen at the chromosphere was in simulations which used different magnetic field inclinations. We note that the source of the chromospheric waves is significant, as disturbances originating from higher in the atmosphere can propagate at longer periods due to higher local temperatures. Overall, the investigations using Lare simulations support our interpretation of the results which we presented in Chapter 3.

---

# 5

---

## Oscillations in a small flaring active region

In this chapter we present analysis of a second dataset from the CRISP instrument, captured on the 13<sup>th</sup> of June 2013. The observations feature an active region which underwent two B-class flares in quick succession. We used the spectral fitting technique (Section 2.2.6) on intensity timeseries, similar to the analysis in Chapter 3. We sought to investigate the oscillatory signals which were present before and after the flare events, and make comparisons to the results from the M1 flare presented in Chapter 3. These two flares are much less powerful than the previous study, and the sunspots within this active region are smaller and more numerous.

We extended our analysis to also include velocity oscillations, which were calculated across the field of view, and utilised the inversion code STiC in our investigation of the results. We also made use of Milne-Eddington inversions of a photospheric line, and the weak-field approximation (Section 2.3.2) on a chromospheric line, to study the magnetic field.

The flares and CRISP dataset are detailed in Section 5.1, before describing the intensity and velocity analyses in Section 5.2. The results are presented in Sections 5.3 and 5.4. We investigate the evolution of the atmosphere in Section 5.5 and Section 5.6. We discuss the results in Section 5.7 and conclude in Section 5.8.

### 5.1 Description of flare events and dataset

The dataset from CRISP contains measurements of two spectral lines: Ca II 8542 Å sampled over  $\pm 0.5$  Å in 0.1 Å steps with one additional continuum-like wavelength point at +2.0 Å; and Fe I 5250 Å covering  $-0.2$  Å/+0.24 Å in 0.04 Å steps. These sample the chromosphere and photosphere, respectively, with full Stokes polarimetry. The CRISP image scale was

### 5.1 Description of flare events and dataset

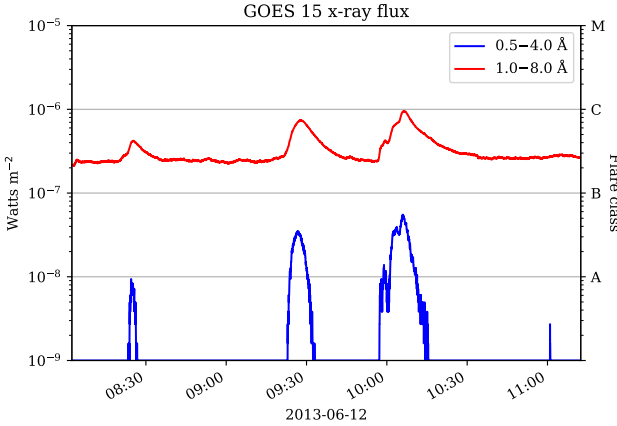


**Figure 5.1:** X-ray flux in two wavelength bands measured by the GOES-15 spacecraft during the time of the CRISP observation. Only the two flares at  $\sim$ 09:20 and  $\sim$ 09:55 occur within the target active region. The corresponding flare class is shown on the right axis.

0.0586" per pixel, and the cadence was  $\Delta t = 30.7$  s. The dataset begins at 8:21 and finishes at 11:00 UTC on 2013-06-13 and is centred on active region NOAA 11768, which was near the disc centre with  $\mu = 0.915$ . The two flares occurred at 09:20 and 09:55, and were of GOES class B7.2 and B9.3, respectively. The GOES timeline for the duration of this observation is shown in Figure 5.1. Figure 5.2 shows Ca II 8542 Å images of the active region from the beginning of the dataset, and also at the times of the flares. The images are aligned such that solar North is pointing upwards, and the field of view shifts and rotates keeping static features fixed in the same pixels. We can see that the active region had already developed the bright structure lying across the middle of the images before the observation began. Note that in this chapter, all of the observations are from the CRISP dataset, and so the spatial axes of all figures are given as the original pixel values, or as the macropixel value in Section 5.3.1 where the scales are simply the original pixel values divided by ten. The first flare caused brightening mostly close to the centre of the field of view, seen in the central panel of Figure 5.2, while the second flare ignited the long ribbon which extends along the middle of the images, and is connected at the sunspot group to the right of the images. We can see in the context images that there is a great deal of complexity in the region connecting the bright points at the left and centre, featuring a dark filament structure. Appearing as a dark curve on the images, it appears to be an absorption feature lying above the brightening region below. The filament moves around a lot during the flare activity, and could also be part of the magnetic connection between the footpoints, as brightening is seen following its shape in SDO/AIA context imaging, seen in Figure 5.3. In this figure, the first three panels closely match the times of the panels from Figure 5.2,

### 5.1 Description of flare events and dataset

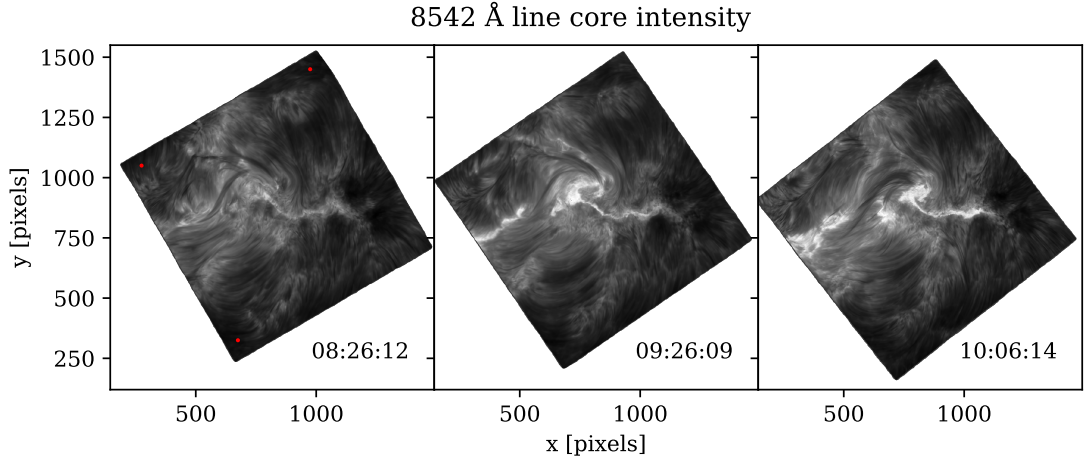


**Figure 5.2:** Images intensity integrated over the Ca II 8542 Å line core taken from the start of the dataset and during the times of the two flares. The colour scale is equal across all images. The red points in the left panel indicate areas of “quiet” Sun, which were used for calibration purposes in Section 5.6.

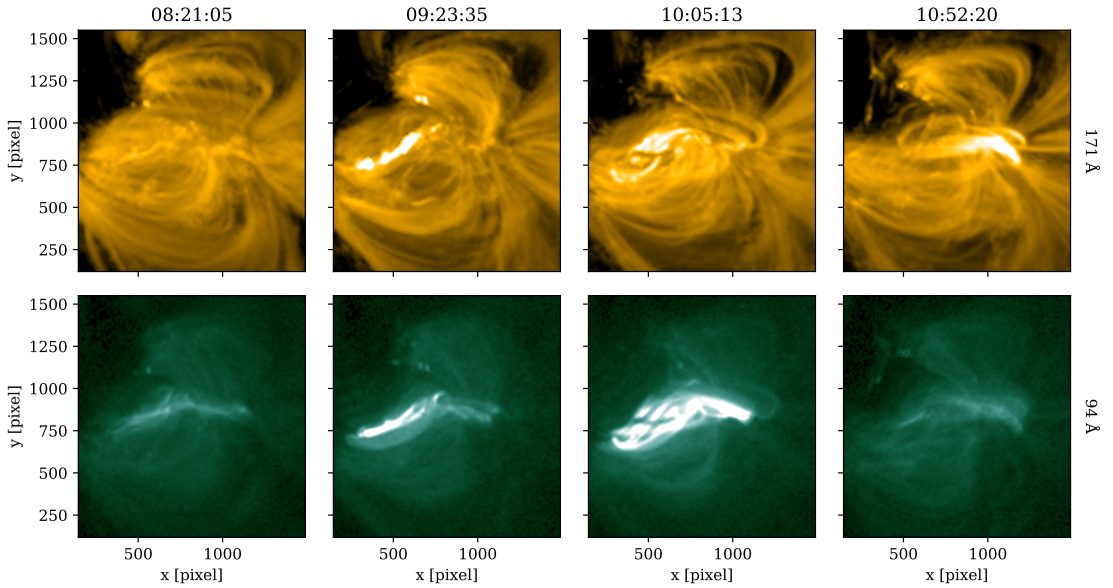


**Figure 5.3:** Images from the 171 Å and 94 Å channels of SDO/AIA, spanning the length of the CRISP dataset and covering the same field of view. All subfigures from each channel have equal colour scales.

### 5.1 Description of flare events and dataset

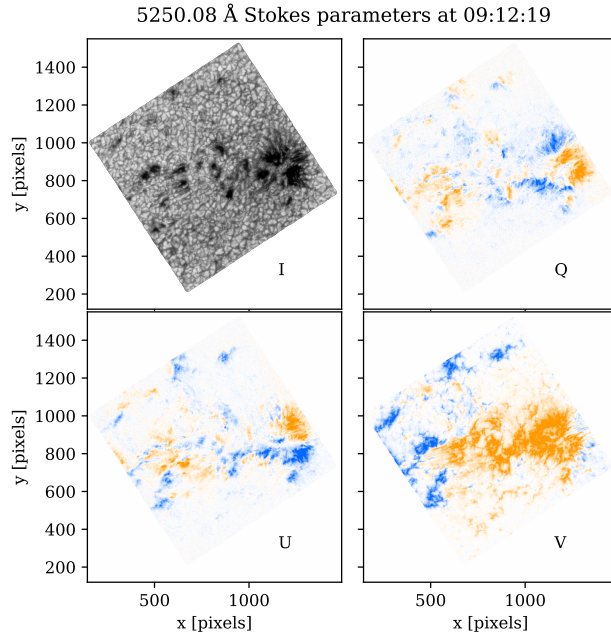


**Figure 5.4:** Maps of the Stokes parameters at a single wavelength value,  $+0.08 \text{ \AA}$  from the core of Fe I 5250  $\text{\AA}$ . The *Q*, *U*, and *V* panels are displayed on diverging colour scales with positive values in blue, and negative in orange. All colour scales were chosen for best contrast, have units of data number, and have ranges which vary across the four subfigures, although the *Q* and *U* scales are identical.

and there is an additional fourth panel showing the region just before the end of the CRISP observation. The fourth panel shows the evolution of a bright loop above the sunspots in the right of the field, which is visible in the 171  $\text{\AA}$  channel, but not in the 94  $\text{\AA}$  channel. This is above the location of the bright flare ribbon, on which we will focus our analysis in section 5.4.

Maps of the Stokes parameters from Fe I 5250  $\text{\AA}$  taken from the beginning of the dataset are found in Figure 5.4. From the *I* image we can see the structure of the photosphere under this active region, showing granulation smattered with many magnetic pores in the centre of the field of view, with more substantial sunspots occupying the right side of the image. The sunspots are rather small, with very little penumbral structures visible in this image. We can see how the polarimetric parameters (*Q*, *U*, and *V*) vary throughout the field of view, with most of the signal being seen at location of the magnetic activity. In contrast to this, Figure 5.5 is an equivalent plot for Ca II 8542  $\text{\AA}$  and shows strong signal only in the *V* component. The *Q* and *U* signal in the calcium line is almost noise-like over the majority of the field of view, except for over the larger sunspots to the right. We can

## 5.1 Description of flare events and dataset

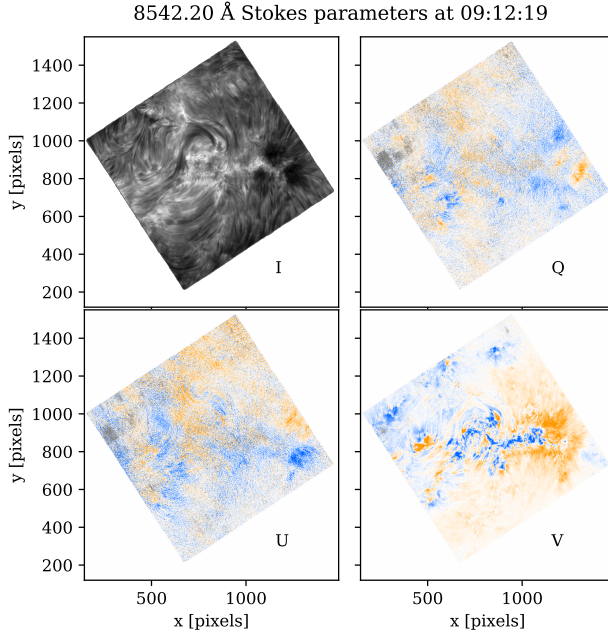


**Figure 5.5:** Similar to Figure 5.4 but for Ca II 8542 Å.

even see some instrumental artefacts in the  $Q$  and  $U$ , meaning that these elements of the dataset are on the whole not appropriate for use in any calculations of the magnetic field (through the weak-field approximation or using inversions), however we can use the  $V$  component to identify line-of-sight magnetic fields.

### 5.1.1 Reference points

Throughout this chapter, we will refer to locations of interesting results, mostly in relation to the location of sunspots in the field of view. We refer to the sunspots of interest as sunspots A, B, C, and D which are identified in Figure 5.6, and will be referred to collectively as the “named sunspots”. The figure also shows the sets of pixels which were inverted using STiC: one 2D patch and one line of pixels in the flare ribbon used for timeseries (see Section 5.6).

## 5.2 Analyses

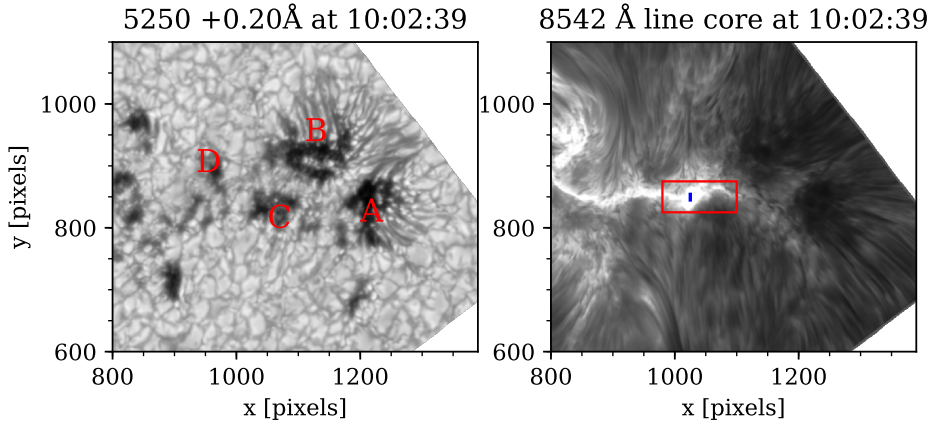


**Figure 5.6:** Left: Fe I 5250 Å image labelled with the named sunspots for reference throughout the chapter. Right: Ca II 8542 Å core image showing the 2D patch and line of pixels used in STiC inversions.

## 5.2 Analyses

In order for direct comparisons to be made to the results of Chapter 3, we searched for signs of oscillatory signals in this dataset by first re-binning the dataset into “macropixels”. The dimensions of the data were reduced by a factor of 10, after clipping the edges. Stokes  $I$  timeseries were then drawn from individual wavelength points in every macropixel which was present at all times throughout the observation, from two separate time intervals; the first  $\sim$ 55 minutes of the observation (“pre-flares”) and the last  $\sim$ 55 minutes (“post-flares”). This contrasts with the Chapter 3 analysis, which used 30-minute time intervals. The current dataset has the advantage of a much longer length of observation after the flares, so we sought to maximize the post-flares interval, especially considering the pre-flares observations were of a similar length. This extended the limits of the Fourier power spectra we analysed, allowing periods up to  $\sim$ 55 minutes to be studied. The cadence of  $\Delta t = 30.7$  s is much longer than for the 2014-09-06 dataset, an unfortunate consequence of fully polarimetric observations. The range of the period space covered by the spectra is  $\sim$ 1–55 min, which is still suitable for finding oscillations on timescales of a few minutes.

Each of the suitable macropixels had timeseries drawn over the pre-flares and post-flares intervals, with each wavelength point taken separately. The spectral fitting process was then carried out at full resolution for the Ca II 8542 Å data. To improve the signal, the spectral range was divided into five sections; line core, near blue/red and far blue/red. Each timeseries was analysed using the spectral fitting method (Section 2.2.6) using a

## 5.2 Analyses

significance level of 99.9%, equivalent to the analysis in Chapter 3. Examples of timeseries which resulted in each of the three chosen models (M1, red noise; M2, Gaussian bump; and M3, kappa function) can be seen in Figure 5.2.

### 5.2.1 Velocity measurement

The velocity in the chromosphere was measured by identifying Doppler shifts to the line core of Ca II 8542 Å. The Ca II 8542 Å line was sampled over a rather small wavelength range at  $\pm 0.5$  Å, meaning the maximum shift we could possibly measure is

$$v_{los} = c \frac{\Delta\lambda}{\lambda_0} = 3 \times 10^5 \times \frac{\pm 0.5}{8542} = \pm 17.5 \text{ km s}^{-1}. \quad (5.40)$$

In the above,  $v_{los}$  is the line-of-sight velocity,  $c$  the speed of light, and  $\Delta\lambda$  is the maximum deviation from the central wavelength  $\lambda_0$ . Flares have been observed to cause velocity flows of the order of 10s of kilometres per second in chromospheric lines (e.g. [Milligan & Dennis 2009](#)). Though 17 km s<sup>-1</sup> is the upper limit of the flows we could observe with this Ca II 8542 Å dataset, flows above  $\sim 7$  km s<sup>-1</sup> would be difficult to ascertain with much confidence, because we do not want to fit too close to the edges of our spectral range. We assume that the typical Doppler shifts will be contained in the available spectral window due to these flares being fairly small, although velocity signals up to 17 km s<sup>-1</sup> have been detected in small flares before ([Keys et al. 2011](#)).

The velocity measurement works on a pixel-by-pixel basis, and moves through each timestep in order, determining the wavelength shift of the line core. The first attempt is made by doing a simple second-order polynomial fit over the middle section of the spectral line out to  $\pm 0.2$  Å (fitted over five spectral points). This is not computationally expensive and allows determination of the line peak with accuracy greater than the wavelength scale. The quadratic function is deemed not to be well-fitted if the sum of the squared residuals ( $\chi^2$  value) is above  $2 \times 10^{-3}$ , or if the peak was determined to be outwith the  $\pm 0.2$  Å range.

If the first quadratic fit is not successful, a second is attempted, again using five spectral points. The wavelength points used for the second fit are chosen based on the turning points of the line profile, in an effort to pick up strong peaks further from the central wavelength. The centre of the fit is set at the turning point which is closest to the previously determined value for the line shift. If the second fit attempt also fails, then the process is

## 5.2 Analyses

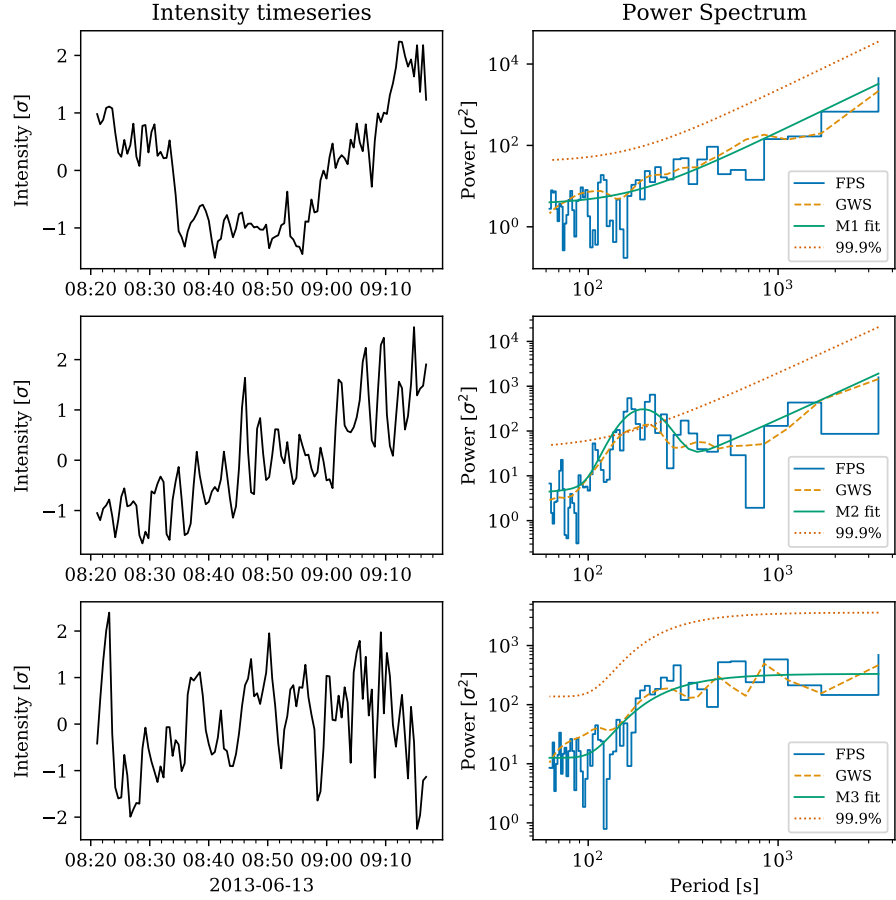


**Figure 5.7:** Timeseries (left column) and their respective Fourier power spectra (right column) from Ca II 8542 Å data, showing examples of each of the three available models. Top row: Ca II 8542 Å core timeseries from quiet Sun, which was classified as fitting M1 (red-noise background). Middle row: Ca II 8542 Å +0.1 Å timeseries from the sunspot umbra, fit with M2 (Gaussian bump). Bottom row: Ca II 8542 Å core timeseries from the edge of the active region, classified as M3 (kappa function). The right-hand panels contain the FPS (blue stepped line), the global wavelet spectrum (yellow dashed line), the mean spectrum fit (green line), and the 99.9% significance level (orange dotted line).

## 5.2 Analyses

stopped and the wavelength shift at that timestep is set to the same value as the previous timestep.

Some of the spectral lines in this dataset are challenging for the purposes of the determination of Doppler shifts. A Gaussian absorption or emission feature is the best candidate for the velocity measurements, which are seen in the majority of pixels over the sunspots (absorption) and at the areas of flare brightening (strong emission) along the ribbon. We also observe many lines with strong central reversals, and Gaussian peaks shifted quite far towards the edges of the spectral window. However, in the region near the filament the lines are erratic. This could be for a variety of reasons; extremely complex radiative transfer as light passes through the cooler plasma high in the atmosphere, very large wavelength shifts of spectral features, or instrumental effects.

Wavelength shifts were converted to line-of-sight velocities via equation 5.40. Velocity timeseries were extracted over the same pre-flares and post-flares time intervals as the intensity timeseries, and were similarly analysed using the spectral fitting method with a 99.9% significance level enforced, and are discussed in Section 5.4. Because of the large number of unsuccessful velocity measurements over the complex area surrounding the filament, the results presented in Section 5.4 are focussed on the area surrounding the flare ribbon and the group of named sunspots in the right of the field of view.

### 5.3 Intensity oscillations

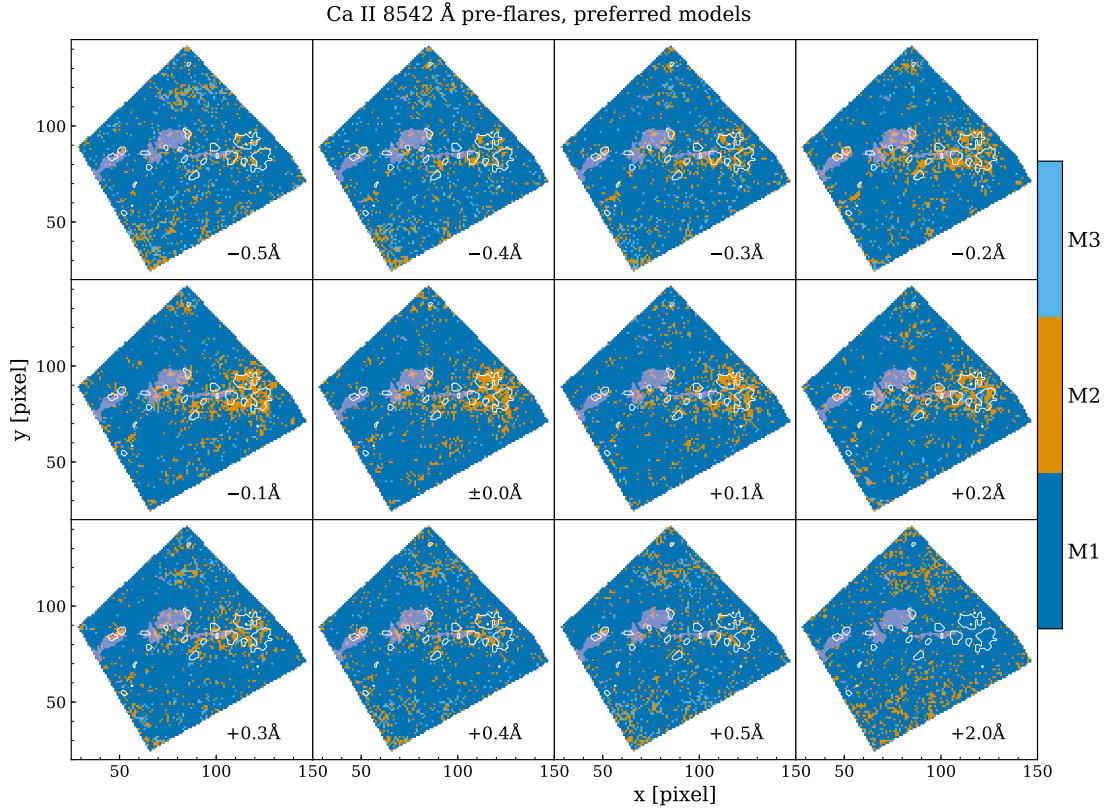


**Figure 5.8:** The preferred spectrum model for each macropixel of Ca II 8542 Å intensity in the pre-flares interval, is displayed by the colour scale. The outlines of the sunspots are shown by the contour lines, determined by 50% of the maximum intensity of the linecore of Fe I 5250 Å. The locations of flaring macropixels is shown by the filled contours, and have been determined by the maximum brightness of each macropixel. Every panel represents a different wavelength offset from the line core, which is denoted in the lower right of each.

## 5.3 Intensity oscillations

### 5.3.1 Reduced resolution results

#### Preferred models

Figures 5.8 and 5.9 show the preferred model across the field of view for the reduced resolution data from Ca II 8542 Å, in the pre-flares and post-flares time intervals. Every wavelength step is displayed, including the continuum point located at 8542 + 2 Å. Also shown are the locations of the underlying sunspots, with contour lines at 40% of the Fe I 5250 Å line core intensity, and the locations which experienced the most intense flare

### 5.3 Intensity oscillations

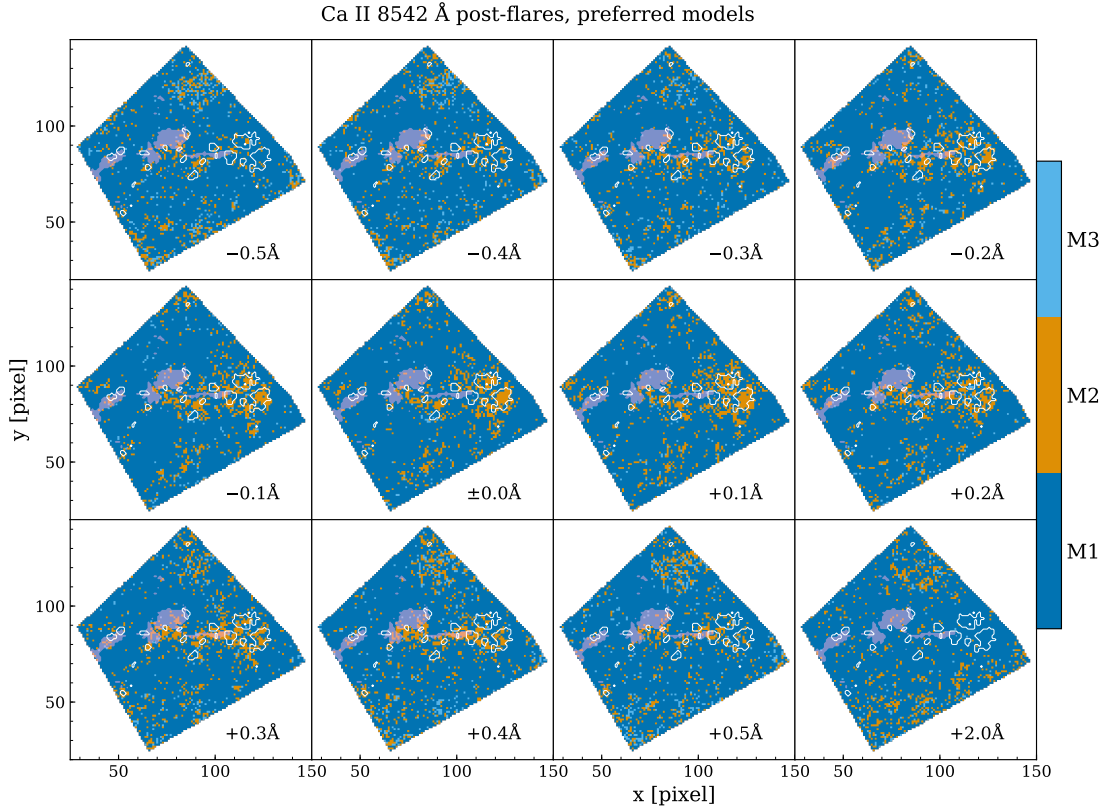


**Figure 5.9:** Similar to Figure 5.8 but for the post-flares interval, in the reduced-resolution Ca II 8542 Å intensity data.

heating, shown by filled contours. In these figures we can see that the most common result was the red noise background model, which is expected and matches the results of Section 3.3.1. There is a relatively small number of macropixels where the kappa model was preferred. They are widely strewn across the field of view, and are more common in towards the wings of the Ca II 8542 Å line. Kappa-model macropixels seem to have slightly higher concentrations towards the outsides of the field of view, away from the most magnetically active part.

There is a significant number of macropixels which favour the Gaussian bump model, and these are mostly concentrated around the magnetically active area which stretches across the centre of the field. They are more prevalent in line core data, with their concentration falling as the wavelength moves away from the core. At + 2.0 Å there are almost no clear oscillations above the background detected in the belt of sunspots.

We see from comparing Figures 5.8 and 5.9 that there are some differences between the

### 5.3 Intensity oscillations

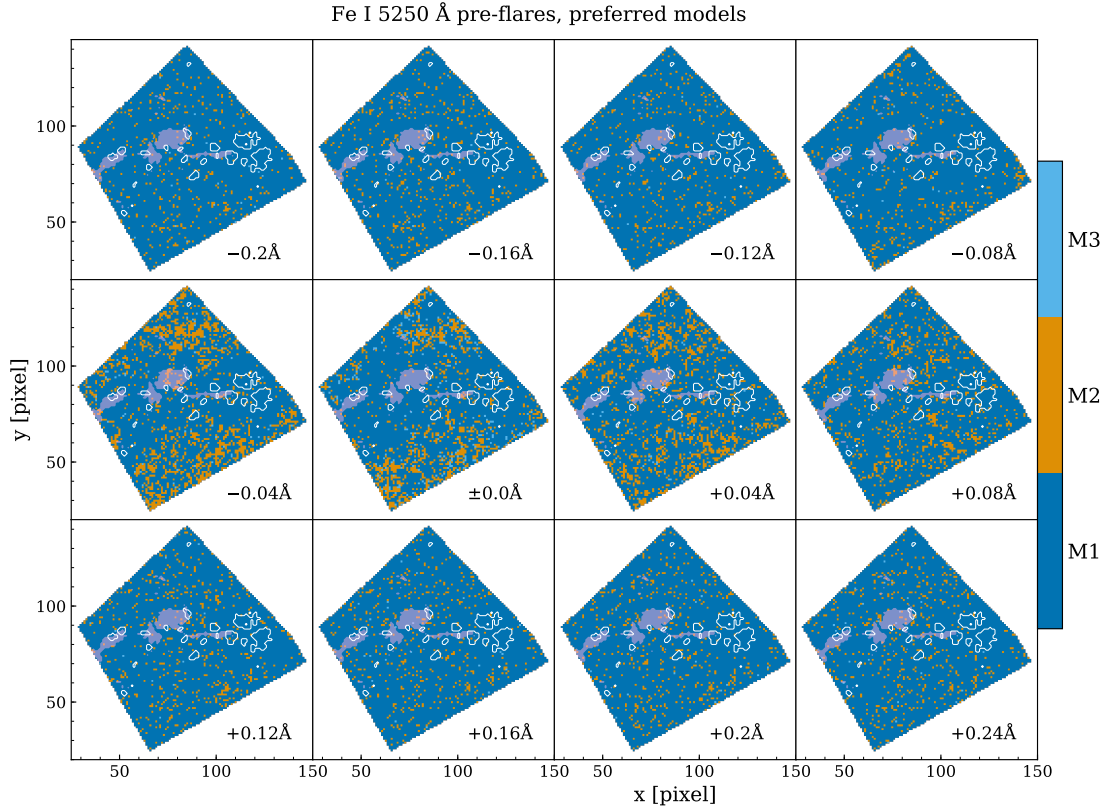


**Figure 5.10:** Similar to Figure 5.8 but showing the preferred models for the pre-flares interval in reduced-resolution Fe I 5250 Å intensity timeseries.

pre-flares and post-flares results. Over the named sunspots to the right of the field of view there is a much larger area of oscillatory behaviour in the pre-flares interval, with the extent of the signals being reduced after the flares. For example, in pre-flares line core results over sunspot B, the region of M2 fits is approximately 150 pixels across, while in the post-flares data it is approximately half as wide, hence the area was reduced by four times. The sunspot umbrae have predominantly oscillatory signals in both time intervals, but in the penumbra these are lost after the flares. At wavelength points surrounding the core, there are oscillatory signals covering the long trail of sunspots in a thick band in the pre-flare results, but in the post-flares interval there is a lack of oscillatory signals at the location of the long flare-heated ribbon situated at  $y = 85$  which stretches from  $x = 80$  to  $x = 110$ . However, at the flare ribbon there is a concentration of oscillatory signals in the wavelength steps from  $+0.2\text{--}0.4\text{\AA}$ . We do not see the same high concentration in the equivalent plots on the blue side of the spectral line. Equivalent plots for the Fe I 5250 Å line are found in Figures 5.10 and 5.11. Again we see that the red noise background is the

### 5.3 Intensity oscillations

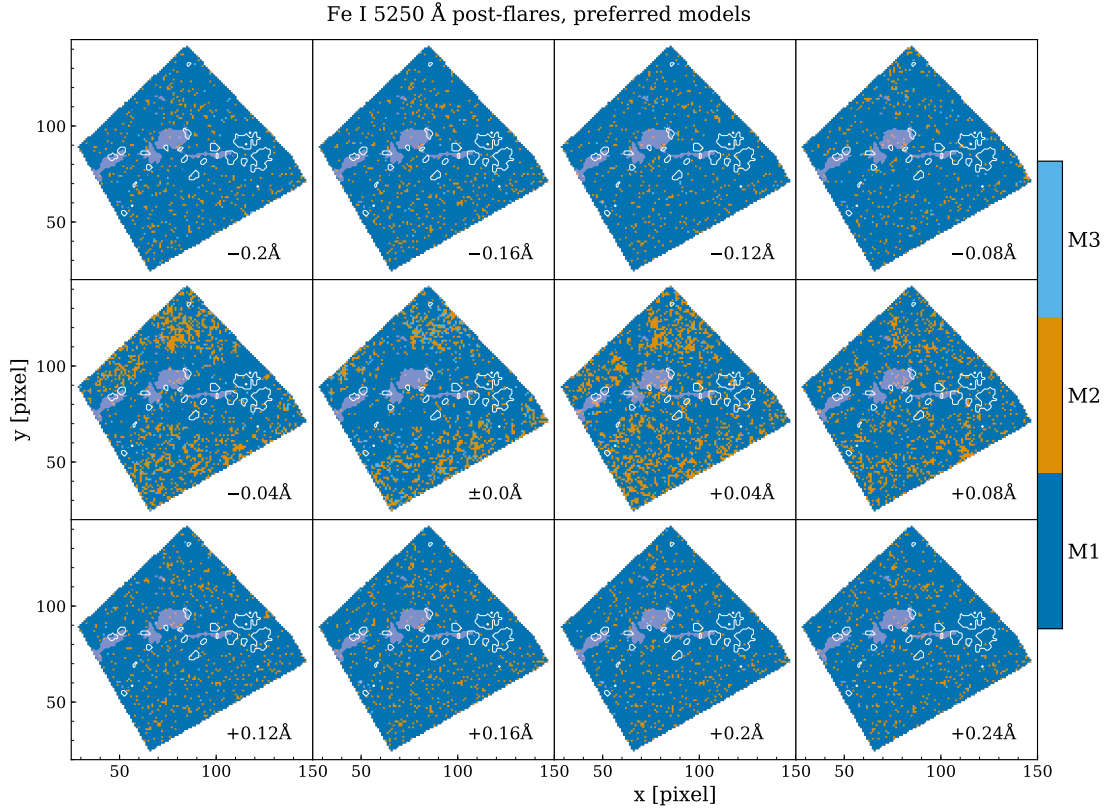


**Figure 5.11:** Similar to Figure 5.8 but for the post-flares interval in reduced-resolution Fe I 5250 Å intensity timeseries.

most common result for all the wavelength values. In contrast to the Ca II 8542 Å results the location of the prevalent oscillatory signals at wavelengths close to the line core is in the “quiet” area surrounding the sunspots (refer to Figure 5.4 for context). There is little evidence for oscillatory signals in the central band of high magnetic field. At the wings of this line there are very few oscillatory signals, with no structure to be seen over the field of view. Comparing pre- and post-flares, there is little difference for the preferred models from Fe I 5250 Å data. This does not necessarily mean that the photosphere was unaffected by the flares, rather that the oscillatory signals remained approximately the same.

#### Gaussian bump peaks

The periods corresponding to peaks of the Gaussian bumps in the M2 spectra are shown in Figures 5.12 and 5.13 for Ca II 8542 Å pre- and post-flares results. At the group of named

### 5.3 Intensity oscillations

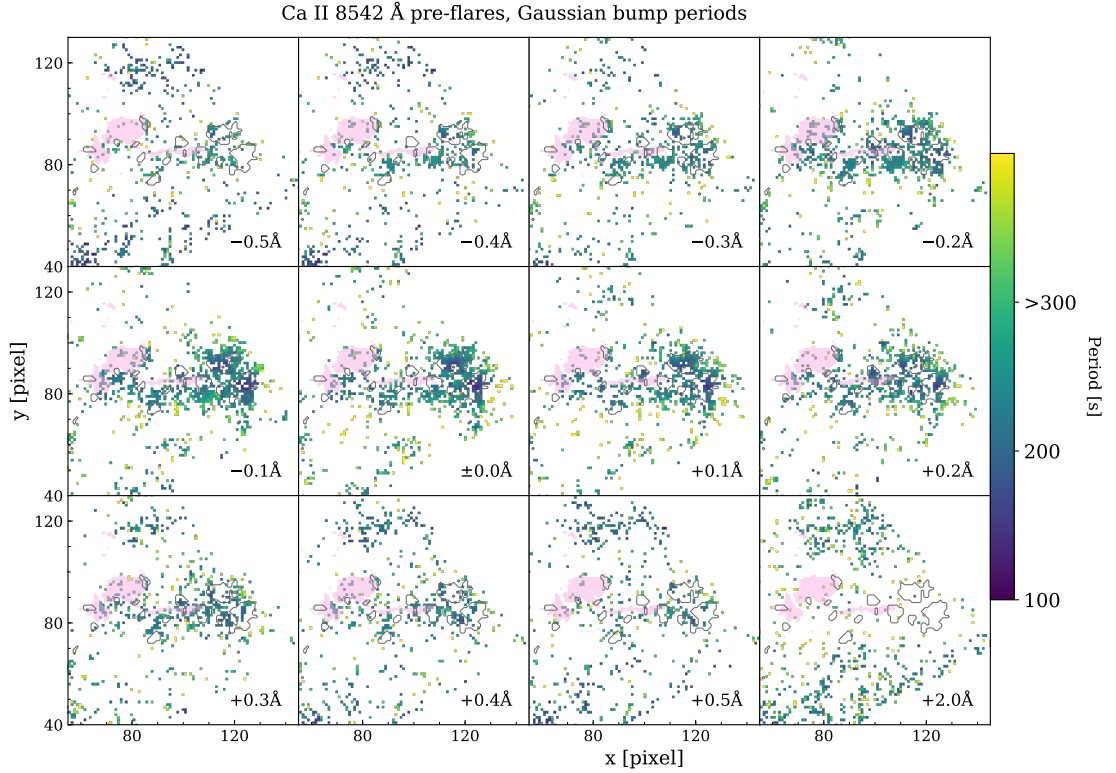


**Figure 5.12:** The periods at the Gaussian bump peaks for each macropixel of Ca II 8542 Å in the pre-flares interval, where the Gaussian bump (M2) was the preferred model for the spectrum. The outlines of the sunspots are shown by the contour lines—determined by 50% of the maximum intensity of the linecore of Fe I 5250 Å. The plots cover a different span than in Figures 5.8–5.11, in order to focus on the group of sunspots with its high concentration of M2 model macropixels. The locations of flaring macropixels is shown by the filled contours, and have been determined by the maximum brightness of each macropixel. Every panel represents a different wavelength offset from the line core, which is denoted in the lower right of each. The colour scale is cut off at 300 seconds.

sunspots the signals show the characteristic increase in period with distance from the centre of the sunspot umbrae, introduced in Section 1.3.3 and observed in the results of Section 3.3.2. We see that the periods range from approximately 150–200 seconds in the sunspot centres to over 300 seconds at the penumbrae. Near the line core, the region surrounding the penumbra shows periods tending to longer values still at 400 seconds or above. This contrasts with behaviour in the wings, which has far fewer M2 spectra, but where there are signals they are at much shorter periods (100–200 seconds) than at the line core. For the oscillations along the belt of trailing sunspots the periods vary between 200–300 seconds, and this is the case for the signals at line-wing wavelengths also.

### 5.3 Intensity oscillations

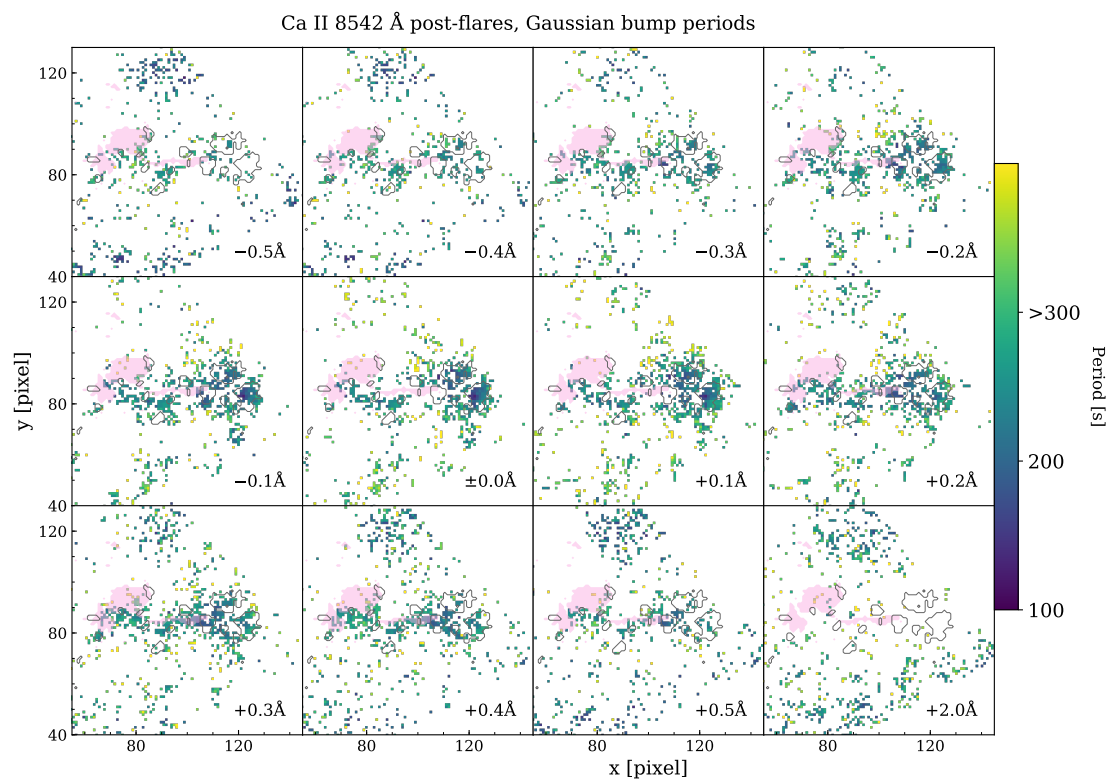


**Figure 5.13:** Similar to Figure 5.12 but for the post-flares interval in reduced-resolution Ca II 8542 Å.

### 5.3 Intensity oscillations

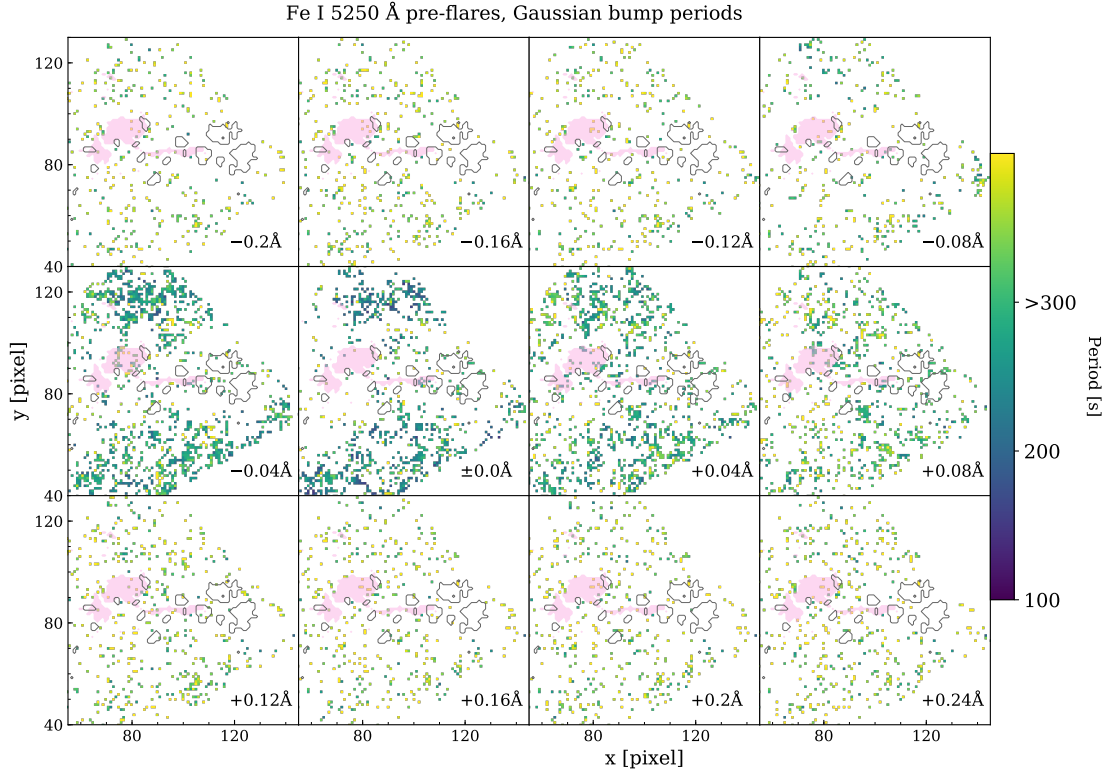


**Figure 5.14:** Similar to Figure 5.12 but for the pre-flares interval for reduced-resolution Fe I 5250 Å.

There is not a great deal of difference seen between the Gaussian bump peaks seen in pre-flares and post-flares data, as the locations of M2 preferred models are not often the same. However, at the Ca II 8542 Å core one can see some changes in the signals lying over the named sunspots. The  $-0.1\text{ \AA}$ ,  $+0.1\text{ \AA}$ , and line core panels displays longer periods in the post-flares interval (Figure 5.13) than in the pre-flares (Figure 5.12) over sunspot A. It appears as though the longer period penumbral signals have been shifted to more centrally above the sunspot umbra.

In the equivalent figures for Fe I 5250 Å (Figures 5.14 and 5.15) we see that the periodicities of the signals covering the quiet area surrounding the sunspot group are mostly in the range 250–350 seconds, although in the line core data the periods are slightly lower at  $\sim 200$  seconds. The typical periods remain almost constant when comparing the pre- and post-flare intervals, suggesting that the flares have little effect on the part of the atmosphere sampled by this line.

### 5.3 Intensity oscillations

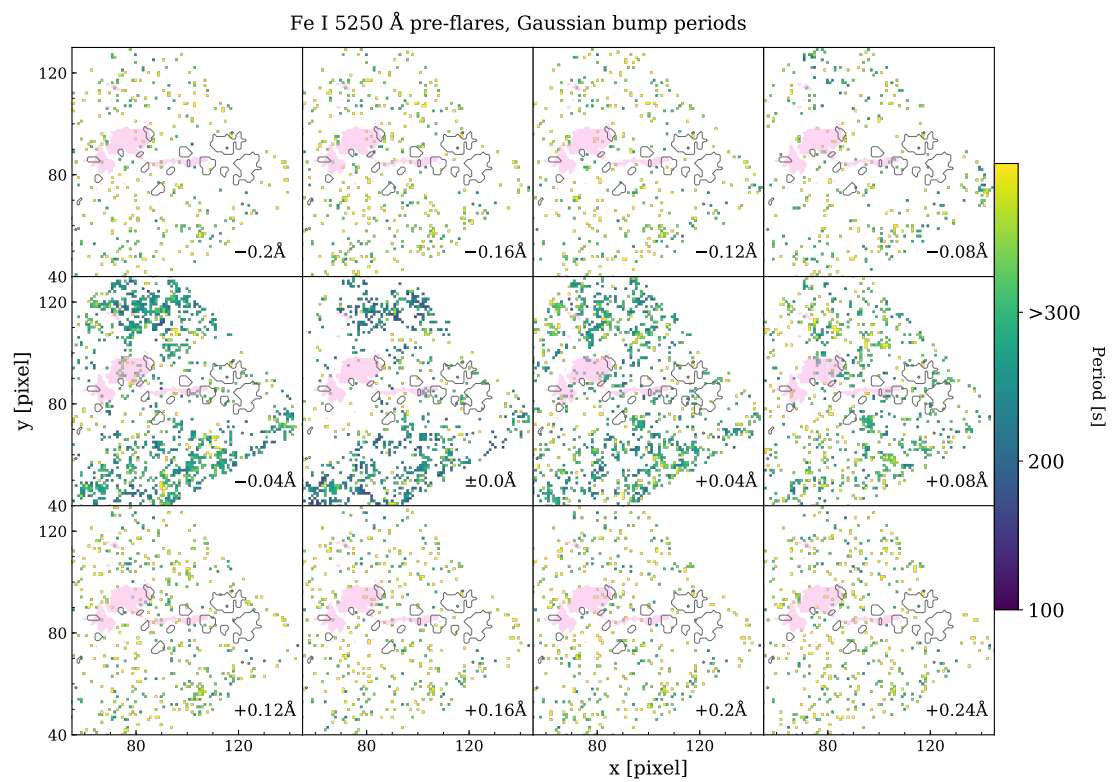


**Figure 5.15:** Similar to Figure 5.12 but for the post-flares interval for reduced-resolution Fe I 5250 Å.

### 5.3.2 Intensity oscillations at full resolution

The preferred models for full resolution Ca II 8542 Å are shown in Figures 5.16 and 5.17, and the locations of the Gaussian bump peaks are in Figures 5.18 and 5.19. In these images we can see a lot more fine structure, in particular in the oscillatory signals which are present at the sunspot penumbrae. Again we see that there is a lack of oscillatory signals at the locations of the thin flare ribbon in the line core, while the near-red and far-red parts of the line show some periodicity. In the two red panels of Figure 5.17 there is a blob of signal over sunspot C, where the thin ribbon meets the spot group. There is some concentration of oscillatory signal within the lower half of this sunspot's umbra (outlined by the contour) visible in the blue sections and core of the line in the pre-flares data, but in the post-flares interval the concentration is not found, while in both the near and far red of the line, there is some signal at this location in pre- and post-flares intervals but is more concentrated in the post-flares data. The patch of concentrated signals in post-flares data covers almost the entire sunspot C umbra at approximately 50 pixels across.

In the full resolution Gaussian bump results it is clear to see the very low period signals ( $P \approx 100$  s) which are found at the centres of sunspots A and B in the line core data and (not quite as prominently) in the near-blue and near-red wavelengths. We can also see more clearly the signals which appear to be in flaring pixels in the near-red and far-red wavelengths, above sunspot C. The periods of these intensity oscillations appear to be fairly low at  $\sim 200$  seconds. There are signals in the post-flares near blue at approximately the same location which appear to match this periodicity. As stated above, in the pre-flares interval there are concentrations of signals at locations near to these oscillations at the flaring pixels. However, from Figure 5.18 we can see that the signals in the pre-flares data are at significantly higher periods than those at the flare ribbon.

## 5.4 Velocity oscillations

The spectral fitting technique was then applied to the velocity timeseries from each pixel, and the resulting preferred models and Gaussian bump results are shown in Figure 5.20. This figure contains both the pre- and post-flares data and the spatial limits were chosen to focus on the magnetically active area including the flare ribbon and the large cluster of named sunspots. This avoids the very complex region on the left of the CRISP field of view which for much of the observation contained very complex line profiles probably due to the moving filament and hence, assigning a single velocity value would not be

### 5.4 Velocity oscillations

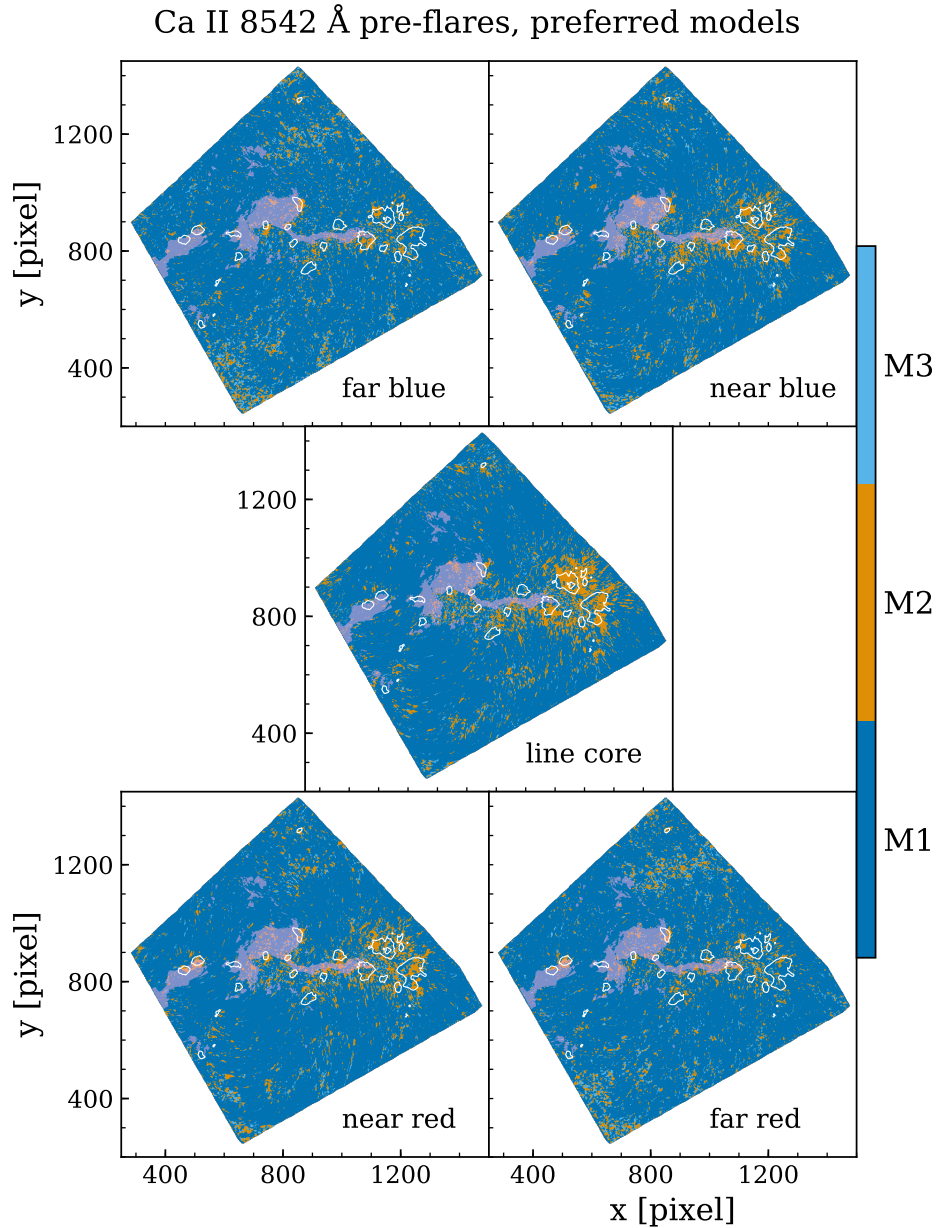


**Figure 5.16:** The preferred spectrum model for each pixel of Ca II 8542 Å in the pre-flares interval, at full resolution. The underlying sunspots are shown by the solid contour lines—determined by 40% of the maximum intensity of the line core of Fe I 5250 Å. The locations of flaring pixels are shown by the filled contours, and have been determined by the maximum brightness of each pixel. The labels in the lower right of each panel show the part of the spectral line they are drawn from.

#### 5.4 Velocity oscillations

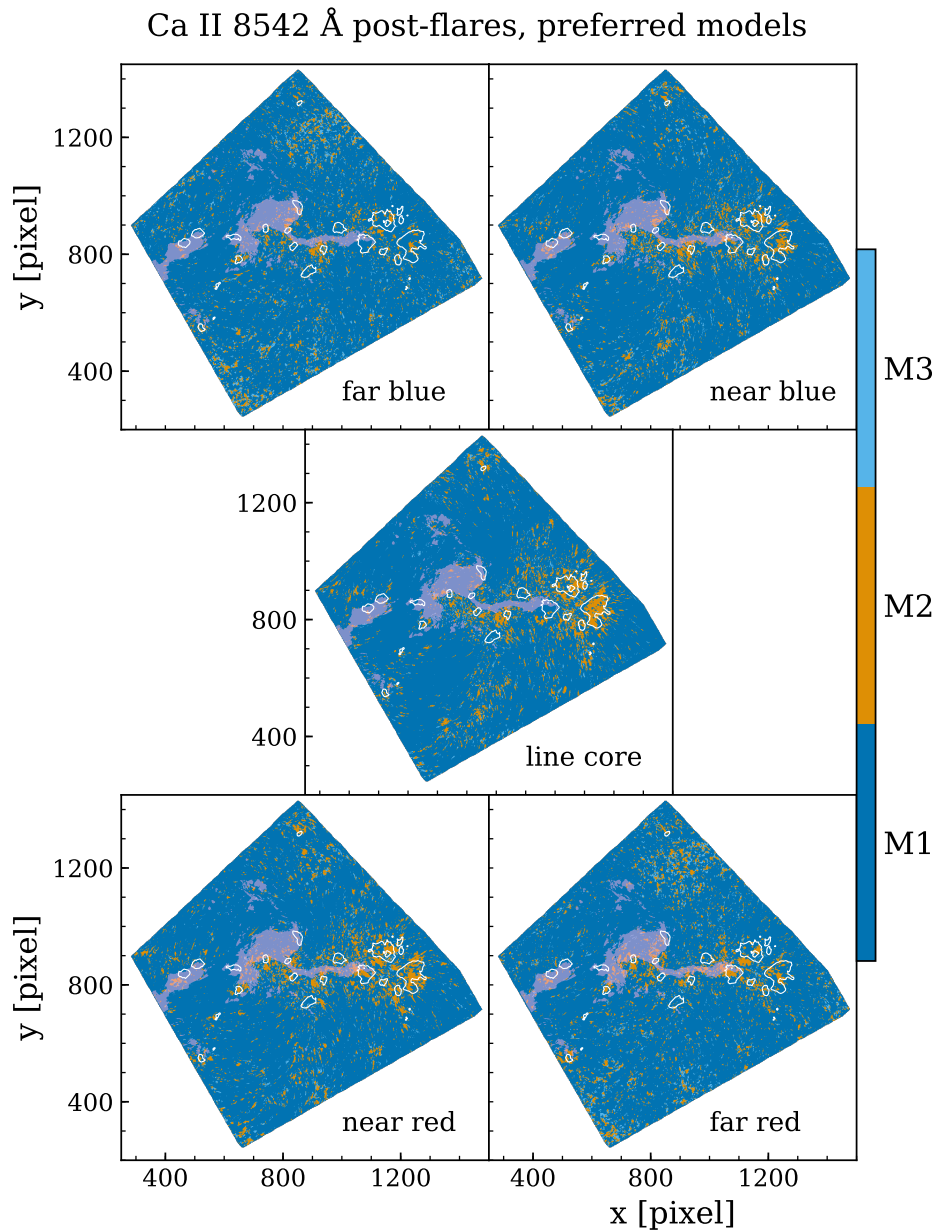
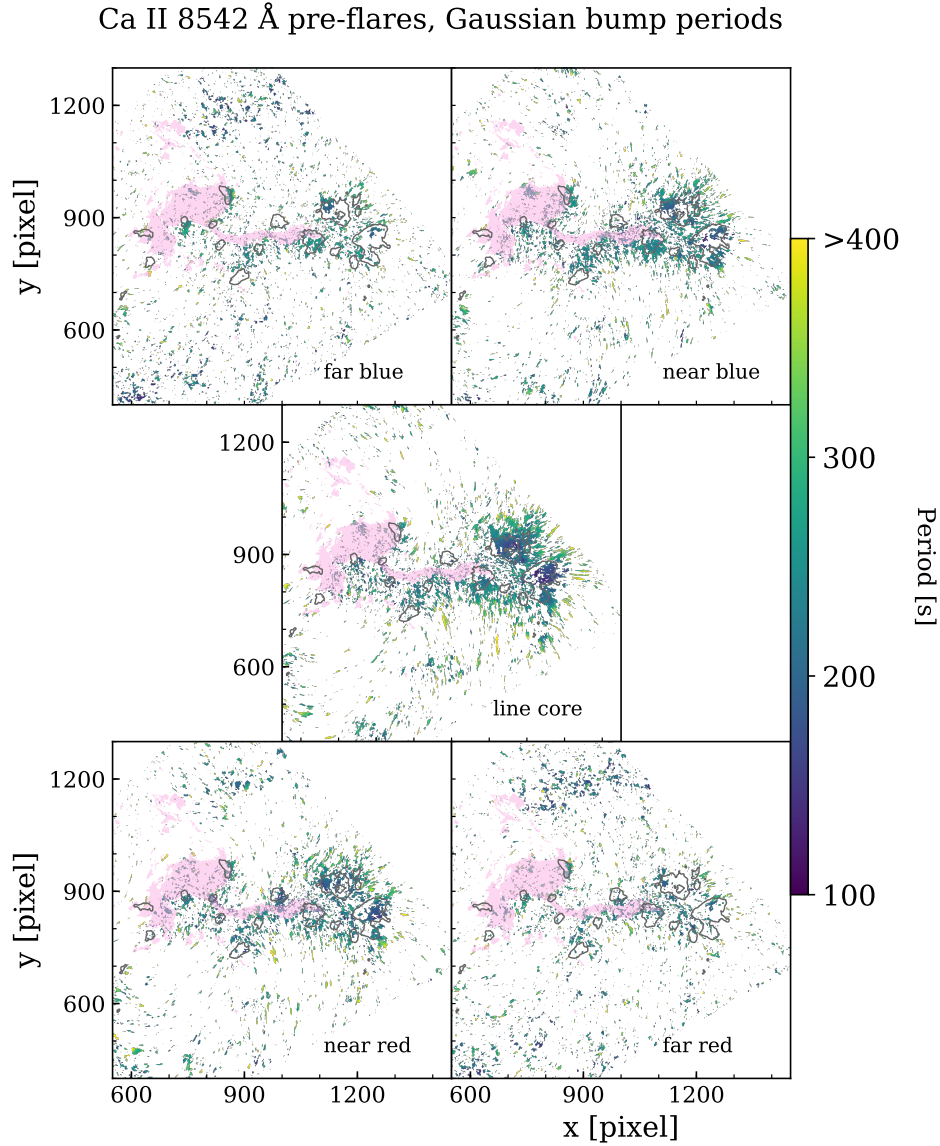


Figure 5.17: Similar to Figure 5.16 but for the post-flares time interval in Ca II 8542 Å intensity.

## 5.4 Velocity oscillations



**Figure 5.18:** The period at which the Gaussian bump peaks in full resolution Ca II 8542 Å in the pre-flares interval when M2 was the preferred model. The plots cover a different span than in Figures 5.16 and 5.17, in order to focus on the group of sunspots with its high concentration of M2 model pixels. The underlying sunspots are shown by the solid contour lines, determined by 40% of the maximum intensity of the linecore of Fe I 5250 Å. The locations of flaring pixels are shown by the filled contours, and have been determined by the maximum brightness of each pixel. The labels in the lower right of each panel show the part of the spectral line they are drawn from.

#### 5.4 Velocity oscillations

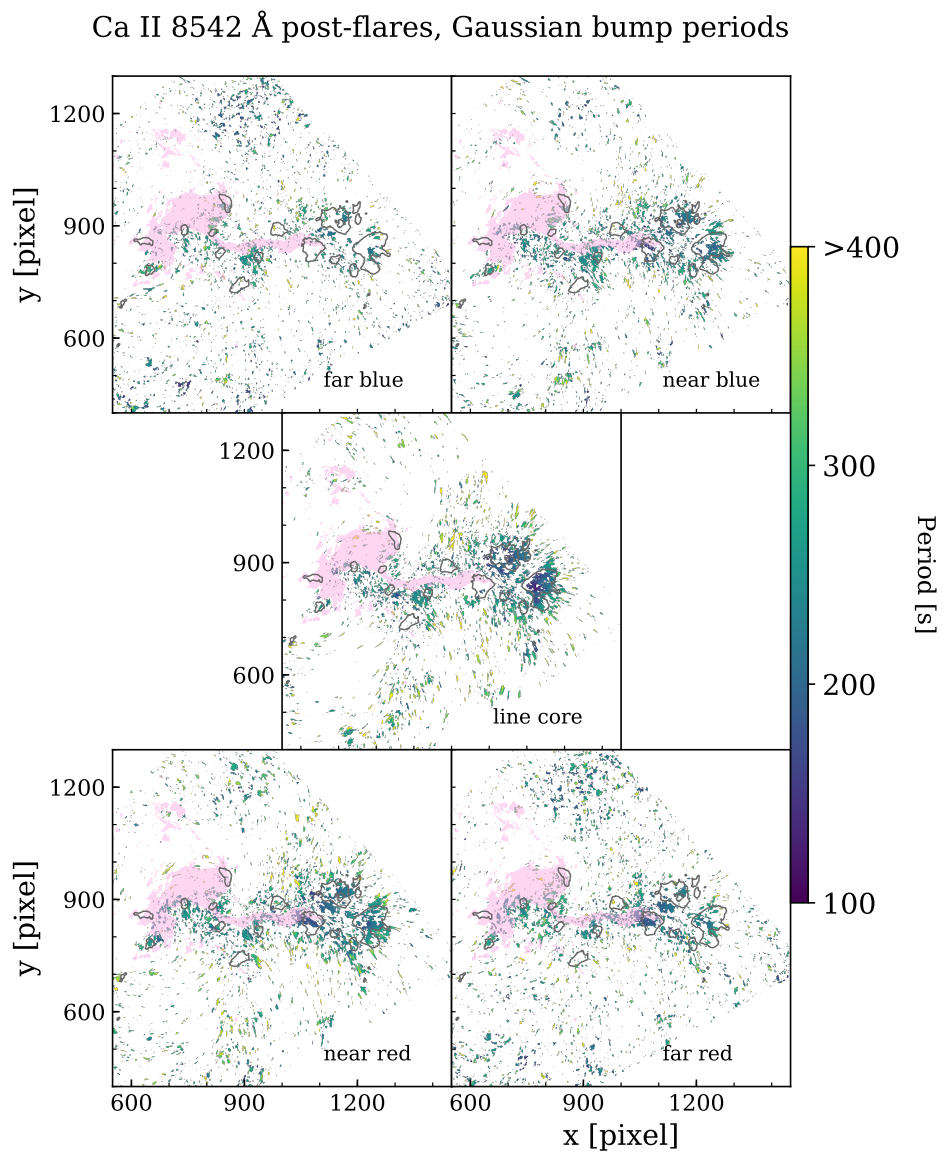
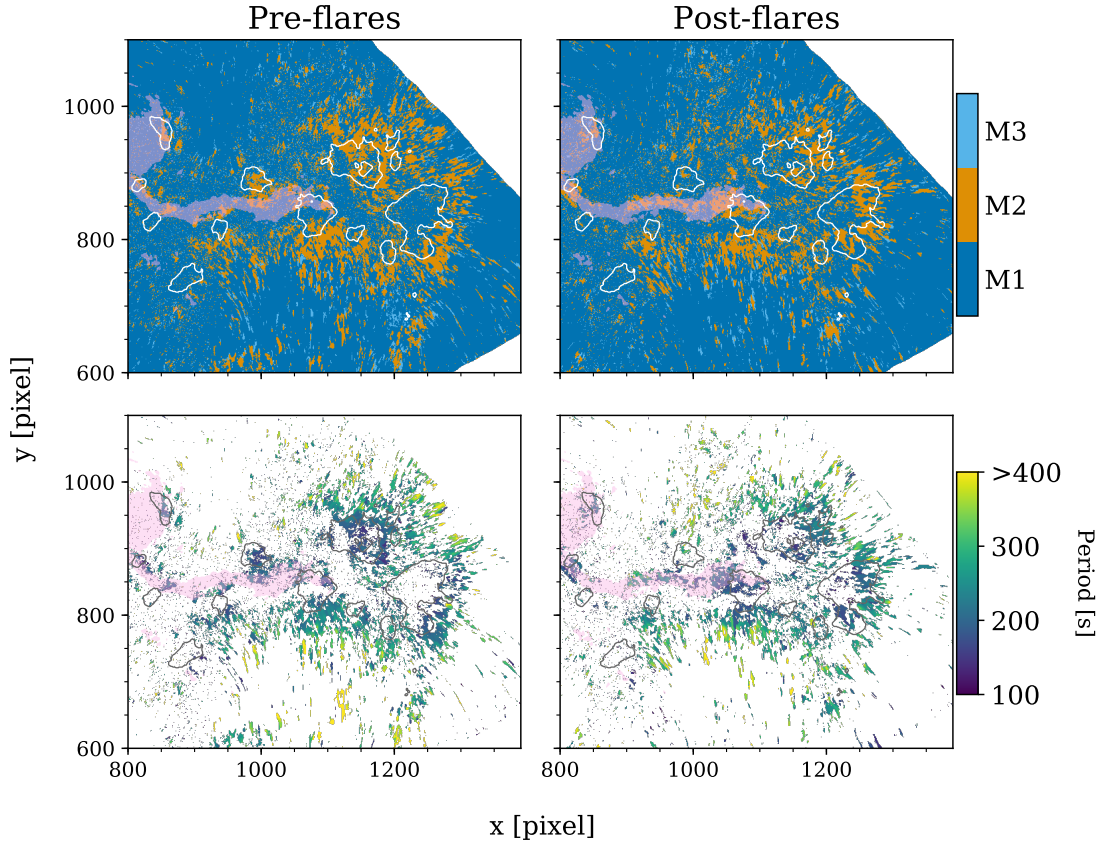


Figure 5.19: Similar to Figure 5.18 but for the post-flares time interval.

## 5.4 Velocity oscillations



**Figure 5.20:** Top row: the preferred power spectrum models in velocity timeseries drawn from Ca II 8542 Å. Bottom row: periods where the Gaussian bumps peak for pixels where M2 was the preferred model. The left column is from the pre-flares interval and the right column is post-flares. The underlying sunspots are shown by the solid contours and the flaring pixels by the filled contours. The field of view is cropped to avoid the dynamic filament to the east.

informative. As seen in the upper two panels of Figure 5.20, the majority of pixels in the field of view show velocity power spectra which prefer the red noise background model. There is a concentration of velocity oscillations around the sunspots to the right of the field, and there are also many oscillatory signals tracing along the southern edge of the trailing sunspot group. The locations of the signals along the southern edge appear mostly constant when comparing the two time intervals, but with the area showing oscillations in the post-flares results seeming contracted — the signals do not extend as widely in the north-south direction. This contraction is mirrored in the peaks of the Gaussian bumps, where one can see increased periods at the lower side and decreased periods at the upper side — for example, the border of sunspot C.

## 5.4 Velocity oscillations

Sunspot B contains many detectable oscillations over the umbra and around the upper-right umbral border. In the post-flares data the penumbral signals remain but the signals above the umbra are not as pronounced. Over sunspot A the opposite happens: there are more signals around the edge of the umbra in the pre-flares data and the post-flares results show more near the centre of the sunspot.

In terms of the periods of the signals, the Gaussian bump peaks (lower two panels in Figure 5.20) again show a pattern of lower period oscillations towards the centre of the sunspot umbrae. This is clear in sunspot B as there are periods as low as 100 seconds in the middle of the umbra. In the penumbral edges of this sunspot there are periods at 200–300 seconds and further out we see periods approaching 400 seconds. The peak periods do not appear to change between the pre- and post-flares intervals. However, in sunspot A, where the spatial locations of Gaussian bump signals seem to move inwards, in the pre-flares interval there are signals around the umbral border at  $\sim 200$  seconds, and after the flares the same spatial locations show signals closer to 300 seconds, while  $\sim 200$  second signals are present over the umbra.

### 5.4.1 The flare ribbon

Before the flares there are signals along the edges of the flaring ribbon's eventual location (shown as the lilac patch in Figure 5.20), but in the post-flares interval there are velocity oscillations detected along part of the flare ribbon itself. There is a large concentration in the post-flares interval near sunspot C and also a broken line of oscillations following the flare ribbon between  $x = 900$  and  $x = 1000$ . There certainly are concentrations of oscillatory signal very close to the flare ribbon oscillations in the pre-flare data, however the locations do appear to be significantly changed by the post-flare interval. Oscillatory signals have a strong presence at sunspot D, just north of the flare ribbon in the pre-flares data as indicated in Figure 5.20, but little to none after the flares. The signals at this sunspot in the pre-flares interval are similar to those found at the end of the ribbon (near sunspot C) at 100–200 seconds.

### 5.4.2 Intensity vs velocity oscillations

By comparing Figures 5.16–5.19 to Figure 5.20 we can investigate which properties are shared between the identified intensity and velocity oscillations. For example, the loss of signals after the flares over sunspot B is apparent in both the line core intensity and

## *5.5 Evolution of the atmosphere around the oscillatory signals*

velocity data. We can see the long band of oscillations along the southern border of the flare ribbon site in the line core and near blue before the flares, but in post-flares results there are not many intensity oscillations at the line core here, whereas the velocity signals remain in the post-flares data.

The velocity oscillations near the flare ribbon in both pre- and post-flares data seem to correlate well with the near red intensity signals, in spatial location and typical oscillatory periods. In the pre-flares data, there are signals in the near red intensity at sunspot D, similar to the pre-flares velocity results; in the post-flares data the near red intensity shows oscillations near the end of the flare ribbon which match velocity signals, in location and also Gaussian bump peak period.

The line core intensity signals over sunspot A seem to move “inwards” after the flares, covering more of the umbra. In the velocity data, there are almost no oscillations detected over the umbra in pre-flares data, with signals around the penumbra, but in the post-flares interval there are signals mostly on the inside of the umbra-penumbra border. This seems to mimic the behaviour of the line core intensity signals but with the velocity signals lagged spatially.

## **5.5 Evolution of the atmosphere around the oscillatory signals**

Here we present context images and maps of calculated physical parameters to gain an understanding of the possible cause of the changes to the oscillations which were detected.

### **5.5.1 Intensity imaging**

Figure 5.21 shows intensity images over the cluster of sunspots, with the same field of view as Figure 5.20. The top row contains line wing data from the Fe I 5250 Å line, which samples the photosphere, and the lower row is from the Ca II 8542 Å core, showing the chromosphere. We have sampled one image from the start of the observation (in the pre-flares time interval), one from the time of the second flare which saw the brightening of the thin ribbon, and one from near the end of the observations (in the post-flares interval).

## 5.5 Evolution of the atmosphere around the oscillatory signals

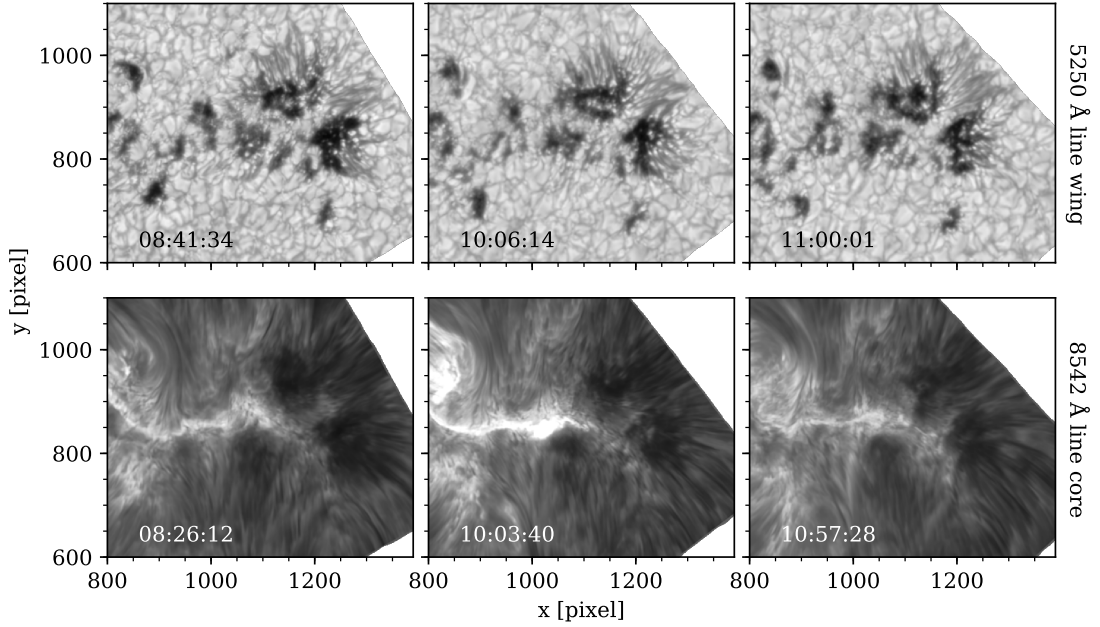


**Figure 5.21:** Top row: Intensity of the wing of the Fe I 5250 Å line at several time instances. Bottom row: Line core intensity of Ca II 8542 Å at several time instances, indicated in the lower left of each panel. The colour scales for each row are constant.

It is clear in the images from Fe I 5250 Å that there is a lot of movement of the sunspot umbrae, particularly for the smallest sunspots which can be seen to move positions entirely over the length of the observation. For the largest sunspots, their shapes change noticeably, particularly around their edges, and we see the appearance and disappearance of bright kernels within the umbrae.

The chromosphere, as shown in the bottom row of Figure 5.21 does not exhibit large-scale obvious changes over the sunspot group. We can see some differences in the shape of the bright ribbon structure which is excited by the flare (visible in the 10:03:40 panel), and it seems to extend further down (in the  $y$ -direction) into the space between sunspot umbrae in the 10:57:28 panel. One noticeable difference is the appearance of the dark sunspots at the chromospheric wavelength. The three largest sunspots in the cluster have corresponding dark patches, at the edges of which many strand-like fibrils are visible. The dark regions around the sunspots in the Ca II 8542 Å data appear more physically extended at 08:26:12 (pre-flares) when compared to the images taken from the post-flares interval.

### 5.5.2 Magnetic field

Over the length of the observations (2.5 hours), the active region had moved  $\sim$ 1.5 degrees around the solar rotation axis. This would slightly affect measurements of the line-of-sight magnetic field, but not by much. On top of these changes due to the rotation of the Sun, we measure significant changes to the magnetic field over the course of the observations, and compare the photospheric and chromospheric fields.

#### Chromospheric field strength

As stated previously, the Stokes  $Q$  and  $U$  data for the Ca II 8542 Å line are too noisy for the determination of the full magnetic field vector to be feasible. Using the  $I$  and  $V$  data, maps were constructed of the line-of-sight magnetic field component using the weak field approximation (Section 2.3.2). The whole available wavelength range of the Ca II 8542 Å line was used, because it does not extend very far into the wings of the line, which can contain measurements of a stronger field lower in the atmosphere. The measurements were applied on a pixel-by-pixel basis on the full resolution data.

The first panel of the Figure 5.22 upper row displays the line-of-sight magnetic field over the sunspot group at the start of the observations, with the subsequent three panels showing the difference in the field since the time of the first panel. At each time step, the results were averaged over a  $\sim$ 6 minute time interval, and then had a Gaussian filter applied over the spatial dimensions. This was to remove the presence of outliers and noisy pixels on the difference plots.

We can see from Figure 5.22 that the line-of-sight component of the chromospheric field is positive almost everywhere in the field of view: the sunspot group is dominated by flux pointing towards the observer. The chromospheric field is as strong as 1.2 kG over the largest sunspots and in the range 500–1000 kG in the immediate vicinity of the umbrae. Across the rest of the field of view the line-of-sight component is almost zero, indicating a very weak or highly inclined field. In the other three panels of the Figure 5.22 upper row we see how the field strength changes over the course of the observations. The first two panels of the figure are drawn from times at the beginning and the end of the pre-flares interval, and the latter two are similarly drawn from after the flares. It is clear that there are significant changes to the field strength in the chromosphere, by as much as  $\pm$ 400 G in some areas. Since the polarity of the field is positive (pointing towards the observer) all over the field of view, a decrease in this value could be indicating that the field has

## 5.5 Evolution of the atmosphere around the oscillatory signals

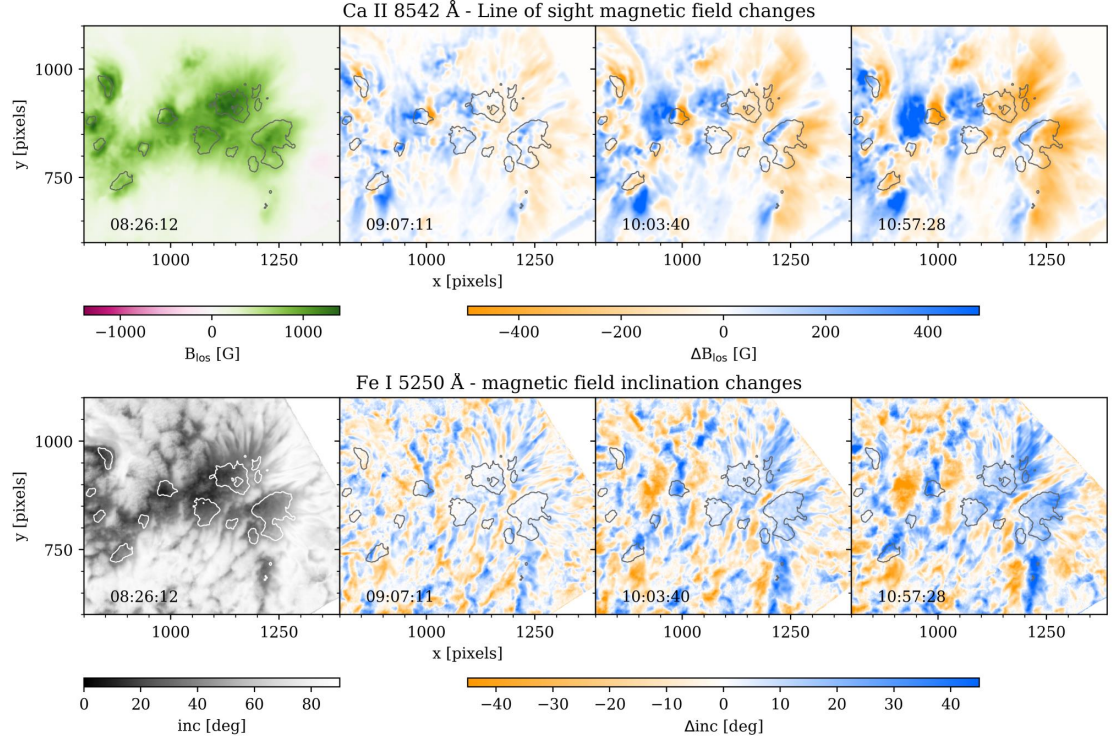


**Figure 5.22:** Upper row: the line-of-sight magnetic field strength as measured by the Ca II 8542 Å using the weak field approximation. The magnetic field values have been averaged in time over a  $\sim$ 6 minute interval around the central time, indicated in the lower left of each panel. A Gaussian smoothing filter was applied to each image before the difference calculation. First panel: The line of sight magnetic field strength. Following panels: Difference images of the line of sight field, in relation to the first panel. Lower row: inclination of the magnetic field at the photosphere, measured by Milne-Eddington inversions on Fe I 5250 Å data. The panel layout is similar to the upper row. Contours show the sunspot umbrae, based on 40% of the Fe I 5250 Å core intensity.

grown more inclined. Similarly, positive changes to the field strength could indicate the field being more closely aligned to the sight line. For instance around sunspot A, the penumbral area to the right of the umbra shows large reductions to the field strength which is likely the field inclining. In the first difference image (09:07:11), the umbra of this sunspot appears to have mostly small positive field changes, but in the following two panels the field strength across much of the umbra reduces to much lower than at 08:26:12.

Some field strength changes shown in the latter three panels of Figure 5.22's upper row seem to exhibit a shift in spatial position; as time passes features move across the field from right to left. For example, sunspot A has a strip of positive field changes, which

## 5.5 Evolution of the atmosphere around the oscillatory signals

moves from the middle of the umbra at 09:07:11 over towards the umbral border in the following two panels. At sunspot D, in the first difference panel the field directly over the spot has mostly increased, and there is a patch of negative field change immediately to its right, and in the following panels the pattern has moved so that the location directly over the spot shows a strong field reduction.

### Photospheric field inclination

The magnetic field inclination with respect to the line of sight, as measured by the photospheric Fe I 5250 Å line was found using magnetic field vector maps, which had been calculated by inversions under the Milne-Eddington approximation<sup>1</sup> (de la Cruz Rodríguez 2019). The lower row of Figure 5.22 is similar to the upper row but showing the field inclination angle, and subsequent differences, measured by Fe I 5250 Å. As seen in the first panel, the field inclination is low over the sunspot group, with the lowest values seen near the umbrae. The surrounding area in the field of view is dominated by very highly inclined fields. From the other three lower panels of Figure 5.22 we see how the field inclination measured at the photosphere changes in the latter part of the observations. Sunspots A, B, and C are dominated by inclination increases — with changes measured up to  $\sim 35^\circ$  — except for a channel in-between the umbrae which shows high inclination in the first panel, and becomes significantly less inclined by the time of the fourth panel.

### Comparing field changes

By comparing the field measured by Ca II 8542 Å and the inclination from the Fe I 5250 Å inversions (Figure 5.22), we see they are very similar in appearance. The chromospheric changes seem to match the photospheric changes quite well, but with some shifting of features in space. For example, sunspot A, which exhibits exclusively inclination increases across the umbra in the Fe I 5250 Å measurements, has a strip of decreasing inclination around the upper-left of the umbra border, but displays corresponding chromospheric line of sight increases in a similarly shaped strip but shifted down and to the right, so that it appears inside the umbral border. This most likely illustrates how magnetic features at different altitudes would appear to lie above a different point on the Sun’s surface, due to the inclination of the field.

---

<sup>1</sup>Inversions performed by J. Joshi using code from <https://github.com/jaimedelacruz/pyMilne>

## 5.6 STiC inversions

In contrast, in the vicinity of the flare ribbon where there was detection of velocity oscillations at sunspot C, the chromospheric field changes do not fully align with the changes to the photospheric field inclination. This is most apparent over the sunspot umbra where there is an increase in the chromospheric field strength, but a decline in the photospheric inclination measurement. This could be a similar effect as seen by Kleint (2017), who detected chromospheric line-of-sight magnetic field strength changes independent of the change to the photospheric field strength.

## 5.6 STiC inversions

### 5.6.1 Inversion setups

To get an impression of the atmospheric parameters over the full span of our spectral coverage, we utilised the STiC inversion code described in Section 2.3.1. The Ca II 8542 Å and Fe I 5250 Å data were firstly calibrated by obtaining the average line profiles from small patches of pixels in “quiet” areas of the field of view. The quiet locations are indicated by red points in Figure 5.2. The averaged profiles were compared to a solar atlas to get a scaling factor and also a wavelength shift which were then applied to the data. This also took into account CRISP’s instrumental degradation and limb darkening effects.

Inversions were performed over a small patch bounded by the box in Figure 5.6. This was chosen to cover the large area of detected velocity oscillations at the flaring pixels near to sunspot C. We chose four time instances at which to perform the inversions, over the  $120 \times 50$  patch. These were chosen to sample times in the pre-flares interval, just after the first flare, just after the second flare, and at the end of the observations (post-flares interval).

The starting atmosphere for the inversions was similar to the FAL-C model atmosphere, with no initial velocity stratification, and a turbulent velocity of  $1.7 \text{ km s}^{-1}$  over 65 values for  $\log \tau_{5000}$ , defining the atmospheric depth axis. The number of nodes which were used for the atmospheric parameters are summed up in Table 5.1. The nodes are equidistant in  $\log \tau_{5000}$  space, between  $\log \tau_{5000} = -6$  and  $\log \tau_{5000} = 2$ . The total number of nodes is the number of free parameters in the minimisation step of the code, so keeping our inversions to as few nodes as possible was crucial. This is partly why we chose only five temperature nodes in the patch inversions: to keep computation time low for the large number of pixels being inverted. We used a low number of nodes in the magnetic field

**Table 5.1:** The number of nodes chosen for the atmospheric parameters in different runs of the STiC inversions.

Run	$T$	$v_{los}$	$v_{turb}$	$B_{\parallel}$	$B_{\perp}$	$B_{\phi}$
Patch cycle 1	5	3	3	2	1	1
Patch cycle 2	5	4	3	2	1	1
Velocity tests	7	4	3	2	1	1
Timeseries line	7	4	3	2	1	1

components because we are more concerned with the thermodynamic properties of the atmosphere.

The results of the first cycle of inversions over the patch were smoothed spatially with a Gaussian filter, to try and remove outlier pixels which were badly-fitted. The smoothed atmosphere was then used as the input for the second cycle, with an additional  $v_{los}$  node added in an attempt to measure the velocity structure more accurately.

We also used STiC to invert a small line of ten pixels at every time instance, obtaining timeseries for the atmospheric parameters. The initialisation of these inversions was more involved than those for the patch, and we used the method employed by [Morosin et al. \(2022\)](#). For data from a single time instance (10:03), we inverted the pixels from the line five times, with five different line-of-sight velocity profiles in the starting atmosphere. Three of the velocity profiles were set to constant values throughout the atmosphere, and two had gradients which steepen in the chromosphere, as shown in Figure 5.23. By using these atmospheres we hoped to more easily identify velocity gradients in the atmosphere. The results from the five velocity inversions were tested for how well the synthetic profiles matched the observations, and for each pixel the best result was selected, and combined into a single atmosphere, with different velocity profiles for each pixel. This combined atmosphere was then used as the input for the inversion of the ten pixel timeseries. We used a larger number of temperature nodes in the timeseries inversion, as the low number of pixels meant that the results were able to be more closely examined.

## 5.6.2 STiC results

### 2D Patch

The atmospheric parameters returned from the STiC inversions over the patch surrounding the site of the potential flare-induced velocity oscillations are shown in Figure 5.24 at an

## 5.6 STiC inversions

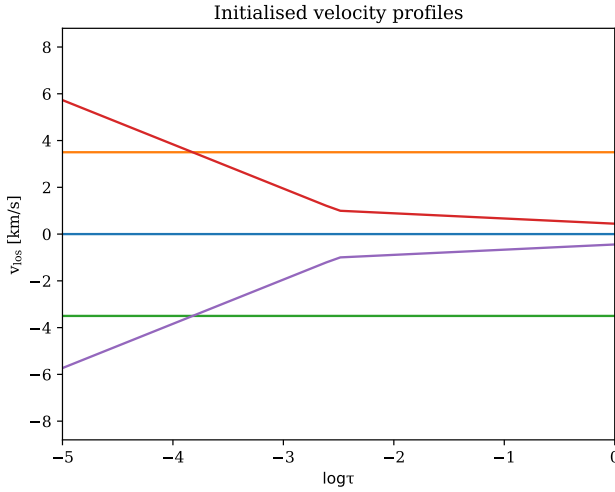


**Figure 5.23:** The five line-of-sight velocity profiles used in the initial atmospheres for the pixels which were used in the STiC timeseries inversions.

optical depth  $\log \tau_{5000} = -3.9$ , a region where Ca II 8542 Å is sensitive (de la Cruz Rodríguez et al. 2019). Each column of the figure shows a different time instance: 08:26, the beginning of the observations (pre-flares interval); 09:32, the time of the first flare (outwith the pre-flares interval); 10:03, the time of the second flare (start of the post-flares interval); 11:00 (end of the post-flares interval). Note that the second time instance is much later than the second instance from Figure 5.22.

The upper row of Figure 5.24 shows temperature, and here we can see the flare heating evident in the second and third panels of this row. At sunspot C, before the flares the temperature is between 4.5–5.0 kK, and it appears even lower in the two flaring panels. At the brighter region of the patch, we see that the temperature ranges from around 5.5 kK up to  $> 7$  kK during the flare heating. By the end of the observation the location of flare heating has cooled to  $\sim 5.5$  kK, to lower than even pre-flares temperatures. The temperature is almost constant across the whole patch at the final time instance, even across much of the area of the sunspot. It is possible that after the flare heating, the cooling plasma spread out over the previously dark umbra of sunspot C.

The line-of-sight velocity results (second row of Figure 5.24) show a fairly wide distribution in the first two time instances, with values ranging between  $\pm 5$  km s $^{-1}$ , except for over the sunspot which shows a tendency to positive velocities. At the time of the greatest flare heating almost the whole patch contains positive velocities, except for an area at the northern sunspot boundary, which is mostly at zero. This same area is where the hotter

## 5.6 STiC inversions

plasma seems to encroach on the sunspot umbra in the final time interval, and at that time the area has developed into strongly positive velocities.

We can see in the third row of Figure 5.24 the turbulent velocity maps at the chromosphere. The turbulence is quite low over the patch except for at the sunspot where the values reach  $\sim 4 \text{ km s}^{-1}$ . We also see higher turbulent velocities at the site of the most intense heating in the third panel. The area of high turbulence over the sunspot shrinks in the third panel, and is vastly reduced in the fourth panel, when the higher temperature plasma covers part of the previously dark sunspot.

The fourth row in Figure 5.24 displays the results of spectral fitting velocity timeseries over this patch, and are sections of Figure 5.20. The first two panels show the pre-flares results, and the latter two show the post-flares results, although we must note that the time of the second panels (09:32:55) is not in the pre-flares interval from which the timeseries were drawn. The pre-flares results are shown in this column for reference, as this time instance is closest to the end of the pre-flares interval than to the start of the post-flares. We see here that there are very few signals over the sunspot in the pre-flares interval (lower right of the patch), and the majority of the detected oscillations are near higher temperature parts of the pre-flares images. In the post-flares interval, we see some oscillatory signals at the location of intense flare heating, though not at every flaring pixel. In the last column there is a section with coordinates ( $y < 840, x < 1030$ ) which is in the flaring area but does not show oscillatory signals, which seems to align with a concentration of very low or negative line-of-sight velocities. As well as in some flaring pixels, oscillations were detected at the location of the hot plasma which spreads over the sunspot, visible in the 11:00:01 temperature panel.

In Figure 5.25 we show a slice of the atmosphere in the inverted patch, taken from along the line with constant  $y = 841$ , as depicted with the dashed lines in Figure 5.24. This  $y$  value was chosen because the line passes through some flaring pixels, and part of the concentration of detected oscillations over the sunspot. These plots have the (logarithm of the) optical depth on the  $y$ -axis and the  $x$ -axis corresponds to  $x$  pixels in the field of view. The three rows depict the same parameters as the first three rows of Figure 5.24 and the columns correspond to the same time instances. We can see the flare activity in the second and third temperature panels, heating lower layers of the atmosphere down to  $\log \tau_{5000} = -2.5$  in the strongest cases. Along the sunspot ( $x > 1050$ ) we see that the lower layers of the atmosphere are measured as almost always positive velocity and the higher layers are much more variable over these time instances, with a mixture of up- and

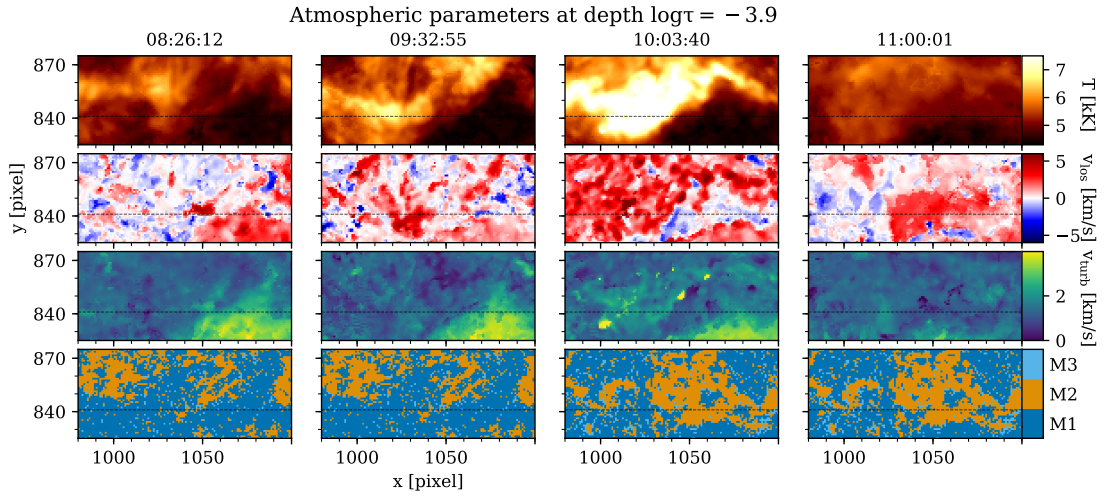


**Figure 5.24:** Atmospheric parameters determined by STiC inversions at four different time values (one per column) at depth  $\log \tau_{5000} = -3.9$ . The first three rows contain temperature, line-of-sight velocity, and turbulent velocity. The fourth row shows the preferred model for velocity timeseries in the pre-flares (first two columns) and post-flares (latter two columns) intervals. The horizontal line shows the location of the atmosphere slice shown in Figure 5.25.

down-flows measured, until the last panel where the whole sunspot atmosphere shows positive velocities along the line-of-sight.

### Timeseries inversions

Figure 5.26 shows the temperature and velocity from a selection of the ten pixels which were used for the timeseries inversions. The time axis covers the whole CRISP observation, measured in minutes from its start (08:21:05). For each pixel there is also a wavelet power spectrum (WPS: Section 2.2.3) computed from the velocity timeseries. This shows the periodicities present as a function of time from the colour scale. The timeseries are drawn from the mid-chromosphere, at  $\log \tau_{5000} = -3.5$ , and from the peaks of the temperature curves we can see the approximate time of the flare heating at these locations.

The temperature timeseries do not show clear oscillatory behaviour, instead we see the random fluctuations associated with red noise. Although the velocity values fluctuate over the course of the observations, there are only select times when the power of the signals (as shown by the WPS) is strong. The most obvious velocity oscillations are seen from  $\Delta t = 135$  min onwards, where there are coherent oscillations in all of the displayed pixels.

## 5.6 STiC inversions

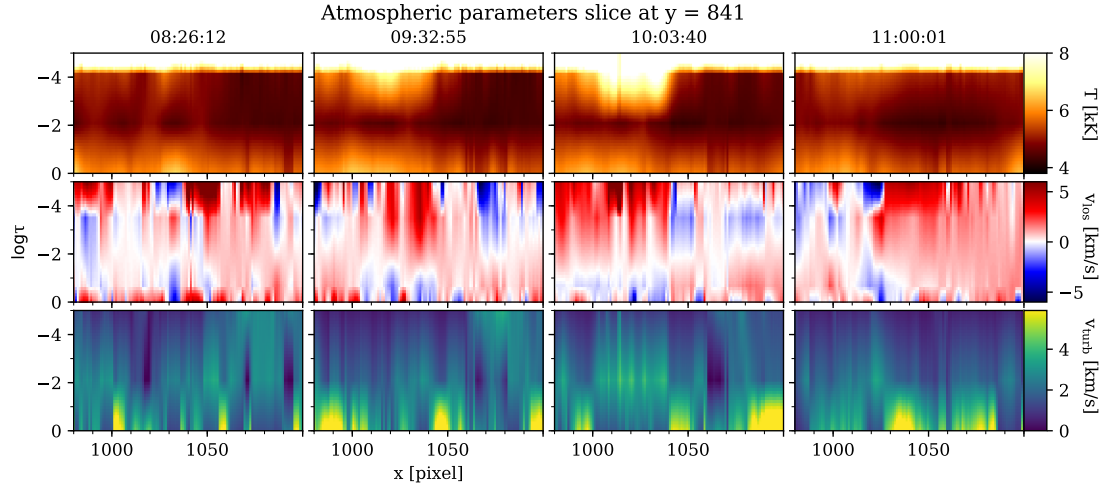


**Figure 5.25:** Atmospheric parameters as a function of  $x$  and depth, at a constant  $y$ -value depicted by the horizontal lines in Figure 5.24. Each row matches the first three of Figure 5.24 showing temperature, line-of-sight velocity, and turbulent velocity.

These signals are at periods of approximately 4 minutes, and for the most part they exist co-temporally with a decrease in the measured temperature. All of these pixels except for Pixel 9 show signals at periods of 150–200 seconds at approximately the time of the flare heating which continues for tens of minutes afterwards ( $\Delta t = 100\text{--}135$  min) but the amplitudes of the oscillations are very small, fluctuating between  $2.5 \text{ km s}^{-1}$  and zero. At around  $\Delta t = 130$  min the amplitudes grow into the very pronounced signals. Because of the small amplitudes, their power is not visible in the wavelet spectra in the majority of cases, and it is difficult to say whether or not these signals are just a trick of the human eye.

There are fluctuations just before the flare heating, which show high power on the wavelet power spectra, occurring at approximately  $\Delta t = 90$  min. The fluctuations appear rather “spiky”, which is something which can add false power to wavelet spectra (similar to a problem for Fourier power spectra which was discussed in Section 2.2.2). As seen for Pixels 6 and 7, the wavelet spectra show power across a wide range of periods at the time of the fluctuations. It is possible these signals are due to spectra which were difficult to fit for the inversion process, though if they are real, they appear to have lower periods (approximately 100–200 seconds) than the oscillations observed later on in the timeseries (above 200 s).

## 5.6 STiC inversions

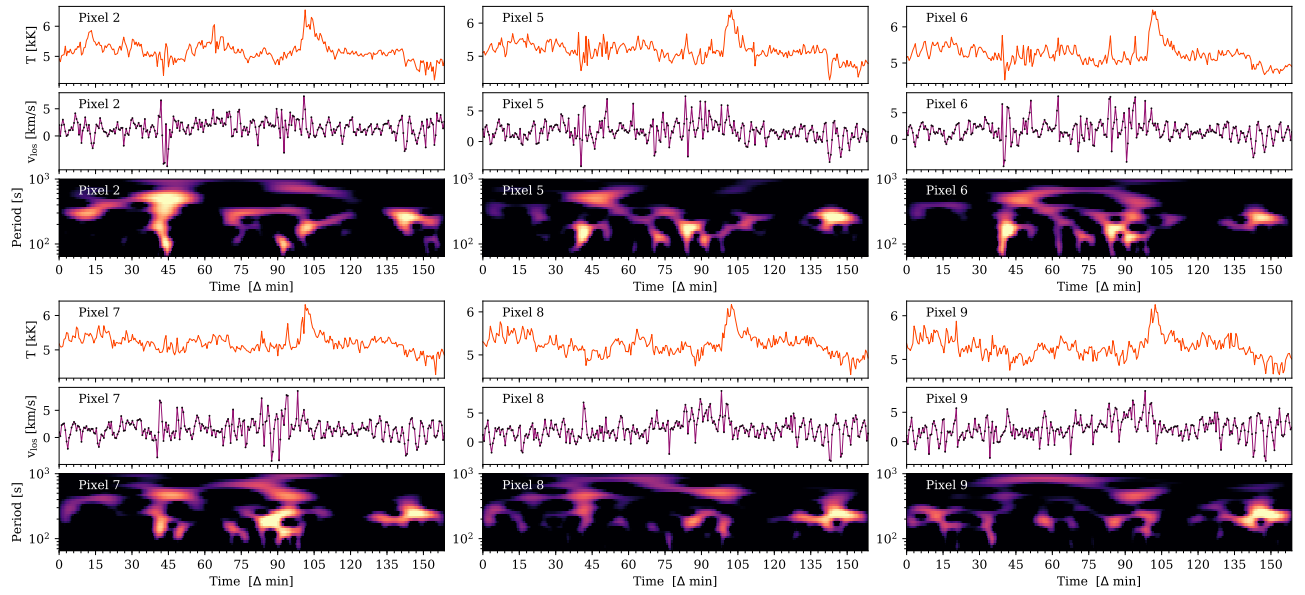


**Figure 5.26:** Each subfigure depicts a different STiC timeseries pixel and contains: the temperature (top panel) and line-of-sight velocity (middle panel) drawn from  $\log \tau_{5000} = -3.5$ , and the wavelet power spectrum (bottom panel) for the velocity timeseries. The colour scale is the same for all wavelet spectra, with limits chosen to accentuate regions of high power.

## 5.7 Discussion

A summary of the main findings from the full-resolution intensity and velocity results is shown in Table 5.2. The figures which are referenced are Figures 5.18, 5.19, 5.20, 5.21, and 5.22. We will now discuss the results in relation to the oscillations observed over the sunspots, and the flare ribbon oscillations. We also compare the broad results of this study to the work presented in Chapter 3.

### 5.7.1 Sunspot oscillations

In Section 5.3 intensity oscillations in the Ca II 8542 Å and Fe I 5250 Å data were identified and contrasted in several wavelengths and over two  $\sim$ 55 minute time intervals. The majority of oscillatory signals were found around the line core of Ca II 8542 Å near the sunspot group which extends across the centre of the field of view, and far fewer signals were identified in the Ca II 8542 Å wings and in the Fe I 5250 Å intensity. This matches the results of Section 3.3, in which the cores of the spectral lines seemed much more sensitive to oscillations. In Section 3.4 we discussed the possibility of this effect being caused by the light near the core emerging from a more compact slab of plasma leading to more coherent oscillatory signals. Meanwhile the results from the Fe I 5250 Å data showed more oscillatory signals from outside the active region, across the “quiet” areas towards the edges of the field of view. The periods were of much longer periods than the chromospheric signals, at around 5 minutes, in keeping with the expected photospheric oscillations.

## 5.7 Discussion

**Table 5.2:** Summary of the main oscillatory results from full-resolution Ca II 8542 Å intensity (Figures 5.18 and 5.19) and velocity (Figure 5.20), with noted changes to the atmosphere which are visible in Figures 5.21 and 5.22.

Location	Pre-flares intensity	Post-flares intensity	Pre-flares velocity	Post-flares velocity	Atmospheric changes
Sunspot A	West inner-umbral border mostly covered. Periods very low at umbral centre 100–200s, increasing radially.	Area shifted inwards over umbral centre. concentration around outside of the west umbra border.	No signals over umbra, umbra, concentration around outside of the west umbra border.	Area shifted towards umbra centre. Periods increased at points that are co-spatial.	Dark area of sunspot appears to have contracted at chromosphere. Field inclines by 30 deg. More penumbral.
Sunspot B	Umbra and north penumbra covered. Periods 150–250s.	Umbra and penumbra covered but much sparser. Loss of low period signals.	Umbra and penumbra covered. Very low periods down to 100s.	Very reduced area over umbra. Penumbra unaffected.	Fe images show growing penumbra. Inclination increases strongly over penumbra.
Sunspot C	Dense coverage over southern half of umbra.	No signals in line core. Near- and far-red signals at 200s (flaring pixels).	Few over umbra.	Reduced area of coverage except at flare pixels.	Photospheric And chromospheric fields do not agree. Shape of spot changes in Fe image.
Sunspot D	Covered umbra, only in near-red wavelengths.	No signals.	Umbra covered, periods ~150s.	No signals.	Sunspot moves eastward, from Fe images.
Flare ribbon	Signals in long band to the south of the ribbon pixels.	Band of signals is gone. Signals partially along ribbon in near- and far-red wavelengths.	Some signals surrounding the horizontal band of flare pixels. Periods 250–300s.	Band of signals contracts. Dense area over flare pixels near sunspot C, 150–200s.	Some movement of underlying magnetic pores visible in Fe.
					Concentrated signals trace ribbon with higher periods.

## 5.7 Discussion

We saw that when comparing pre-flares and post-flares data, there was a reduction in the area covered by oscillatory signals around the large sunspots: signals remained present at the umbra but were no longer present around the penumbra. We see from Figure 5.21 that the penumbral areas over sunspots A and B underwent visible changes. The chromospheric dark regions appear much more extended in the pre-flares interval than in the post-flares. Coupled with the results from Figure 5.22 which gave evidence that the magnetic field in these areas became more inclined in the post-flares interval, it appears that the area surrounding the sunspots is becoming more “penumbral” than “umbral”, with a more inclined field and appearing as a brighter environment. These results suggest that the oscillations are no longer present at this part of the atmosphere, which may be caused by a change to the local cut-off period (i.e. affecting the waves themselves), or it could be that the oscillations are no longer detectable in this spectral line. This could be the case if the height of the strongest signals changed or if the location sampled by the Ca II 8542 Å changed in the later time interval.

For the most part, the typical periods of the intensity oscillations follow the same pattern observed in Section 3.3.2, with shorter period signals coming from closer to the umbral centres, thought to be caused by less inclined magnetic fields towards the middle. Figure 5.22 lends credence to this explanation as they show both photospheric and chromospheric magnetic fields in agreement. At sunspot A in Figures 5.18 and 5.19 we observe oscillatory signals at the right side umbral border which are present at higher typical periods in the post-flares time interval, rising from 100–150 s to  $\sim$ 250 s. This could again be connected to the magnetic field inclination increases affecting the cut-off period. It is unclear whether the magnetic field changes are directly due to the flares, as the values appear to be gradually changing across all time instances of Figure 5.22.

Section 5.4 explored velocity oscillations which are present in the Ca II 8542 Å portion of this dataset and how they related to the intensity oscillations we observed. Velocity oscillations are most easy to detect when a region shows simple spectral lines i.e. when the line is a Gaussian-like emission or absorption feature, close to the centre of the spectral window. It is easy for a coherent velocity signal to be disrupted if the line shape becomes complex – due to a steep velocity gradient in the atmosphere, an absorption feature in the line-of-sight or a large Doppler shift (due to the rather narrow spectral window of the dataset). This is important to keep in mind as it means that a detected velocity signal is likely a real signal, while some locations could be oscillating, but the signals are undetectable by this analysis. Complex line shapes are not as significant for the detection of intensity oscillations.

## 5.7 Discussion

Velocity oscillations were detected over the large sunspots to the right of the field, similar to the intensity oscillations, and also a large concentration was seen along the centre of the field of view, to the south of the flare ribbon's location. The locations of the velocity oscillations over the sunspots were seen to change after the flares, but not consistently: one sunspot showed more oscillations over the umbra in the post-flares data and another showed a reduction in umbral velocity signals. The velocity oscillations follow the typical periods of intensity oscillations: they also show lower periods in regions where the magnetic field inclination is lower, similar to intensity.

### 5.7.2 Flare ribbon oscillations

The ribbon of the second observed flare is not typical, because the physical structure which is brightened appears to be present in the active region before either flare occurred. The bright area running along the centre of the field of view moves subtly over the course of the observations, and as seen in Figure 5.24, the first of the two flares did cause some activity at these locations, though the second flare was much more impactful in terms of chromospheric heating.

There were intensity oscillations detected along the position of the flare ribbon in the pre-flares interval, not directly within the ribbon but rather along its edges. These were seen in line core, near-red and near-blue sections of the full resolution Ca II 8542 Å line intensity at  $\sim 250$  s. In the post-flares interval the line core showed almost no oscillatory signals near the ribbon, but the near- and far-red sections showed oscillations at the end of the ribbon over sunspot C. In Figure 5.24 we see from STiC inversions of this area that at the region in which there is a concentration of oscillatory signals, positive line-of-sight velocity values are prevalent, which explains why the red side of the line showed strong intensity oscillations.

It is in the velocity signals (Figure 5.20) where the ribbon oscillations are most obvious. In the pre-flares interval there are, again, signals along the edges of the bright structure, but in the post-flares interval we see a large concentration of signals with periods 150–200 s near sunspot C. This concentration of signals is almost all within the most active flaring pixels, which encroaches on the umbra of sunspot C. In Figure 5.24 we saw that the area with prevalent oscillatory signals was where heated plasma appeared to spread out as it cooled towards the end of the post-flares interval. The STiC inversion atmosphere slice in Figure 5.25 shows that the atmosphere here was determined by the inversion contained strongly downflowing material, whereas the flare-heated locations without

## 5.7 Discussion

detected velocity oscillations produced upflows at chromospheric depths. There was also a strip of velocity oscillations detected at  $y = 850$  from  $x = 900\text{--}1025$  (Figure 5.20) which quite obviously followed the flaring pixels. The signals along the ribbon had slightly higher periods than those seen at the bright spot over sunspot C.

STiC inversions were carried out on a small number of pixels within the inverted patch, at every timestep, to create timeseries. We saw in Figure 5.26 that in these pixels, velocity fluctuations with very small amplitudes started at approximately the time of the flare heating. The fluctuations were difficult to identify with much certainty, until a time approximately 30 minutes after the time of the flare brightening, at which point all the inverted pixels exhibited very clear oscillations in velocity with amplitudes around  $2.5 \text{ km s}^{-1}$  and periods of approximately 4 minutes, which were sustained until the end of the observations. The strong velocity signals coincided with a drop in temperature for these pixels, which might suggest energy or heat being transported away from the area. If these oscillations were the result of acoustic waves, the energy flux  $F$  of the waves can be estimated using

$$F = \langle \delta p \delta v \rangle \quad (5.41)$$

where  $\delta p$  and  $\delta v$  are the typical changes in gas pressure and velocity (Felipe et al. 2011). We draw estimates for  $\delta v$  and  $\delta p$  from the STiC timeseries results in the eighth pixel during the last 30 minutes of the dataset, at  $\log \tau_{5000} = -3.5$ . These oscillations have approximately  $\delta v = 2.5 \text{ km s}^{-1}$  and  $\delta p = 2.5 \text{ Pa}$ , giving an energy flux of  $F = 5 \times 10^3 \text{ W m}^{-2}$  ( $5 \times 10^6 \text{ erg cm}^{-2} \text{ s}^{-1}$ ). This flux is similar to, but larger than, typical values for acoustic waves in the middle chromosphere observed by, for example Abbasvand et al. (2020). This could indicate that there was increased activity due to the flare energy input.

The time at which the strong oscillations seen in the STiC timeseries start is close to the time at which a coronal loop connected to the group of named sunspots starts to develop. We can see the loop, visible in the  $171\text{\AA}$  image in the last panel of Figure 5.3. The hot loop is not particularly bright in the (flare temperature)  $94\text{\AA}$  image, suggesting that the brightening loop is not another flare event. The oscillations in the chromosphere could be linked to this active loop, from disturbances travelling down the magnetic fields, hence the downflows. We stress that this is very speculative, and we do not have strong evidence for this interpretation at this time.

It is possible that the oscillations we see at the flaring pixels have somehow been induced by the flare heating. The flare could be imparting energy into the chromosphere, causing a “kick” which can excite oscillations, which settle at approximately the cut-off period

## 5.7 Discussion

of the local plasma. The cooling, oscillating plasma shown in Figure 5.24 would suggest that the oscillations are seen towards the end of the observations, as were seen in the STiC timeseries, however it is possible that oscillations could develop over time, as the chromosphere cools. However, as noted above, care must be taken when interpreting the appearance of velocity oscillations at the site of flare heating. The heating from the flare produces strong emission lines in Ca II 8542 Å which leads to easily measureable velocities (either by the quadratic method or using STiC), which might be revealing oscillations which were previously hard to detect (e.g. waves being guided by magnetic field lines from a sunspot). It could be the case that the flare heating causes the Ca II 8542 Å line to sample a different physical height in the atmosphere, thus changing the oscillatory signature. It is also possible that these changes to the oscillations would have appeared without the flare heating. We see across the rest of the field of view that the oscillatory signals do change their location and typical periods devoid of flare activity. However, the closeness with which the signals follow the flare ribbon suggest that the flare activity must be linked to the signals in some way.

### 5.7.3 Comparison to the 2014-09-06 event

The best way to compare the results of this study (2013 event) to those presented in Chapter 3 (2014 event) is by using the reduced-resolution intensity results, shown in Figures 5.8–5.15. For the 2014 event, the spectral coverage of the Ca II 8542 Å line was far wider, but very few oscillatory signals were found in data from the far wings of either the calcium line or H $\alpha$ . In the 2013 dataset, instead of H $\alpha$  we had data available from Fe I 5250 Å. This seems to be a better combination of lines, as the H $\alpha$  results from the 2014 event are rather sparse, and not much extra information was learned from H $\alpha$  than using Ca II 8542 Å alone. The photospheric results from Fe I 5250 Å observed many oscillatory signals around the line core, but detected them outwith the active region, in surrounding quiet areas, mostly with periods over 250 seconds, putting them in the range of the expected 5-minute photospheric oscillations. These results mirror those from AIA 1600 Å and 1700 Å in Chapter 3, and seems to have provided a better photospheric diagnostic than using the wings of the chromospheric lines. This solidifies our reasoning that the wings of chromospheric lines are good for imaging lower in the atmosphere, but oscillatory signals are muddled by the large range of heights sampled.

In the 2014 event, we observed oscillatory signals covering the sunspot umbra in pre-impulsive data, and the signals moved to mostly over the northern umbra/penumbra border in the post-impulsive timeseries. We did not see the exact same pattern in the 2013

### 5.8 Conclusion

event, however the amount of oscillations surrounding the named sunspots was changed, with intensity results showing a kind of “contraction” around the sunspot umbrae. The sunspot umbrae in the 2013 event seemed more densely covered by oscillatory signals than the 2014 umbra. This higher amount of pixels which were fitted by the Gaussian bump model could be to do with the length of the timeseries which were analysed. The 2013 dataset extended much further into the time after the flares, meaning the power spectra being fitted had more datapoints at long periods, so the Gaussian bump model could be more easily characterised. Another possibility is that in a longer span of time, there is more likely to be an oscillatory signal, assuming their occurrence was random.

In the 2013 event we do observe an increase in the length of the dominant periods with distance from the sunspot umbrae, which agrees with the 2014 results. Because there are more sunspots in the 2013 study, identifying flare-associated changes to the periods was more difficult, however we did see some locations where the periods had increased in the post-flares interval, such as over the umbra of sunspot A. In this sunspot, the oscillatory signals seemed to move inwards from the penumbra, retaining their approximate periods.

One of the points put forward in Chapter 3 was whether there could be oscillatory signals in velocity that were not picked up in our intensity analyses. By performing a full study of velocity determined by the chromospheric line in the 2013 event, we were able to identify many locations where velocity oscillatory signals were detected, but few or no intensity signals were present. This suggests that perhaps the 2014 event dataset should be revisited using the velocity analysis performed here.

## 5.8 Conclusion

We set out to investigate the oscillatory signals from this active region which underwent two small solar flares in quick succession. Similar techniques were used as in Chapter 3 to observe oscillations in spectrally resolved intensity data, and we found similar results for how the locations and typical periods changed when comparing pre-flares and post-flares results. As in Chapter 3, one explanation is that the magnetic field inclination had changed, and we were able to verify this interpretation by utilising the full Stokes polarimetry of this dataset to measure the chromospheric and photospheric fields. We extended our analysis to velocity oscillations which were detected across the field of view, and we compared these to the intensity signals found. Velocity signals were detected at the site of flare

### *5.8 Conclusion*

heating in the post-flares data, which we investigated by implementing STiC inversions of the local atmosphere, and found they may be linked to a downflow of cooling plasma over a sunspot. We found that the typical perturbations returned by STiC were in line with high levels of acoustic energy flux of  $F = 5 \times 10^3 \text{ W m}^{-2}$  in the middle chromosphere. Strong velocity signals were found by inversions which could correlate with the development of a coronal loop over the flaring region.

We have found further evidence of how a flare can affect the lower layers of the Sun's atmosphere both directly and indirectly. We have found that oscillatory behaviours can be affected by these small flares in much the same way as for a larger flare.

---

# 6

---

## Conclusions

In this thesis, we have presented work centred around identifying and categorising oscillatory behaviour in data from a variety of sources. With a particular focus on the chromosphere, we have studied oscillations throughout the lower solar atmosphere in active regions, over sunspots, and during energetic injection from solar flares. Care had to be taken to avoid common pitfalls associated with the red-noise nature of solar timeseries. With our method we were able to perform spatially-resolved investigations of periodicities in active regions, while considering the full shape of the observed power spectra. Our interpretations of the results of these investigations were tested through MHD simulations and measurements of the physical parameters in the atmosphere using spectropolarimetric inversions.

In Chapter 2, we outlined the spectral fitting method which we adapted from various studies of quasi-periodic pulsations in the literature, and which we found to be widely adaptable to a variety of timeseries in the studies presented in Chapters 3 and 5. We explained the nature of red noise which is prevalent in many astrophysical timeseries including solar data, and we showed why it is necessary to take caution when attempting to identify periodicities in lightcurves.

The spectral fitting method was used in Chapter 3, where we studied oscillatory signals from an active region which experienced a class M1 solar flare on 6<sup>th</sup> September 2014. We searched for periodicities in H $\alpha$  and Ca II 8542 Å spectroscopic data from the CRISP instrument, as well as in the 1600 Å and 1700 Å filters of SDO/AIA. While the majority of results across the field of view in all wavelengths suggested nothing more than red noise, plentiful oscillatory signals were detected in H $\alpha$  and Ca II 8542 Å line cores over the umbra of a large sunspot, near the site of the chromospheric flare ribbons. Very few oscillations were detected over the active region in the UV channels from AIA, while in the surrounding quiet Sun oscillations were abundant. We considered that this could be

## Chapter 6 Conclusions

due to the layer of the atmosphere which is sampled by these channels: photospheric continuum in quiet sun conditions, and the transition region/upper chromosphere in active regions. A similar explanation exists for why the wings of the CRISP lines showed fewer oscillations than the core. The wings sample lower atmospheric heights, suggesting there are fewer oscillations lower in the atmosphere, but the region sampled in the wings covers a much larger *range* of heights than the line core, which may explain the lack of signals.

When comparing an interval before the impulsive phase of the flare to a post-impulsive interval, we found that the oscillations over the sunspot had changed, both in their locations and the typical periods of oscillation. The area of concentrated signals which covered almost the whole umbra in the pre-flares period appeared to have shifted to the northern umbra/penumbra boundary, and near the centre of the sunspot the typical periods we observed were seen to increase by up to  $\sim 100$  seconds. The interpretation for these results were that the magnetic field over the sunspot had changed its inclination. In regions of high magnetic field strength the angle between the magnetic field and the gravitational field is known to affect the theoretical limit on the periods of acoustic waves which can travel through the atmosphere. Furthermore, waves are thought to be guided by the field lines, meaning a field with an increased inclination angle could have directed waves to a different location in the chromosphere. This presents a possible method for measuring the magnetic field inclination indirectly, through the typical oscillatory periods we observe.

This interpretation was tested using magnetograms from SDO/HMI with 12-minute cadence, and the results were inconclusive. By measuring the evolution of the three magnetic field vector components over time, we observed some locations where there were flare-associated changes to one or more of the components. No systematic changes to the magnetic environment as measured by HMI were found, however the fact that the measurements of the field were averaged over 12-minute windows meant that changes on smaller timescales, expected during a flare, were undetectable. However, from imaging coronal loops with the AIA 171 Å channel, we showed that the magnetic field connectivity in the corona seemed to have changed as a result of the flare.

In Chapter 4, we presented a series of tests using the MHD simulation code Lare2d. We aimed to verify our interpretations of the results from our observational work from Chapter 3, by simulating the solar atmosphere with varying temperature stratifications and magnetic field inclinations. We used the inversion code STiC to get an approximate temperature profile from the sunspot umbra in our observations. The atmospheres were driven from the lower boundary with a wide spectrum of disturbances meant to simulate

## *Chapter 6 Conclusions*

the *p*-modes of the photosphere. Three sets of five simulations were carried out: Set 1 varied the magnetic field inclination in atmospheres following the inverted STiC umbral temperature profile; Set 2 varied the magnetic field inclination in the often-used Maltby Sunspot M atmosphere; and Set 3 varied the height scaling of the umbral temperature profile, in vertical magnetic fields. Set 3 simulated a change to the height of the transition region, which in effect could happen in observed data due to, for example, the heating of lower atmospheric layers due to a flare, or the different stratifications you would expect to see in the umbra versus the penumbra of a sunspot.

Of the tests that were performed, the only property which affected the predominant period of the chromospheric velocity oscillations was the varying magnetic field inclination, which was observed in Sets 1 and 2. The results from Sets 1 and 2 were almost identical, despite having quite different chromospheric temperatures. It was determined that the cause of this similarity was the similar minimum cut-off period values in both atmospheres. We reason that chromospheric disturbances originating from the photosphere must only be limited by the minimum temperature value, but that oscillations with different originating altitudes (e.g. velocity kicks from flares) could cause propagating disturbances with longer periods.

The variations to the length of the chromospheric cavity did not alter the main peak of the chromospheric velocity power spectra, but the minor peaks at lower values of period were affected, most likely due to destructively interfering reflected waves. We concluded that the simulations agreed with our interpretations of the results in Chapter 3, that the inclination angle was the most likely thing to have effected the change in oscillatory behaviour.

A second flare dataset was analysed, and presented in Chapter 5. In this chapter data from the CRISP instrument was used, of an observation of a flaring active region from 13<sup>th</sup> June 2013. The active region was very different in appearance to the one studied in Chapter 3: the flares which occurred during the observation were much less powerful, B7.2 and B9.3 classes, and the sunspots were far smaller with less pronounced penumbras. The dataset featured Ca II 8542 Å and Fe I 5250 Å spectral lines, with the iron line allowing direct measurement of the photosphere with CRISP. We used the same analytical methods as in Chapter 3 so that comparisons could easily be made. However, we also extended the reach of the analysis by applying the spectral fitting method to the CRISP data at full resolution, and by identifying velocity oscillations over the field of view, as well as the previously studied intensity oscillations.

## *Chapter 6 Conclusions*

We found that the photospheric line returned very few results over the active region, but many signals of the order of five minutes were identified by Fe I 5250 Å intensity in the surrounding quiet sun. This suggested that the oscillations detectable by Fe I 5250 Å are similar to the AIA UV channels in quiet conditions.

It was found in the results from the 2013-06-13 observations that there were a variety of changes to the oscillatory behaviour of this active region after the flare activity. We identified a reduction in the amount of oscillatory behaviour around the edges of sunspot umbrae which suggested the development of penumbrae, i.e. brightening of the area and more inclined magnetic fields.

The most striking results of this chapter were found in the results from velocity oscillations. We found strong velocity signals present at the sites of the most intense heating by the second of the two flares, along the chromospheric ribbon and at a bright kernel beside the group of sunspots. Near the sunspots the signals had periods 150–200 seconds and along the ribbon the periods were slightly longer. We investigated the oscillations at the bright kernel through STiC inversions over a 2D patch at a few timesteps, and by timeseries analysis of a small line of flaring pixels. The patch results showed a correlation between the oscillatory signals with cooling plasma, flowing downwards over a small sunspot. We estimated the energy flux of the acoustic waves these oscillations might indicate and found a higher than average flux than typical chromospheric values.

The timeseries results showed that velocity oscillations may have started at the time of the flare heating, but became extremely clear to see around 30 minutes after the flare. They persisted until the end of the dataset, oscillating at between 200–300 second periods, as revealed by wavelet analysis. This point in time,  $\sim$ 20 minutes before the end of the dataset, coincided with the development of a coronal loop above the site of the flare ribbon. We speculated that these two phenomena could be linked.

By comparing the observational results of Chapters 3 and 5 we can see that while the flares in the second dataset were much smaller than the first, there can still be a wealth of information learned about the effects that flares can have on the lower solar atmosphere. We have gained insight into the magnetic environment of the active region, as well as some of the processes behind the energy balance in the chromosphere, by studying these oscillatory signals.

## Future work

As is often the case in science, the results presented in this thesis pose more questions than they answer. This is unavoidable as we seek to expand our understanding of the Sun and its flares. Below we present some future directions that this field could take.

The works presented here are based on two flare events from 2013 and 2014 — almost a decade ago. There have been dozens of flares observed in the last  $\sim$ 20 years with a variety of instrumentation. The spectral fitting method seems to be widely applicable, as we studied intensity from CRISP chromospheric and photospheric lines as well as ultraviolet AIA data, and velocity signals as well. The first question that arises is what else can this technique be applied to? There is no shortage of data sources or flare events for us to study: transition region lines with IRIS, coronal timeseries with AIA EUV channels, timeseries of magnetic field measurements, blue and near-UV data from the CHROMIS instrument at the SST. This is to name but a few, without mentioning the upcoming first studies performed using the next-generational 4m DKIST telescope, or the European Solar Telescope, as well as new space-based sources such as EUI and SPICE on Solar Orbiter.

The fact that both of the datasets we studied showed similar changes to chromospheric oscillations suggest that a systematic study of similar events could be insightful. The spectral fitting method requires little oversight, and could be blindly applied to a variety of data. A challenge would perhaps be how to categorise the change caused by a flare, as we have seen these could take many forms. Another caveat would be that so far we have not detected strong flare-associated changes in data other than with CRISP spectropolarimetry, and CRISP data is not very easily obtainable, such as the publicly available AIA and HMI data services. However, the F-CHROMA database does host a substantial number of CRISP observations. We know that the majority of flares exhibit magnetic field changes, do the majority exhibit changes to chromospheric oscillations?

Our MHD simulations were a good insight into the mechanisms behind the development of sunspot oscillations, however there is much scope for the improvement of these, for instance the Lare3d code would be a natural extension of our work in two dimensions. Our magnetic field structure was uniform, which we know is almost never the case in the real solar atmosphere. More complex magnetic field structures are difficult to employ in such 2D simulations, but we know that the field strength generally reduces from the photosphere into the chromosphere, as the magnetic canopy forms. Simulations of an entire sunspot with increasing magnetic field inclination towards the penumbra would be the ideal setup.

## *Chapter 6 Conclusions*

There are improvements which could be made to the spectral fitting method, particularly when applying this over two-dimensional imaging data. Currently the process works pixel-to-pixel, and is based on least squares minimisations given some starting parameters. If we assume that pixels close together share similar spectra, then the process could be sped up by using the results of surrounding pixels as inputs to the next fit. A more advanced implementation of spatial dependency could be in the form of spatial regularisation, such as that employed by [Morosin et al. \(2020\)](#). The regularisation penalises fits which differ too much from their surrounding pixels. Improved performance of the spectral fitting would mean more data could be processed, which might be necessary for systematic studies featuring many datasets.

There is certainly more analysis available in the datasets from Chapters 3 and 5. The presence of velocity signals in the 2013 event suggests that a study of velocity oscillations using the Ca II 8542 Å data from the 2014 event could be fruitful. This dataset featured a wide spectral window for this line, meaning that larger velocity Doppler shifts could be detectable from this more powerful flare event.

The velocity oscillations seen in Chapter 5 were especially notable because they were observed in pixels which were heated by the second flare. More investigation into this effect would be possible by, for example, a larger-scale study of the dataset using STiC or a similar inversion code. Our analysis inverted ten pixels to extract timeseries, allowing us to infer the development of velocity and temperature in the lower atmosphere, but this is a drop in the ocean compared to the full extent of this dataset. It might be worthwhile conducting a systematic search for velocity oscillations in chromospheric flare ribbons. The event studied here can be added to a growing list of evidence that the energy injected into the chromosphere during flares can excite oscillations. Such a systematic study would need to be able to classify flare ribbons efficiently, which might be possible using machine-learning image classification ([Armstrong & Fletcher 2019](#)).

It is perhaps arbitrary to consider how much we could reveal about these specific events or flares in general if we had additional resources. Great advancements could be made if we had infinite time, infinite computing power, infinite researchers... An infinite number of monkeys could eventually predict the next solar cycle (or write this thesis). One thing that is almost infinite is the amount of data the Sun outputs every day, so we should start now if we ever hope to fully understand it.

# Bibliography

- Abbasvand, V., Sobotka, M., Švanda, M., et al. 2020, *Astronomy & Astrophysics*, 642, A52, doi: [10.1051/0004-6361/202038559](https://doi.org/10.1051/0004-6361/202038559) 132
- Alfvén, H. 1942, *Nature*, 150, 405, doi: [10.1038/150405d0](https://doi.org/10.1038/150405d0) 3
- Allian, F., Jain, R., & Hindman, B. W. 2019, *The Astrophysical Journal*, 880, 3, doi: [10.3847/1538-4357/ab264c](https://doi.org/10.3847/1538-4357/ab264c) 11
- Arber, T. D., Longbottom, A. W., Gerrard, C. L., & Milne, A. M. 2001, *Journal of Computational Physics*, 171, 151, doi: [10.1006/jcph.2001.6780](https://doi.org/10.1006/jcph.2001.6780) 63
- Armstrong, J. A., & Fletcher, L. 2019, *Solar Physics*, 294, 80, doi: [10.1007/s11207-019-1473-z](https://doi.org/10.1007/s11207-019-1473-z) 141
- Aschwanden, M. J. 2011, *Solar Physics*, 274, 99, doi: [10.1007/s11207-011-9755-0](https://doi.org/10.1007/s11207-011-9755-0) 29
- Aschwanden, M. J., Fletcher, L., Schrijver, C. J., & Alexander, D. 1999, *The Astrophysical Journal*, 520, 880, doi: [10.1086/307502](https://doi.org/10.1086/307502) 11
- Aschwanden, M. J., & Schrijver, C. J. 2011, *The Astrophysical Journal*, 736, 102, doi: [10.1088/0004-637X/736/2/102](https://doi.org/10.1088/0004-637X/736/2/102) 11
- Asensio Ramos, A. 2011, *The Astrophysical Journal*, 731, 27, doi: [10.1088/0004-637X/731/1/27](https://doi.org/10.1088/0004-637X/731/1/27) 37, 38
- Auchère, F., Froment, C., Bocchialini, K., Buchlin, E., & Solomon, J. 2016, *The Astrophysical Journal*, 825, 110, doi: [10.3847/0004-637X/825/2/110](https://doi.org/10.3847/0004-637X/825/2/110) 22, 26, 27, 28, 30, 32, 33
- Ball, D. W. 2006, in *Field Guide to Spectroscopy* (1000 20th Street, Bellingham, WA 98227-0010 USA: SPIE), 32, doi: [10.1117/3.682726](https://doi.org/10.1117/3.682726) 15
- Batchelor, G. K. 1967, in *An introduction to fluid dynamics*, Cambridge mathematical library (Cambridge: Cambridge University Press), 71 65
- Battams, K., Gallagher, B. M., & Weigel, R. S. 2019, *Solar Physics*, 294, 11, doi: [10.1007/s11207-019-1399-5](https://doi.org/10.1007/s11207-019-1399-5) 28, 29, 32, 57
- Bel, N., & Leroy, B. 1977, *Astronomy and Astrophysics*, 55, 239. <https://ui.adsabs.harvard.edu/abs/1977A&A....55..239B> 8

## Bibliography

- Bhatnagar, A., & Tanaka, K. 1972, Solar Physics, 24, doi: [10.1007/BF00231085](https://doi.org/10.1007/BF00231085) 7
- Bonanno, A., Schlattl, H., & Paternò, L. 2002, Astronomy & Astrophysics, 390, 1115, doi: [10.1051/0004-6361:20020749](https://doi.org/10.1051/0004-6361:20020749) 1
- Borrero, J. M., Tomczyk, S., Kubo, M., et al. 2011, Solar Physics, 273, 267, doi: [10.1007/s11207-010-9515-6](https://doi.org/10.1007/s11207-010-9515-6) 18, 35
- Botha, G. J. J., Arber, T. D., Nakariakov, V. M., & Zhugzhda, Y. D. 2011, The Astrophysical Journal, 728, 84, doi: [10.1088/0004-637X/728/2/84](https://doi.org/10.1088/0004-637X/728/2/84) 9, 63, 65
- Braun, D. C., Duvall, Jr., T. L., & Labonte, B. J. 1987, The Astrophysical Journal, 319, L27, doi: [10.1086/184949](https://doi.org/10.1086/184949) 57
- Brown, J. C. 1971, Solar Physics, 18, 489, doi: [10.1007/BF00149070](https://doi.org/10.1007/BF00149070) 5
- Brown, R. 1828, The Philosophical Magazine, 4, 161, doi: [10.1080/14786442808674769](https://doi.org/10.1080/14786442808674769) 22
- Cally, P. S., Crouch, A. D., & Braun, D. C. 2003, Monthly Notices of the Royal Astronomical Society, 346, 381, doi: [10.1046/j.1365-2966.2003.07019.x](https://doi.org/10.1046/j.1365-2966.2003.07019.x) 57
- Carlsson, M., & Stein, R. F. 1992, The Astrophysical Journal, 397, L59, doi: [10.1086/186544](https://doi.org/10.1086/186544) 16
- . 1997, The Astrophysical Journal, 481, 500, doi: [10.1086/304043](https://doi.org/10.1086/304043) 16
- Carmichael, H. 1964, NASA Special Publication, 50, 451. <https://ui.adsabs.harvard.edu/abs/1964NASSP..50..451C> 5
- Carrington, R. C. 1859, Monthly Notices of the Royal Astronomical Society, 20, 13, doi: [10.1093/mnras/20.1.13](https://doi.org/10.1093/mnras/20.1.13) 4
- Castellanos Durán, J. S., Kleint, L., & Calvo-Mozo, B. 2018, The Astrophysical Journal, 852, 25, doi: [10.3847/1538-4357/aa9d37](https://doi.org/10.3847/1538-4357/aa9d37) 5
- Centeno, R. 2018, The Astrophysical Journal, 866, 89, doi: [10.3847/1538-4357/aae087](https://doi.org/10.3847/1538-4357/aae087) 38
- Centeno, R., Schou, J., Hayashi, K., et al. 2014, Solar Physics, 289, 3531, doi: [10.1007/s11207-014-0497-7](https://doi.org/10.1007/s11207-014-0497-7) 18
- Chae, J., & Goode, P. R. 2015, The Astrophysical Journal, 808, 118, doi: [10.1088/0004-637X/808/2/118](https://doi.org/10.1088/0004-637X/808/2/118) 8, 9
- Chapman, S., & Bartels, J. 1940, Geomagnetism, Vol. I: Geomagnetic and Related Phenomena. <https://ui.adsabs.harvard.edu/abs/1940gm1..book.....c> 4
- Christensen-Dalsgaard, J. 2002, Reviews of Modern Physics, 74, 1073, doi: [10.1103/RevModPhys.74.1073](https://doi.org/10.1103/RevModPhys.74.1073) 6
- Clette, F., Svalgaard, L., Vaquero, J. M., & Cliver, E. W. 2014, Space Science Reviews, 186, 35, doi: [10.1007/s11214-014-0074-2](https://doi.org/10.1007/s11214-014-0074-2) 6

## Bibliography

- Cliver, E. W., & Dietrich, W. F. 2013, Journal of Space Weather and Space Climate, 3, A31, doi: [10.1051/swsc/2013053](https://doi.org/10.1051/swsc/2013053) 5
- Cliver, E. W., Schrijver, C. J., Shibata, K., & Usoskin, I. G. 2022, Living Reviews in Solar Physics, 19, 2, doi: [10.1007/s41116-022-00033-8](https://doi.org/10.1007/s41116-022-00033-8) 2
- Costa, F. R. d., Kleint, L., Petrosian, V., Dalda, A. S., & Liu, W. 2015, The Astrophysical Journal, 804, 56, doi: [10.1088/0004-637X/804/1/56](https://doi.org/10.1088/0004-637X/804/1/56) 56
- de la Cruz Rodríguez, J. 2019, Astronomy & Astrophysics, 631, A153, doi: [10.1051/0004-6361/201936635](https://doi.org/10.1051/0004-6361/201936635) 120
- de la Cruz Rodríguez, J., Leenaarts, J., & Asensio Ramos, A. 2016, The Astrophysical Journal, 830, L30, doi: [10.3847/2041-8205/830/2/L30](https://doi.org/10.3847/2041-8205/830/2/L30) 35
- de la Cruz Rodríguez, J., Leenaarts, J., Danilovic, S., & Uitenbroek, H. 2019, Astronomy & Astrophysics, 623, A74, doi: [10.1051/0004-6361/201834464](https://doi.org/10.1051/0004-6361/201834464) 35, 123
- de la Cruz Rodríguez, J., Löfdahl, M. G., Sütterlin, P., Hillberg, T., & Rouppe van der Voort, L. 2015, Astronomy & Astrophysics, 573, A40, doi: [10.1051/0004-6361/201424319](https://doi.org/10.1051/0004-6361/201424319) 14
- de la Cruz Rodríguez, J., & Piskunov, N. 2013, The Astrophysical Journal, 764, 33, doi: [10.1088/0004-637X/764/1/33](https://doi.org/10.1088/0004-637X/764/1/33) 36
- de la Cruz Rodríguez, J., & van Noort, M. 2017, Space Science Reviews, 210, 109, doi: [10.1007/s11214-016-0294-8](https://doi.org/10.1007/s11214-016-0294-8) 35
- De Moortel, I., & Browning, P. 2015, Philosophical Transactions of the Royal Society A: Mathematical, Physical and Engineering Sciences, 373, 20140269, doi: [10.1098/rsta.2014.0269](https://doi.org/10.1098/rsta.2014.0269) 4
- Degl'Innocenti, E. L., & Degl'Innocenti, M. L. 1973, Solar Physics, 31, 299, doi: [10.1007/BF00152807](https://doi.org/10.1007/BF00152807) 37
- Degl'Innocenti, E. L., & Landolfi, M. 2004, Polarization in spectral lines, Astrophysics and space science library No. v. 307 (Dordrecht ; Boston: Kluwer Academic Publishers) 38
- del Toro Iniesta, J. C., & Ruiz Cobo, B. 2016, Living Reviews in Solar Physics, 13, 4, doi: [10.1007/s41116-016-0005-2](https://doi.org/10.1007/s41116-016-0005-2) 35
- Deubner, F.-L., & Gough, D. 1984, Annual Review of Astronomy and Astrophysics, 22, 593, doi: [10.1146/annurev.aa.22.090184.003113](https://doi.org/10.1146/annurev.aa.22.090184.003113) 8
- Dolla, L., Marqué, C., Seaton, D. B., et al. 2012, The Astrophysical Journal, 749, L16, doi: [10.1088/2041-8205/749/1/L16](https://doi.org/10.1088/2041-8205/749/1/L16) 27
- Dominique, M., Zhukov, A. N., Dolla, L., Inglis, A., & Lapenta, G. 2018, Solar Physics, 293, 61, doi: [10.1007/s11207-018-1281-x](https://doi.org/10.1007/s11207-018-1281-x) 25

## Bibliography

- Donea, A. C., Besliu-Ionescu, D., Cally, P. S., Lindsey, C., & Zharkova, V. V. 2006, Solar Physics, 239, 113, doi: [10.1007/s11207-006-0108-3](https://doi.org/10.1007/s11207-006-0108-3) 10
- Duvall, Jr., T. L., Harvey, J. W., Jefferies, S. M., & Pomerantz, M. A. 1991, The Astrophysical Journal, 373, 308, doi: [10.1086/170052](https://doi.org/10.1086/170052) 8
- Einstein, A. 1905, Annalen der Physik, 322, 549, doi: [10.1002/andp.19053220806](https://doi.org/10.1002/andp.19053220806) 22
- Farris, L., & McAteer, R. T. J. 2020, The Astrophysical Journal, 903, 19, doi: [10.3847/1538-4357/abb701](https://doi.org/10.3847/1538-4357/abb701) 12, 57
- Felipe, T. 2019, Astronomy & Astrophysics, 627, A169, doi: [10.1051/0004-6361/201935784](https://doi.org/10.1051/0004-6361/201935784) 9, 63
- Felipe, T., Khomenko, E., & Collados, M. 2011, The Astrophysical Journal, 735, 65, doi: [10.1088/0004-637X/735/1/65](https://doi.org/10.1088/0004-637X/735/1/65) 132
- Fisher, G. H., Bercik, D. J., Welsch, B. T., & Hudson, H. S. 2012, Solar Physics, 277, 59, doi: [10.1007/s11207-011-9907-2](https://doi.org/10.1007/s11207-011-9907-2) 11
- Fleck, B., & Schmitz, F. 1991, Astronomy and Astrophysics, 250, 235. <https://ui.adsabs.harvard.edu/abs/1991A&A...250..235F> 8, 9
- Fletcher, L., Dennis, B. R., Hudson, H. S., et al. 2011, Space Science Reviews, 159, 19, doi: [10.1007/s11214-010-9701-8](https://doi.org/10.1007/s11214-010-9701-8) 4, 5
- Fontenla, J. M., Avrett, E. H., & Loeser, R. 1993, The Astrophysical Journal, 406, 319, doi: [10.1086/172443](https://doi.org/10.1086/172443) 2, 16, 65
- Freij, N., Dorotovič, I., Morton, R. J., et al. 2016, The Astrophysical Journal, 817, 44, doi: [10.3847/0004-637X/817/1/44](https://doi.org/10.3847/0004-637X/817/1/44) 9
- Garcia, H. A. 1994, Solar Physics, 154, 275, doi: [10.1007/BF00681100](https://doi.org/10.1007/BF00681100) 5
- Goldreich, P., & Kumar, P. 1988, The Astrophysical Journal, 326, 462, doi: [10.1086/166108](https://doi.org/10.1086/166108) 57
- Graham, D. R., & Cauzzi, G. 2015, The Astrophysical Journal, 807, L22, doi: [10.1088/2041-8205/807/2/L22](https://doi.org/10.1088/2041-8205/807/2/L22) 5
- Gruber, D., Lachowicz, P., Bissaldi, E., et al. 2011, Astronomy & Astrophysics, 533, A61, doi: [10.1051/0004-6361/201117077](https://doi.org/10.1051/0004-6361/201117077) 28
- Gudiksen, B. V., Carlsson, M., Hansteen, V. H., et al. 2011, Astronomy & Astrophysics, 531, A154, doi: [10.1051/0004-6361/201116520](https://doi.org/10.1051/0004-6361/201116520) 16
- Guglielmi, A. V., & Potapov, A. S. 2021, Physics-Uspekhi, 64, 452, doi: [10.3367/UFNe.2020.06.038777](https://doi.org/10.3367/UFNe.2020.06.038777) 6
- Hale, G. E. 1931, The Astrophysical Journal, 73, 379, doi: [10.1086/143316](https://doi.org/10.1086/143316) 4

## Bibliography

- Hayes, L. A., Gallagher, P. T., Dennis, B. R., et al. 2019, *The Astrophysical Journal*, 875, 33, doi: [10.3847/1538-4357/ab0ca3](https://doi.org/10.3847/1538-4357/ab0ca3) 10
- . 2016, *The Astrophysical Journal*, 827, L30, doi: [10.3847/2041-8205/827/2/L30](https://doi.org/10.3847/2041-8205/827/2/L30) 27
- Hayes, L. A., Inglis, A. R., Christe, S., Dennis, B., & Gallagher, P. T. 2020, *The Astrophysical Journal*, 895, 50, doi: [10.3847/1538-4357/ab8d40](https://doi.org/10.3847/1538-4357/ab8d40) 10
- Hindman, B. W., Jain, R., & Zweibel, E. G. 1997, *The Astrophysical Journal*, 476, 392, doi: [10.1086/303615](https://doi.org/10.1086/303615) 57
- Hirayama, T. 1974, *Solar Physics*, 34, 323, doi: [10.1007/BF00153671](https://doi.org/10.1007/BF00153671) 5
- Hodgson, R. 1859, *Monthly Notices of the Royal Astronomical Society*, 20, 15, doi: [10.1093/mnras/20.1.15a](https://doi.org/10.1093/mnras/20.1.15a) 4
- Hoeksema, J. T., Liu, Y., Hayashi, K., et al. 2014, *Solar Physics*, 289, 3483, doi: [10.1007/s11207-014-0516-8](https://doi.org/10.1007/s11207-014-0516-8) 18, 58
- Howard, R. F., Harvey, J. W., & Forgach, S. 1990, *Solar Physics*, 130, 295, doi: [10.1007/BF00156795](https://doi.org/10.1007/BF00156795) 43
- Hudson, H. S., Fisher, G. H., & Welsch, B. T. 2008, 383, 221. <https://ui.adsabs.harvard.edu/abs/2008ASPC..383..221H> 11
- Huppenkothen, D., Watts, A. L., Uttley, P., et al. 2013, *The Astrophysical Journal*, 768, 87, doi: [10.1088/0004-637X/768/1/87](https://doi.org/10.1088/0004-637X/768/1/87) 22
- Ichimoto, K., & Kurokawa, H. 1984, *Solar Physics*, 93, 105, doi: [10.1007/BF00156656](https://doi.org/10.1007/BF00156656) 5
- Inglis, A. R., Ireland, J., Dennis, B. R., Hayes, L., & Gallagher, P. 2016, *The Astrophysical Journal*, 833, 284, doi: [10.3847/1538-4357/833/2/284](https://doi.org/10.3847/1538-4357/833/2/284) 10, 28
- Inglis, A. R., Ireland, J., & Dominique, M. 2015, *The Astrophysical Journal*, 798, 108, doi: [10.1088/0004-637X/798/2/108](https://doi.org/10.1088/0004-637X/798/2/108) 28, 30, 55
- Jain, R., Hindman, B. W., & Zweibel, E. G. 1996, *The Astrophysical Journal*, 464, 476, doi: [10.1086/177337](https://doi.org/10.1086/177337) 57
- Jess, D. B., Reznikova, V. E., Van Doorsselaere, T., Keys, P. H., & Mackay, D. H. 2013, *The Astrophysical Journal*, 779, 168, doi: [10.1088/0004-637X/779/2/168](https://doi.org/10.1088/0004-637X/779/2/168) 8, 52
- Jess, D. B., Snow, B., Houston, S. J., et al. 2020, *Nature Astronomy*, 4, 220, doi: [10.1038/s41550-019-0945-2](https://doi.org/10.1038/s41550-019-0945-2) 65, 86, 89
- Joshi, J., Lagg, A., Solanki, S. K., et al. 2016, *Astronomy and Astrophysics*, 596, A8, doi: [10.1051/0004-6361/201629214](https://doi.org/10.1051/0004-6361/201629214) 37
- Kalkofen, W., Rossi, P., Bodo, G., & Massaglia, S. 1994, *Astronomy and Astrophysics*, 284, 976. <https://ui.adsabs.harvard.edu/abs/1994A&A...284..976K> 8

## Bibliography

- Keys, P. H., Jess, D. B., Mathioudakis, M., & Keenan, F. P. 2011, *Astronomy and Astrophysics*, 529, A127, doi: [10.1051/0004-6361/201016320](https://doi.org/10.1051/0004-6361/201016320) 98
- Khomenko, E., & Collados, M. 2015, *Living Reviews in Solar Physics*, 12, 6, doi: [10.1007/lrsp-2015-6](https://doi.org/10.1007/lrsp-2015-6) 7, 53
- Kianfar, S., Leenaarts, J., Danilovic, S., de la Cruz Rodríguez, J., & Díaz Baso, C. J. 2020, *Astronomy and Astrophysics*, 637, A1, doi: [10.1051/0004-6361/202037572](https://doi.org/10.1051/0004-6361/202037572) 37
- Kimball, D. S. 1960, *A Study of the Aurora of 1859*, Geophysical Institute at the University of Alaska. <http://hdl.handle.net/11122/3607> 4
- Kleint, L. 2017, *The Astrophysical Journal*, 834, 26, doi: [10.3847/1538-4357/834/1/26](https://doi.org/10.3847/1538-4357/834/1/26) 38, 60, 121
- Kobanov, N. I., Kolobov, D. Y., & Chupin, S. A. 2008, *Astronomy Letters*, 34, 133, doi: [10.1134/S1063773708020060](https://doi.org/10.1134/S1063773708020060) 57
- Kobanov, N. I., Kolobov, D. Y., Chupin, S. A., & Nakariakov, V. M. 2011, *Astronomy & Astrophysics*, 525, A41, doi: [10.1051/0004-6361/200913533](https://doi.org/10.1051/0004-6361/200913533) 57
- Kopp, G. 2016, *Journal of Space Weather and Space Climate*, 6, A30, doi: [10.1051/swsc/2016025](https://doi.org/10.1051/swsc/2016025) 2
- Kopp, R., & Pneuman, G. 1976, *Solar Physics*, 50, doi: [10.1007/BF00206193](https://doi.org/10.1007/BF00206193) 5
- Kosovichev, A. G. 2015, in *Extraterrestrial Seismology*, 1st edn., ed. V. C. H. Tong & R. A. García (Cambridge University Press), 306–322, doi: [10.1017/CBO9781107300668.025](https://doi.org/10.1017/CBO9781107300668.025) 10
- Kosovichev, A. G., & Sekii, T. 2007, *The Astrophysical Journal*, 670, L147, doi: [10.1086/524298](https://doi.org/10.1086/524298) 12
- Kosovichev, A. G., & Zharkova, V. V. 1998, *Nature*, 393, 317, doi: [10.1038/30629](https://doi.org/10.1038/30629) 10
- Kumar, P., Nakariakov, V. M., & Cho, K.-S. 2017, *The Astrophysical Journal*, 836, 121, doi: [10.3847/1538-4357/836/1/121](https://doi.org/10.3847/1538-4357/836/1/121) 10
- Kuridze, D., Mathioudakis, M., Simões, P. J. A., et al. 2015, *The Astrophysical Journal*, 813, 125, doi: [10.1088/0004-637X/813/2/125](https://doi.org/10.1088/0004-637X/813/2/125) 16, 56
- Kwak, H., Chae, J., Song, D., et al. 2016, *The Astrophysical Journal*, 821, L30, doi: [10.3847/2041-8205/821/2/L30](https://doi.org/10.3847/2041-8205/821/2/L30) 11
- Leenaarts, J., Carlsson, M., & Rouppe van der Voort, L. 2012a, *The Astrophysical Journal*, 749, 136, doi: [10.1088/0004-637X/749/2/136](https://doi.org/10.1088/0004-637X/749/2/136) 16
- Leenaarts, J., Pereira, T., & Uitenbroek, H. 2012b, *Astronomy and Astrophysics*, 543, A109, doi: [10.1051/0004-6361/201219394](https://doi.org/10.1051/0004-6361/201219394) 36
- Leighton, R. B., Noyes, R. W., & Simon, G. W. 1962, *The Astrophysical Journal*, 135, 474,

## Bibliography

- doi: [10.1086/147285](https://doi.org/10.1086/147285) 6
- Lemen, J. R., Title, A. M., Akin, D. J., et al. 2012, Solar Physics, 275, 17, doi: [10.1007/s11207-011-9776-8](https://doi.org/10.1007/s11207-011-9776-8) 17, 18
- Levenberg, K. 1944, Quarterly of applied mathematics, 2, 164 36
- Li, D., Lu, L., Ning, Z., et al. 2020, The Astrophysical Journal, 893, 7, doi: [10.3847/1538-4357/ab7cd1](https://doi.org/10.3847/1538-4357/ab7cd1) 11
- Li, D., Ning, Z. J., & Zhang, Q. M. 2015, The Astrophysical Journal, 807, 72, doi: [10.1088/0004-637X/807/1/72](https://doi.org/10.1088/0004-637X/807/1/72) 10
- Maltby, P., Avrett, E. H., Carlsson, M., et al. 1986, The Astrophysical Journal, 306, 284, doi: [10.1086/164342](https://doi.org/10.1086/164342) 65
- Marquardt, D. W. 1963, Journal of the Society for Industrial and Applied Mathematics, 11, 431, doi: [10.1137/0111030](https://doi.org/10.1137/0111030) 36
- Mathew, S. K., Lagg, A., Solanki, S. K., et al. 2003, Astronomy & Astrophysics, 410, 695, doi: [10.1051/0004-6361:20031282](https://doi.org/10.1051/0004-6361:20031282) 3
- McLaughlin, J. A., Nakariakov, V. M., Dominique, M., Jelínek, P., & Takasao, S. 2018, Space Science Reviews, 214, 45, doi: [10.1007/s11214-018-0478-5](https://doi.org/10.1007/s11214-018-0478-5) 10
- Millar, D. C. L., Fletcher, L., & Milligan, R. O. 2021, Monthly Notices of the Royal Astronomical Society, 503, 2444, doi: [10.1093/mnras/stab642](https://doi.org/10.1093/mnras/stab642) 40
- Milligan, R. O., & Dennis, B. R. 2009, The Astrophysical Journal, 699, 968, doi: [10.1088/0004-637X/699/2/968](https://doi.org/10.1088/0004-637X/699/2/968) 98
- Milligan, R. O., Fleck, B., Ireland, J., Fletcher, L., & Dennis, B. R. 2017, The Astrophysical Journal, 848, L8, doi: [10.3847/2041-8213/aa8f3a](https://doi.org/10.3847/2041-8213/aa8f3a) 11, 25, 27, 57
- Monsue, T., Hill, F., & Stassun, K. G. 2016, The Astronomical Journal, 152, 81, doi: [10.3847/0004-6256/152/4/81](https://doi.org/10.3847/0004-6256/152/4/81) 12
- Morosin, R., de la Cruz Rodríguez, J., Díaz Baso, C. J., & Leenaarts, J. 2022, Astronomy and Astrophysics, 664, A8, doi: [10.1051/0004-6361/202243461](https://doi.org/10.1051/0004-6361/202243461) 37, 122
- Morosin, R., Rodriguez, J. d. l. C., Vissers, G. J. M., & Yadav, R. 2020, doi: [10.48550/ARXIV.2006.14487](https://doi.org/10.48550/ARXIV.2006.14487) 38, 141
- Mumford, S., Freij, N., Christe, S., et al. 2020, Journal of Open Source Software, 5, 1832, doi: [10.21105/joss.01832](https://doi.org/10.21105/joss.01832) 43
- Nakariakov, V. M., Anfinogentov, S., Storozhenko, A. A., et al. 2018, The Astrophysical Journal, 859, 154, doi: [10.3847/1538-4357/aabfb9](https://doi.org/10.3847/1538-4357/aabfb9) 10
- Nakariakov, V. M., Foullon, C., Myagkova, I. N., & Inglis, A. R. 2010a, The Astrophysical

## Bibliography

- Journal, 708, L47, doi: [10.1088/2041-8205/708/1/L47](https://doi.org/10.1088/2041-8205/708/1/L47) 10
- Nakariakov, V. M., Inglis, A. R., Zimovets, I. V., et al. 2010b, Plasma Physics and Controlled Fusion, 52, 124009, doi: [10.1088/0741-3335/52/12/124009](https://doi.org/10.1088/0741-3335/52/12/124009) 10
- Nakariakov, V. M., Ofman, L., DeLuca, E. E., Roberts, B., & Davila, J. M. 1999, Science, 285, 862, doi: [10.1126/science.285.5429.862](https://doi.org/10.1126/science.285.5429.862) 11
- Nakariakov, V. M., Anfinogentov, S. A., Antolin, P., et al. 2021, Space Science Reviews, 217, 73, doi: [10.1007/s11214-021-00847-2](https://doi.org/10.1007/s11214-021-00847-2) 11
- Nechaeva, A., Zimovets, I. V., Nakariakov, V. M., & Goddard, C. R. 2019, The Astrophysical Journal Supplement Series, 241, 31, doi: [10.3847/1538-4365/ab0e86](https://doi.org/10.3847/1538-4365/ab0e86) 11
- Neupert, W. M. 1968, The Astrophysical Journal, 153, L59, doi: [10.1086/180220](https://doi.org/10.1086/180220) 5
- Newton, H. W. 1943, Monthly Notices of the Royal Astronomical Society, 103, 244, doi: [10.1093/mnras/103.5.244](https://doi.org/10.1093/mnras/103.5.244) 4
- Nordlund, A., Stein, R. F., & Asplund, M. 2009, Living Reviews in Solar Physics, 6, doi: [10.12942/lrsp-2009-2](https://doi.org/10.12942/lrsp-2009-2) 2
- Pesnell, W. D., Thompson, B. J., & Chamberlin, P. C. 2012, Solar Physics, 275, 3, doi: [10.1007/s11207-011-9841-3](https://doi.org/10.1007/s11207-011-9841-3) 17
- Petrie, G. J. D. 2019, The Astrophysical Journal Supplement Series, 240, 11, doi: [10.3847/1538-4365/aaef2f](https://doi.org/10.3847/1538-4365/aaef2f) 58
- Phillis, G. L. 1975, Solar Physics, 41, 71, doi: [10.1007/BF00152957](https://doi.org/10.1007/BF00152957) 7
- Pietarila, A., Socas-Navarro, H., & Bogdan, T. 2007, The Astrophysical Journal, 663, 1386, doi: [10.1086/518714](https://doi.org/10.1086/518714) 38
- Pietrow, A. G. M., Kiselman, D., de la Cruz Rodríguez, J., et al. 2020, Astronomy and Astrophysics, 644, A43, doi: [10.1051/0004-6361/202038750](https://doi.org/10.1051/0004-6361/202038750) 37
- Piskunov, N., & Valenti, J. A. 2017, Astronomy and Astrophysics, 597, A16, doi: [10.1051/0004-6361/201629124](https://doi.org/10.1051/0004-6361/201629124) 36
- Potapov, A., Polyushkina, T., & Pulyaev, V. 2013, Journal of Atmospheric and Solar-Terrestrial Physics, 102, 235, doi: [10.1016/j.jastp.2013.06.001](https://doi.org/10.1016/j.jastp.2013.06.001) 6
- Quinn, S., Mathioudakis, M., Nelson, C. J., et al. 2021, The Astrophysical Journal, 920, 25, doi: [10.3847/1538-4357/ac0139](https://doi.org/10.3847/1538-4357/ac0139) 11
- Quinn, S., Reid, A., Mathioudakis, M., et al. 2019, The Astrophysical Journal, 881, 82, doi: [10.3847/1538-4357/ab2c9e](https://doi.org/10.3847/1538-4357/ab2c9e) 11
- Reznikova, V. E., & Shibasaki, K. 2011, Astronomy & Astrophysics, 525, A112, doi: [10.1051/0004-6361/201015600](https://doi.org/10.1051/0004-6361/201015600) 10

## Bibliography

- Reznikova, V. E., Shibasaki, K., Sych, R. A., & Nakariakov, V. M. 2012, *The Astrophysical Journal*, 746, 119, doi: [10.1088/0004-637X/746/2/119](https://doi.org/10.1088/0004-637X/746/2/119) 7, 8, 52
- Rijs, C., Rajaguru, S. P., Przybylski, D., et al. 2016, *The Astrophysical Journal*, 817, 45, doi: [10.3847/0004-637X/817/1/45](https://doi.org/10.3847/0004-637X/817/1/45) 57
- Savitzky, A., & Golay, M. J. E. 1964, *Analytical Chemistry*, 36, 1627, doi: [10.1021/ac60214a047](https://doi.org/10.1021/ac60214a047) 27
- Schafer, R. 2011, *IEEE Signal Processing Magazine*, 28, 111, doi: [10.1109/MSP.2011.941097](https://doi.org/10.1109/MSP.2011.941097) 27
- Scharmer, G. B., Bjelksjo, K., Korhonen, T. K., Lindberg, B., & Petterson, B. 2003a, in *Proceedings of the SPIE*, ed. S. L. Keil & S. V. Avakyan, Waikoloa, Hawai'i, United States, 341, doi: [10.1117/12.460377](https://doi.org/10.1117/12.460377) 13
- Scharmer, G. B., Dettori, P. M., Lofdahl, M. G., & Shand, M. 2003b, 4853, 370, doi: [10.1117/12.460387](https://doi.org/10.1117/12.460387) 14
- Scharmer, G. B., Narayan, G., Hillberg, T., et al. 2008, *The Astrophysical Journal*, 689, L69, doi: [10.1086/595744](https://doi.org/10.1086/595744) 13
- Schou, J., Scherrer, P. H., Bush, R. I., et al. 2012, *Solar Physics*, 275, 229, doi: [10.1007/s11207-011-9842-2](https://doi.org/10.1007/s11207-011-9842-2) 17
- Sharykin, I. N., & Kosovichev, A. G. 2018, *The Astrophysical Journal*, 864, 86, doi: [10.3847/1538-4357/aad558](https://doi.org/10.3847/1538-4357/aad558) 11  
—. 2020, *The Astrophysical Journal*, 895, 76, doi: [10.3847/1538-4357/ab88d1](https://doi.org/10.3847/1538-4357/ab88d1) 11
- Shea, M., & Smart, D. 2006, *Advances in Space Research*, 38, 313, doi: [10.1016/j.asr.2006.07.005](https://doi.org/10.1016/j.asr.2006.07.005) 4
- Simões, P. J. A., Hudson, H. S., & Fletcher, L. 2015, *Solar Physics*, 290, 3625, doi: [10.1007/s11207-015-0691-2](https://doi.org/10.1007/s11207-015-0691-2) 10, 25, 27
- Simões, P. J. A., Reid, H. A. S., Milligan, R. O., & Fletcher, L. 2019, *The Astrophysical Journal*, 870, 114, doi: [10.3847/1538-4357/aaef28d](https://doi.org/10.3847/1538-4357/aaef28d) 17, 57
- Smitha, H. N., & Solanki, S. K. 2017, *Astronomy & Astrophysics*, 608, A111, doi: [10.1051/0004-6361/201731261](https://doi.org/10.1051/0004-6361/201731261) 16
- Socas-Navarro, H., Ruiz Cobo, B., & Trujillo Bueno, J. 1998, *The Astrophysical Journal*, 507, 470, doi: [10.1086/306330](https://doi.org/10.1086/306330) 35
- Srivastava, A. K., Ballester, J. L., Cally, P. S., et al. 2021, *Journal of Geophysical Research: Space Physics*, 126, doi: [10.1029/2020JA029097](https://doi.org/10.1029/2020JA029097) 3
- Sturrock, P. A. 1966, *Nature*, 211, 695, doi: [10.1038/211695a0](https://doi.org/10.1038/211695a0) 5

## Bibliography

- Sudol, J. J., & Harvey, J. W. 2005, The Astrophysical Journal, 635, 647, doi: [10.1086/497361](https://doi.org/10.1086/497361) 58
- Sych, R., Nakariakov, V. M., Karlicky, M., & Anfinogentov, S. 2009, Astronomy & Astrophysics, 505, 791, doi: [10.1051/0004-6361/200912132](https://doi.org/10.1051/0004-6361/200912132) 12
- Sych, R., Zhugzhda, Y., & Yan, X. 2020, The Astrophysical Journal, 888, 84, doi: [10.3847/1538-4357/ab5a78](https://doi.org/10.3847/1538-4357/ab5a78) 8
- Tan, B., & Tan, C. 2012, The Astrophysical Journal, 749, 28, doi: [10.1088/0004-637X/749/1/28](https://doi.org/10.1088/0004-637X/749/1/28) 10
- Thompson, M. J. 2004, Astronomy and Geophysics, 45, 4.21, doi: [10.1046/j.1468-4004.2003.45421.x](https://doi.org/10.1046/j.1468-4004.2003.45421.x) 7
- Threlfall, J., De Moortel, I., & Conlon, T. 2017, Solar Physics, 292, 165, doi: [10.1007/s11207-017-1191-3](https://doi.org/10.1007/s11207-017-1191-3) 28, 30
- Torrence, C., & Compo, G. P. 1998, Bulletin of the American Meteorological Society, 79, 61, doi: [10.1175/1520-0477\(1998\)079<0061:APGTWA>2.0.CO;2](https://doi.org/10.1175/1520-0477(1998)079<0061:APGTWA>2.0.CO;2) 25, 26
- Tsurutani, B. T. 2003, Journal of Geophysical Research, 108, 1268, doi: [10.1029/2002JA009504](https://doi.org/10.1029/2002JA009504) 4
- Uchida, Y., & Sakurai, T. 1975, Publications of the Astronomical Society of Japan, 27, 259. <https://ui.adsabs.harvard.edu/abs/1975PASJ...27..259U> 7
- Uitenbroek, H. 2001, The Astrophysical Journal, 557, 389, doi: [10.1086/321659](https://doi.org/10.1086/321659) 16, 35
- van Driel-Gesztelyi, L., & Green, L. M. 2015, Living Reviews in Solar Physics, 12, 1, doi: [10.1007/lrsp-2015-1](https://doi.org/10.1007/lrsp-2015-1) 3
- Van Noort, M., Der Voort, L. R. V., & Löfdahl, M. G. 2005, Solar Physics, 228, 191, doi: [10.1007/s11207-005-5782-z](https://doi.org/10.1007/s11207-005-5782-z) 14
- van Noort, M. J., & Rouppe van der Voort, L. H. M. 2008, Astronomy & Astrophysics, 489, 429, doi: [10.1051/0004-6361:200809959](https://doi.org/10.1051/0004-6361:200809959) 14
- Van Doorsselaere, T., Kupriyanova, E. G., & Yuan, D. 2016, Solar Physics, 291, 3143, doi: [10.1007/s11207-016-0977-z](https://doi.org/10.1007/s11207-016-0977-z) 10
- Vaughan, S. 2005, Astronomy & Astrophysics, 431, 391, doi: [10.1051/0004-6361:20041453](https://doi.org/10.1051/0004-6361:20041453) 22, 28
- Vernazza, J. E., Avrett, E. H., & Loeser, R. 1981, The Astrophysical Journal Supplement Series, 45, 635, doi: [10.1086/190731](https://doi.org/10.1086/190731) 16
- Verwichte, E., Foulon, C., & Van Doorsselaere, T. 2010, The Astrophysical Journal, 717, 458, doi: [10.1088/0004-637X/717/1/458](https://doi.org/10.1088/0004-637X/717/1/458) 11

## *Bibliography*

- Virtanen, P., Gommers, R., Oliphant, T. E., et al. 2020, *Nature Methods*, 17, 261, doi: [10.1038/s41592-019-0686-2](https://doi.org/10.1038/s41592-019-0686-2) 31
- Webb, D. F., & Howard, T. A. 2012, *Living Reviews in Solar Physics*, 9, doi: [10.12942/lrsp-2012-3](https://doi.org/10.12942/lrsp-2012-3) 4
- Woods, T. N., Eparvier, F. G., Hock, R., et al. 2012, *Solar Physics*, 275, 115, doi: [10.1007/s11207-009-9487-6](https://doi.org/10.1007/s11207-009-9487-6) 17
- Wuelser, J.-P., & Marti, H. 1989, *The Astrophysical Journal*, 341, 1088, doi: [10.1086/167567](https://doi.org/10.1086/167567) 5
- Yadav, R., Díaz Baso, C. J., de la Cruz Rodríguez, J., Calvo, F., & Morosin, R. 2021, *Astronomy and Astrophysics*, 649, A106, doi: [10.1051/0004-6361/202039857](https://doi.org/10.1051/0004-6361/202039857) 37